Mon. Not. R. Astron. Soc. **000**, 1–23 (2010) Printed 14 June 2010 (MN LATEX style file v2.2)

The LABOCA survey of the Extended Chandra Deep Field South: A photometric redshift survey of submillimetre galaxies

J. L. Wardlow[1⋆], Ian Smail[2], K. E. K. Coppin[2], D. M. Alexander[1], W. N. Brandt[3], A. L. R. Danielson[1], B. Luo[3], A. M. Swinbank[2], F. Walter[4], A. Weiß[5], Y. Q. Xue[3], S. Zibetti[4], F. Bertoldi[6], A. D. Biggs[7], S. C. Chapman[8], H. Dannerbauer[4], J. S. Dunlop[9], E. Gawiser[10], R. J. Ivison[9,11], K. K. Knudsen[6], A. Kovács[5], C. G. Lacey[2], K. M. Menten[5], N. Padilla[12], H.-W. Rix[4], and P. P. van der Werf[13]

[1]*Department of Physics, Durham University, South Road, Durham, DH1 3LE, UK*
[2]*Institute for Computational Cosmology, Durham University, South Road, Durham, DH1 3LE, UK*
[3]*Department of Astronomy and Astrophysics, 525 Davey Lab, Pennsylvania State University, University Park, PA 16802, USA*
[4]*Max-Planck-Institut für Astronomie, Königstuhl 17, D-69117 Heidelberg, Germany*
[5]*Max-Planck-Institut für Radioastronomie, Auf dem Hügel 69, D-53121 Bonn, Germany*
[6]*Argelander Institut für Astronomie, Auf dem Hügel 71, D-53121 Bonn, Germany*
[7]*European Southern Observatory, Karl-Schwarzschild Strasse 2, D-85748 Garching, Germany*
[8]*Institute of Astronomy, Madingley Road, Cambridge, CB3 0HA, UK*
[9]*SUPA (Scottish University Physics Alliance), Institute for Astronomy, University of Edinburgh, Royal Observatory, Edinburgh EH9 3HJ, UK*
[10]*Physics and Astronomy Department, Rutgers University, Piscataway, NJ 08854, USA*
[11]*UK Astronomy Technology Centre, Royal Observatory, Blackford Hill, Edinburgh EH9 3HJ, UK*
[12]*Departmento de Astronomia y Astrofisica, Pontificia Universidad Catolica de Chile, Santiago, Chile*
[13]*Leiden Observatory, Leiden University, P.O. Box 9513, 2300 RA Leiden, The Netherlands*

14 June 2010

ABSTRACT

We derive photometric redshifts from 17-band optical to mid-infrared photometry of 74 robust radio, 24 μm and *Spitzer* IRAC counterparts to 68 of the 126 submillimetre galaxies (SMGs) selected at 870 μm by LABOCA observations in the Extended *Chandra* Deep Field South (ECDFS). We test the photometric redshifts of the SMGs against the extensive archival spectroscopy in the ECDFS. The median photometric redshift of identified SMGs is $z = 2.2 \pm 0.1$, the interquartile range is $z = 1.8$–2.7 and we identify 10 ($\sim 15\%$) high-redshift ($z \geqslant 3$) SMGs. We derive a simple redshift estimator for SMGs based on the IRAC 3.6 and 8 μm fluxes which is accurate to $\Delta z \sim 0.4$ for SMGs at $z < 4$. A statistical analysis of sources around unidentified SMGs identifies a population of likely counterparts with a redshift distribution peaking at $z = 2.5 \pm 0.3$, which likely comprises $\sim 60\%$ of the unidentified SMGs. This confirms that the bulk of the undetected SMGs are co-eval with those detected in the radio/mid-infrared. We conclude that at most $\sim 15\%$ of all the SMGs are below the flux limits of our IRAC observations and lie at $z \gtrsim 3$ and hence around $\sim 30\%$ of all SMGs have $z \gtrsim 3$. We estimate that the full $S_{870\mu m} > 4$ mJy SMG population has a median redshift of 2.5 ± 0.6. In contrast to previous suggestions we find no significant correlation between submillimetre flux and redshift. The median stellar mass of the SMGs derived from SED fitting is $(9.2 \pm 0.9) \times 10^{10}\,M_{\odot}$ and the interquartile range is (4.7–14)$\times 10^{10}\,M_{\odot}$, although we caution that the uncertainty in the star-formation histories results in a factor of ~ 5 uncertainty in these stellar masses. Using a single temperature modified blackbody fit with $\beta = 1.5$ the median characteristic dust temperature of SMGs is 35.9 ± 1.4 K and the interquartile range is 28.5–43.3 K. The infrared luminosity function shows that SMGs at $z = 2$–3 typically have higher far-infrared luminosities and luminosity density than those at $z = 1$–2. This is mirrored in the evolution of the star-formation rate density (SFRD) for SMGs which peaks at $z \sim 2$. The maximum contribution of bright SMGs to the global SFRD ($\sim 5\%$ for SMGs with $S_{870\mu m} \gtrsim 4$ mJy; $\sim 50\%$ for SMGs with $S_{870\mu m} > 1$ mJy) also occurs at $z \sim 2$.

Key words: submillimetre – galaxies: starburst – galaxies: evolution – galaxies: high-redshift

⋆ E-mail: j.l.wardlow@durham.ac.uk

1 INTRODUCTION

Observations in the millimetre and submillimetre wavebands provide a uniquely powerful route to survey the distant Universe for intense dust-obscured starbursts (Blain & Longair 1993). This is due to the negative K-correction arising from the shape of the spectral energy distribution (SED) of the dust emission in the rest-frame far-infrared, which results in an almost constant apparent flux for sources with a fixed luminosity at $z \sim 1$–8.

Over the past decade, a series of ever larger surveys in the submillimetre and millimetre wavebands have mapped out a population of sources at mJy-flux limits with a surprisingly high surface density (e.g. Smail et al. 1997; Barger et al. 1998; Hughes et al. 1998; Eales et al. 1999; Bertoldi et al. 2000, 2007; Coppin et al. 2006; Knudsen et al. 2008; Weiß et al. 2009; Austermann et al. 2010). The mJy fluxes of these sources imply far-infrared luminosities of $\gtrsim 10^{12}$ L$_{\odot}$, if the sources are at cosmological distances, $z \gtrsim 1$, classing them as ultraluminous infrared galaxies (ULIRGs; Sanders & Mirabel 1996). Their high surface density is far in excess of that expected from a "no evolution" model, suggesting very strong evolution of the population: $\propto (1+z)^4$ (Smail et al. 1997; Blain et al. 1999). If this results from strong luminosity evolution of starburst galaxies (as opposed to obscured AGN; Alexander et al. 2005 then a significant fraction of the massive star formation (and metal production) at high redshift may be occurring in this population.

To confirm this evolution and understand the physical processes driving it requires redshifts for the submillimetre galaxies (SMGs). Due to the coarse spatial resolution of the submillimetre and millimetre maps from which the SMGs can be identified, combined with their optical faintness (in part due to their high dust obscuration), it has proved challenging to measure their spectroscopic redshift distribution (e.g. Barger et al. 1999; Chapman et al. 2003a, 2005).

In fact, spectroscopic redshifts are not necessary to map the broad evolution of the SMG population and cruder photometric redshifts can be sufficient, if they are shown to be reliable. Various photometric redshift techniques have therefore been applied in an attempt to trace the evolution of SMGs, using their optical/near-/mid-infrared or far-infrared/radio SEDs (e.g. Carilli & Yun 1999; Smail et al. 2000; Ivison et al. 2004; Pope et al. 2005, 2006; Ivison et al. 2007; Aretxaga et al. 2007; Clements et al. 2008; Dye et al. 2008; Biggs et al. 2010).

Both spectroscopic and photometric analyses suggest that the bulk of the SMG population lies at $z \gtrsim 1$, with an apparent peak at $z \sim 2.2$ for the subset of SMGs which can be located through their μJy radio emission (Chapman et al. 2005). Nevertheless, there are significant disagreements between the different studies (see e.g. Chapman et al. 2005; Clements et al. 2008; Dye et al. 2008), which may arise in part due to differing levels and types of incompleteness in the identifications and biases in the redshift measurements. The most serious of these is the incompleteness due to challenges in reliably locating the correct SMG counterpart. They are typically identified through statistical arguments and physical correlations based on radio, mid- or near-infrared emission (e.g. Ivison et al. 1998, 2000, 2005; Smail et al. 1999; Pope et al. 2005; Bertoldi et al. 2007; Hainline et al. 2009; Biggs et al. 2010), but these locate only ~ 60–80% of SMGs. The expectation is that the SMGs whose counterparts are missed could potentially include the highest redshift (and thus the faintest in the radio and mid-infrared) examples, biasing the derived evolution (Ivison et al. 2005). Attempts to address this incompleteness through time-intensive submillimetre interferometry have located a small fraction of previously unidentified SMGs (e.g. Dannerbauer et al. 2002, 2008; Younger et al. 2007, 2009; Wang et al. 2007) but the nature and redshifts of this unidentified subset of SMGs remains a critical issue for studies of the population as a whole.

In this paper we use optical, near- and mid-infrared photometry to study SMGs detected in the Extended *Chandra* Deep Field South (ECDFS) by the Large APEX BOlometer CAmera (LABOCA; Siringo et al. 2009) on the Atacama Pathfinder EXperiment (APEX; Güsten et al. 2006) 12-m telescope in the LABOCA ECDFS Submillimetre Survey (LESS; Weiß et al. 2009). LESS mapped the full $30' \times 30'$ ECDFS at 870-μm to a noise level of $\sigma_{870\mu m} \approx 1.2$ mJy beam^{-1}, for a beam with angular resolution of $19\farcs2$. 126 SMGs were detected at $> 3.7\sigma$ significance (equivalent to a false-detection rate of $\sim 4\%$, Weiß et al. 2009) and robust or tentative radio, 24 μm or IRAC mid-infrared counterparts are identified to 93 (71 robust and 22 tentative) SMGs (Biggs et al. 2010). Here we determine photometric redshifts for the 91 (68 robust and 23 tentative) of these SMGs with detectable optical and near-infrared counterparts in new and archival multiband photometry of the ECDFS (described in §2). LESS is an ideal survey for this purpose because of its panoramic, deep and uniform submillimetre coverage and extensive auxiliary data, including spectroscopy of sufficient SMG counterparts to adequately test our photometric redshifts. In addition, the large size of the survey allows us to statistically measure the redshift distribution of the SMGs that we are unable to locate directly, in order to test if their redshift distribution differs significantly from the identified population.

The plan of the paper is as follows: in §2 we derive multiband photometry from new and archival observations; while in §3 we describe our the photometric redshift estimates and tests of their reliability. The photometric redshifts, SED fits, absolute H-band magnitudes, infrared luminosities, dust temperatures and star-formation rates of SMGs are presented and discussed in §4 and we present our conclusions in §5. Throughout this paper we use deboosted submillimetre fluxes from Weiß et al. (2009), J2000 coordinates and ΛCDM cosmology with $\Omega_M = 0.3$, $\Omega_\Lambda = 0.7$ and $H_0 = 70 \mathrm{kms}^{-1}\mathrm{Mpc}^{-1}$. All photometry is on the AB magnitude system, in which $23.9\ \mathrm{m_{AB}} = 1\mu\mathrm{Jy}$, unless otherwise stated.

2 OBSERVATIONS AND DATA REDUCTION

In this paper we consider the optical and infrared counterparts to 126 SMGs in the ECDFS detected at $\geqslant 3.7\sigma$ (Weiß et al. 2009) and identified by VLA radio, MIPS (Rieke et al. 2004) 24 μm and IRAC (Fazio et al. 2004) emission (Biggs et al. 2010). Following convention and Biggs et al. (2010) we consider robust counterparts as those with a corrected Poissonian probability of being unassociated with the submillimetre source (*p*; Downes et al. 1986) of $p \leqslant 0.05$ in one or more of the radio, 24μm, or IRAC datasets, or $p = 0.05$ – 0.10 in two or more; tentative counterparts are those with $p = 0.05$ – 0.10 in only one of the three bands.

Six of the SMGs have multiple robust counterparts; of these four SMGs (LESS 2, LESS 27, LESS 49 and LESS 74) have two counterparts with photometric redshifts (§3.1) consistent with them being at the same distance and possibly physically associated. Two SMGs (LESS 10 and LESS 49) each have two robust counterparts with photometric redshifts and SEDs that suggest they are not physically associated. In these cases, from the information currently available, it is not possible to determine which of the two counterparts is the source of the submillimetre flux, or whether the

Table 1. Summary of photometry employed in this paper.

Filter	$\lambda_{\rm effective}$ (μm)	Detection limit (3σ; mag)	Reference
MUSYC WFI U	0.35	26.9	Taylor et al. (2009b)
MUSYC WFI $U38$	0.37	25.4	Taylor et al. (2009b)
VIMOS U	0.38	28.4[a]	Nonino et al. (2009)
MUSYC WFI B	0.46	26.8	Taylor et al. (2009b)
MUSYC WFI V	0.54	26.7	Taylor et al. (2009b)
MUSYC WFI R	0.66	25.8	Taylor et al. (2009b)
MUSYC WFI I	0.87	24.9	Taylor et al. (2009b)
MUSYC Mosaic II z	0.91	24.5	Taylor et al. (2009b)
MUSYC ISPI J	1.25	23.6	Taylor et al. (2009b)
HAWK-I J	1.26	25.7	Zibetti et al. (in prep.)
MUSYC SofI H	1.66	23.0	Taylor et al. (2009b)
MUSYC ISPI K	2.13	22.7	Taylor et al. (2009b)
HAWK-I K_s	2.15	25.3	Zibetti et al. (in prep.)
SIMPLE IRAC 3.6μm	3.58	24.6	Damen et al. (2010)
SIMPLE IRAC 4.5μm	4.53	24.4	Damen et al. (2010)
SIMPLE IRAC 5.8μm	5.79	22.8	Damen et al. (2010)
SIMPLE IRAC 8.0μm	8.05	23.5	Damen et al. (2010)

[a] The listed depth of the VIMOS U band is that of the central region. The typical depth in the shallower outskirts is 28.0 mag

LABOCA detection is a blend of emission from two galaxies. To avoid bias we have included all of the multiple counterparts in our analysis, but we note that their small number means that their inclusion does not significantly affect our results.

2.1 Optical and infrared photometry

SMGs typically have faint optical and near-infrared counterparts (e.g. Ivison et al. 2002) so we require deep photometry for accurate photometric redshift estimates. The ECDFS was chosen for this survey because it is an exceptionally well-studied field, and as such we are able to utilise data from extensive archival imaging and spectroscopic surveys. For completeness and uniformity we only consider surveys that cover a large fraction of the ECDFS rather than the smaller and deeper central CDFS region. Therefore, we utilise the MUltiwavelength Survey by Yale-Chile (MUSYC; Gawiser et al. 2006) near-infrared survey for U to K-band imaging (Taylor et al. 2009b), and the *Spitzer* IRAC/MUSYC Public Legacy in ECDFS (SIMPLE) imaging for *Spitzer* IRAC data (Damen et al. 2010). We also include U-band data from the deep GOODS/VIMOS imaging survey of the CDFS (Nonino et al. 2009); although this covers only $\sim 60\%$ of LESS SMGs it is valuable for galaxies that are undetected at short wavelengths in the shallower MUSYC survey.

In addition, we have carried out deep near-infrared observations in the J and K_s bands with HAWK-I (Pirard et al. 2004; Casali et al. 2006; Kissler-Patig et al. 2008) at the ESO-VLT (ID: 082.A-0890, P.I. N. Padilla). The ECDFS was covered with a mosaic of 16 pointings in each band, with a total exposure time of 0.75 and 1.1 hours per pointing, in the J and K_s bands respectively. The median seeing is $0.7''$ in J and $0.5''$ in K_s. Data reduction has been performed using an upgraded version of the official ESO pipeline for HAWK-I, customized calibration has been obtained from observations of photometric standard stars. More details and catalogues will be published in Zibetti et al. (in preparation).

For accurate photometric redshifts we require consistent photometry in apertures which sample the same emitting area in each of the 17 filters. For consistency between surveys and to ensure that all detected SMG counterparts are included in this study we extract photometry from the available survey imaging rather than relying on the catalogued sources. SMGs are typically brighter at mid-infrared than optical wavelengths due to their high redshifts and extreme dust obscuration. Therefore, we use SExtractor (Bertin & Arnouts 1996) to create a source list from a combined image of the four IRAC channels, which is weighted such that a given magnitude receives equal contributions from all of the input images. Real sources are required to have at least 4 contiguous $0.6'' \times 0.6''$ pixels with fluxes at least 1.5 times the background noise. In addition, we visually check the area within $15''$ of each LABOCA source to ensure that no potential SMG counterparts are missed.

We next use APPHOT in IRAF to measure the fluxes in $3.8''$ diameter apertures for each of the four IRAC bands. We then cut the catalogues to $\geqslant 3\sigma$ based on the background noise, and finally apply aperture corrections as derived by the SWIRE team (Surace et al. 2005) to obtain total source magnitudes. The resolution in the U- to K-band imaging is better than IRAC (FWHM $\leqslant 1.5''$ compared to $\sim 2''$ for IRAC) and so we convolve each U- to K-band image to match the $1.5''$ seeing of the worst band. We next use APPHOT to measure photometry in $3''$ diameter apertures at the positions of the IRAC-selected sources. In all cases, we only allow APPHOT to re-centroid the aperture if centroiding does not cause the extraction region to be moved to a nearby source, as flagged by IRAF's CIER parameter when the centroid shift is $> 0.5''$. We have not performed any deblending of the photometry but examination of the images suggests fewer than $\sim 10\%$ of the SMG counterparts are affected. We note here that the photometric extraction process is not restricted to SMGs and yields photometry (which allows us to calculate consistent photometric redshifts) for IRAC-selected sources throughout the ECDFS.

Finally, to ensure equivalent photometry between the IRAC and optical-to-near-infrared filters we create simulated IRAC images of point sources. Using these images we calculate that the correction between the measured IRAC total magnitudes and the photometry extracted from $3''$ diameter apertures on $1.5''$ seeing images is -0.014 ± 0.017 magnitudes, and as such we do not apply any systematic corrections to the IRAC magnitudes at this stage. In §3.1 we calibrate the photometry prior to photometric redshift calculation in a process which corrects for small residual offsets. A summary of our photometry is presented in Table 1.

The median number of photometric filters per SMG counterpart is 15 and we require detections in at least three photometric filters in order to calculate photometric redshifts. Our final sample therefore contains 74 optical counterparts to the 68 robustly identified SMGs with sufficient detectable optical-to-infrared emission. In §3.3 we show that the exclusion of the additional 23, tentatively identified, counterparts does not bias our results.

2.2 Spectroscopy

We employ spectroscopy of the ECDFS to calibrate our photometry with the SED templates (§3.1) and test our photometric redshifts (§3.2). We have examined the spectroscopic redshift catalogues from many archival surveys (Cristiani et al. 2000; Croom et al. 2001; Bunker et al. 2003; Dickinson et al. 2004; Le Fèvre et al. 2004; Stanway et al. 2004; Strolger et al. 2004; Szokoly et al. 2004; van der Wel et al. 2004; Zheng et al. 2004; Daddi et al. 2005; Doherty et al. 2005; Mignoli et al. 2005; Grazian et al. 2006; Ravikumar et al. 2007; Kriek et al. 2008; Vanzella et al. 2008;

Popesso et al. 2009; Treister et al. 2009; Balestra et al. 2010, Koposov et al. in prep.) and also our own on-going spectroscopic survey of LESS sources with the VLT (PID: 183.A-0666, P.I. I. Smail), which will be published in full in Danielson et al. (in prep.).

3 ANALYSIS

3.1 Photometric redshift calculation

We use HYPERZ[1] (Bolzonella et al. 2000) to calculate the photometric redshifts of counterparts to LESS SMGs (Biggs et al. 2010). HYPERZ compares a model SED to observed magnitudes and computes χ^2 for each combination of spectral type, age, reddening and redshift and thus statistically determines the most likely redshift of the galaxy. We use the elliptical (E), Sb, single burst (Burst) and constant star-formation (Im) spectral templates from Bruzual & Charlot (1993) which are provided with HYPERZ, and allow reddening (Calzetti et al. 2000) of $A_V = 0$–5 in steps of 0.2. This combination of templates and A_V was shown by Wardlow et al. (2010) to be sufficient for calculating photometric redshifts of SMGs. Redshifts between 0 and 7 are considered and galaxy ages are required to be less than the age of the Universe at the appropriate redshift. In §3.5 we show that the HYPERZ-derived galaxy ages cannot be reliably determined, but we note here that the requirement for SMGs to be younger than the Universe does not significantly affect the derived redshifts. Galaxies are assigned zero flux in any filter in which they are not detected, with an error equal to the 1σ detection limit of that filter. To ensure that galaxies at $z \sim 2$–3 do not have their redshifts systematically underestimated we have modified the handling of the Lyman-α forest in HYPERZ, such that intragalactic absorption in the models is increased and three different levels of absorption are considered in the fitting process. The reliability of the calculated redshifts and the validity of these settings is tested in full in §3.2.

We test for small systematic discrepancies between the photometry and model SEDs prior to using HYPERZ to calculate photometric redshifts of SMGs. This is done by running HYPERZ on 1796 galaxies and AGN with spectroscopic redshifts in the ECDFS and requiring a fit at the observed redshift. We then compare the model and measured magnitudes for each galaxy, and iteratively adjust the zeropoints of the filters with the largest systematic offsets. This yields significant offsets for the following filters: VIMOS U (0.083 mag), MUSYC U (-0.091 mag), $U38$ (-0.074 mag), R (0.049 mag), I (0.048 mag), z (0.095 mag), HAWK-I J (0.043 mag), IRAC 3.6 (0.043 mag) and IRAC 8.0 μm (0.110 mag). The typical uncertainties in these corrections are ± 0.02 and the remaining eight filters have no significant corrections.

The calibrated photometry of the robust LESS SMG counterparts is listed in Table 4 and in Table 2 we provide the coordinates, photometric redshifts, absolute rest-frame H-band magnitudes, far-infrared luminosities and characteristic dust temperatures of the SMGs (§4.6). We also provide the reduced χ^2 of the best fit SED at the derived photometric redshift and the number of filters in which the SMG was detected and undetected (but observed). We caution that the reduced χ^2 for galaxies with only a few photometric detections is typically low ($\lesssim 0.5$) but the error on the photometric redshift is typically large, since there are only weak limits on the SED from the photometry. Therefore, the values of the reduced χ^2 should be considered in conjunction with the number of photometric detections when considering the reliability of the photometric redshifts.

[1] We use HYPERZ version 10.0 (http://www.ast.obs-mip.fr/users/roser/hyperz/)

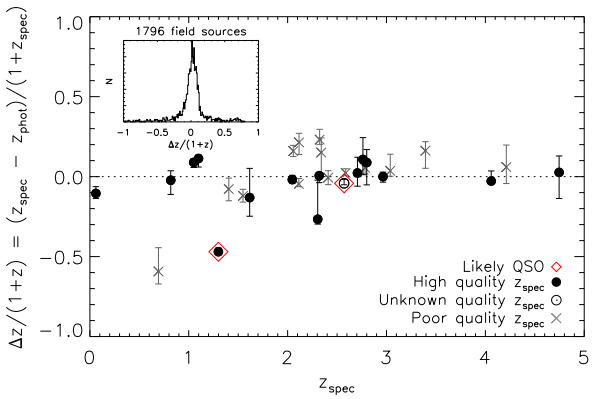

Figure 1. Spectroscopic redshift against $\Delta z/(1+z)$ for robust counterparts to LESS SMGs. We distinguish between high and low quality spectroscopic redshifts as determined by the flags provided in most archival catalogues, and highlight the two likely quasars (LESS 66 and LESS 96; see Appendix A). The median (mean) $\Delta z/(1+z)$ for the all the SMGs is 0.023 ± 0.021 (-0.013 ± 0.178). The inset plot shows the histogram of $\Delta z/(1+z)$ for 1796 galaxies and AGN in the ECDFS with spectroscopic redshifts. The distribution is centered on 0.016 ± 0.002 and has a 1σ dispersion of 0.05. We conclude that our photometric redshifts are a good proxy for spectroscopic redshifts for both samples.

The median reduced χ^2 of the SMG counterparts is 2.3 (2.1 if only the galaxies with reduced $\chi^2 \leqslant 10$ are considered). This suggests that our photometric errors are slightly overestimated and lead to apparently overly-precise photometric redshift limits. Indeed, we find that the HYPERZ 99% confidence intervals more reliably represent the 1σ errors, yielding $\sim 68\%$ of SMGs with photometric redshifts consistent with the spectroscopic redshifts. Therefore, throughout this paper we use the HYPERZ 99% confidence intervals on the photometric redshift estimates to represent the 1-σ uncertainty. Of the 74 SMG counterparts examined there are eight with poor fits of the SED to the photometry (indicated with reduced $\chi^2 > 10$). Of these, one (LESS 39) is blended in the optical imaging and two (LESS 66 and LESS 81) lie in stellar halos. LESS 66 is also likely to be a quasar, as is LESS 96, and another four SMGs with reduced $\chi^2 > 10$ (LESS 19, LESS 57, LESS 75 and LESS 111) have excess 8 μm flux compared to the best-fit SED, which is indicative of an AGN component (see §3.4 for a full discussion). Since we did not include any quasar or AGN templates in the fitting procedure it is unsurprising that these sources are not well represented by the employed SEDs. We note here that, as we show in §3.4, the exclusion of AGN templates does not bias our photometric redshift estimates.

3.2 Reliability of photometric redshifts

To test the reliability of our photometric redshifts ($z_{\rm phot}$) we first compare them to the spectroscopic redshifts ($z_{\rm spec}$) for 1796 galaxies and AGN in the ECDFS and calculate $\Delta z = z_{\rm spec} - z_{\rm phot}$ for each source. The histogram of $\Delta z/(1+z)$ for these 1796 sources is shown as an inset in Fig.1; the sample is centered on $\Delta z/(1+z) = 0.016 \pm 0.002$ and has a 1σ dispersion of 0.05. We define outliers as sources with $|\Delta z|/(1+z) > 0.3$; the outlier fraction for these 1796 field galaxies and AGN is 0.15. We also calculate the outlier

Table 2. The catalogue of 74 robust counterparts to LESS SMGs, their photometric redshift estimates, reduced χ^2 of the best-fit SED and the number of photometric filters in which the galaxy is observed. We also present the absolute rest-frame H-band magnitudes, the derived far-infrared luminosities and characteristic dust temperatures of the SMGs.

SMG[a]	Short name	RA[b]	Dec[b]	$z_{\rm phot}$[c]	$\chi^2_{\rm red}$[d]	Filters[e]	M_H[f] (mag)	L_{FIR}[g] ($10^{12}L_\odot$)	T_D[h] (K)	ID type[i]
LESSJ033302.5-275643	LESS 2a	$03^{\rm h}33^{\rm m}02\overset{\rm s}{.}55$	$-27°56'44\overset{''}{.}7$	$1.80^{+0.35}_{-0.14}$	2.8	16 [1]	-23.42	< 1.5	< 19.9	M
LESSJ033302.5-275643	LESS 2b	$03^{\rm h}33^{\rm m}02\overset{\rm s}{.}68$	$-27°56'42\overset{''}{.}6$	$2.27^{+0.16}_{-0.55}$	1.1	8 [9]	-23.15	$30.9^{+6.4}_{-15.3}$	$44.2^{+2.5}_{-7.6}$	R
LESSJ033321.5-275520	LESS 3	$03^{\rm h}33^{\rm m}21\overset{\rm s}{.}50$	$-27°55'20\overset{''}{.}1$	$3.92^{+0.54}_{-0.72}$	0.5	5 [10]	-24.66	< 8.9	< 35.2	M
LESSJ033257.1-280102	LESS 6	$03^{\rm h}32^{\rm m}57\overset{\rm s}{.}15$	$-28°01'01\overset{''}{.}5$	$0.40^{+0.09}_{-0.03}$	4.3	16 [1]	-20.29	$0.09^{+0.08}_{-0.03}$	$12.8^{+1.1}_{-0.8}$	RM
LESSJ033315.6-274523	LESS 7	$03^{\rm h}33^{\rm m}15\overset{\rm s}{.}41$	$-27°45'24\overset{''}{.}0$	$2.81^{+0.18}_{-0.07}$	6.9	16 [1]	-25.50	$16.2^{+4.3}_{-2.4}$	$41.1^{+2.6}_{-1.9}$	RM
LESSJ033211.3-275210	LESS 9	$03^{\rm h}32^{\rm m}11\overset{\rm s}{.}35$	$-27°52'12\overset{''}{.}9$	$4.63^{+0.10}_{-1.10}$	2.4	6 [9]	-25.29	$20.3^{+5.9}_{-11.7}$	$48.3^{+3.4}_{-10.0}$	RM
LESSJ033219.0-275219	LESS 10a	$03^{\rm h}32^{\rm m}19\overset{\rm s}{.}04$	$-27°52'14\overset{''}{.}3$	$2.46^{+0.15}_{-0.15}$	6.0	12 [5]	-23.46	$8.7^{+2.4}_{-2.0}$	$34.5^{+2.2}_{-2.2}$	R
LESSJ033219.0-275219	LESS 10b	$03^{\rm h}32^{\rm m}19\overset{\rm s}{.}30$	$-27°52'19\overset{''}{.}1$	$0.91^{+0.07}_{-0.05}$	4.5	15 [2]	-23.32	$0.8^{+0.3}_{-0.2}$	$18.6^{+1.1}_{-1.0}$	R
LESSJ033213.6-275602	LESS 11	$03^{\rm h}32^{\rm m}13\overset{\rm s}{.}84$	$-27°55'59\overset{''}{.}8$	$2.60^{+0.30}_{-0.36}$	3.2	7 [9]	-24.04	$9.9^{+4.4}_{-3.8}$	$35.9^{+3.5}_{-4.0}$	R
LESSJ033248.1-275414	LESS 12	$03^{\rm h}32^{\rm m}47\overset{\rm s}{.}96$	$-27°54'16\overset{''}{.}1$	$3.92^{+1.02}_{-2.11}$	0.1	6 [11]	-24.06	$18.2^{+17.3}_{-15.6}$	$45.6^{+9.8}_{-19.7}$	RM
LESSJ033152.6-280320	LESS 14	$03^{\rm h}31^{\rm m}52\overset{\rm s}{.}47$	$-28°03'18\overset{''}{.}6$	$3.56^{+0.92}_{-0.56}$	0.8	7 [9]	-24.74	$32.6^{+26.6}_{-12.5}$	$51.3^{+10.6}_{-6.7}$	RM
LESSJ033333.4-275930	LESS 15	$03^{\rm h}33^{\rm m}33\overset{\rm s}{.}35$	$-27°59'29\overset{''}{.}4$	$1.95^{+3.05}_{-0.39}$	0.2	4 [8]	-23.59	< 1.8	< 22.6	M
LESSJ033218.9-273738	LESS 16	$03^{\rm h}32^{\rm m}18\overset{\rm s}{.}70$	$-27°37'43\overset{''}{.}5$	$1.09^{+0.08}_{-0.09}$	4.1	17 [0]	-24.05	$1.2^{+0.4}_{-0.4}$	$20.8^{+1.4}_{-1.5}$	R
LESSJ033207.6-275123	LESS 17	$03^{\rm h}32^{\rm m}07\overset{\rm s}{.}26$	$-27°51'20\overset{''}{.}1$	$1.55^{+0.11}_{-0.11}$	1.0	17 [0]	-24.11	$6.6^{+1.5}_{-1.4}$	$32.7^{+2.0}_{-2.1}$	RM
LESSJ033205.1-274652	LESS 18	$03^{\rm h}32^{\rm m}04\overset{\rm s}{.}87$	$-27°46'47\overset{''}{.}4$	$2.07^{+0.08}_{-0.09}$	2.4	16 [1]	-24.88	$13.8^{+2.1}_{-2.0}$	$40.2^{+2.1}_{-2.1}$	RM
LESSJ033208.1-275818	LESS 19	$03^{\rm h}32^{\rm m}08\overset{\rm s}{.}23$	$-27°58'13\overset{''}{.}7$	$2.11^{+0.11}_{-0.10}$	10.3	10 [6]	-22.80	$3.4^{+1.3}_{-1.1}$	$28.3^{+2.3}_{-2.2}$	RI
LESSJ033316.6-280018[j]	LESS 20	$03^{\rm h}33^{\rm m}16\overset{\rm s}{.}77$	$-28°00'15\overset{''}{.}8$	$2.80^{+0.17}_{-0.27}$	2.2	9 [7]	-24.28	903^{+132}_{-190}	$124.6^{+7.8}_{-10.5}$	RM
LESSJ033147.0-273243	LESS 22	$03^{\rm h}31^{\rm m}46\overset{\rm s}{.}90$	$-27°32'38\overset{''}{.}8$	$1.95^{+0.34}_{-0.38}$	2.4	6 [4]	-24.67	$10.4^{+5.8}_{-4.6}$	$36.6^{+4.6}_{-5.1}$	RM
LESSJ033336.8-274401	LESS 24	$03^{\rm h}33^{\rm m}36\overset{\rm s}{.}97$	$-27°43'58\overset{''}{.}1$	$1.72^{+0.29}_{-0.36}$	2.6	11 [2]	-24.06	$4.1^{+2.6}_{-2.1}$	$29.2^{+3.6}_{-4.3}$	RM
LESSJ033157.1-275940	LESS 25	$03^{\rm h}31^{\rm m}56\overset{\rm s}{.}85$	$-27°59'38\overset{''}{.}9$	$2.28^{+0.09}_{-0.15}$	3.0	13 [2]	-24.47	$8.1^{+1.8}_{-2.1}$	$36.4^{+2.4}_{-2.8}$	RM
LESSJ033149.7-273432	LESS 27a	$03^{\rm h}31^{\rm m}49\overset{\rm s}{.}88$	$-27°34'30\overset{''}{.}4$	$2.10^{+1.00}_{-0.88}$	0.1	4 [11]	-22.83	< 2.1	< 25.1	I
LESSJ033149.7-273432	LESS 27b	$03^{\rm h}31^{\rm m}49\overset{\rm s}{.}92$	$-27°34'36\overset{''}{.}7$	$2.46^{+0.42}_{-0.72}$	1.9	7 [6]	-23.73	< 3.1	< 28.1	MI
LESSJ033336.9-275813	LESS 29	$03^{\rm h}33^{\rm m}36\overset{\rm s}{.}88$	$-27°58'08\overset{''}{.}8$	$2.64^{+4.36}_{-0.87}$	0.1	4 [8]	-24.13	$8.4^{+78.5}_{-5.8}$	$36.8^{+44.0}_{-9.2}$	R
LESSJ033150.0-275743	LESS 31	$03^{\rm h}31^{\rm m}49\overset{\rm s}{.}77$	$-27°57'40\overset{''}{.}4$	$3.63^{+0.84}_{-0.70}$	0.3	6 [9]	-24.30	$9.9^{+10.0}_{-5.4}$	$41.8^{+8.5}_{-7.3}$	RI
LESSJ033217.6-275230	LESS 34	$03^{\rm h}32^{\rm m}17\overset{\rm s}{.}60$	$-27°52'28\overset{''}{.}1$	$0.86^{+0.11}_{-0.05}$	3.8	17 [0]	-23.53	< 0.3	< 15.6	M
LESSJ033149.2-280208	LESS 36	$03^{\rm h}31^{\rm m}48\overset{\rm s}{.}94$	$-28°02'13\overset{''}{.}6$	$2.49^{+0.53}_{-0.31}$	0.3	7 [7]	-24.58	$7.8^{+6.4}_{-3.0}$	$36.7^{+6.2}_{-4.2}$	RM
LESSJ033336.0-275347	LESS 37	$03^{\rm h}33^{\rm m}36\overset{\rm s}{.}01$	$-27°53'49\overset{''}{.}4$	$3.52^{+0.26}_{-0.36}$	4.0	11 [1]	-24.95	< 6.9	< 37.3	M
LESSJ033144.9-273435	LESS 39	$03^{\rm h}31^{\rm m}45\overset{\rm s}{.}00$	$-27°34'36\overset{''}{.}3$	$2.59^{+0.16}_{-0.06}$	12.6	13 [1]	-24.25	$8.2^{+2.8}_{-1.8}$	$37.7^{+3.3}_{-2.9}$	RM
LESSJ033246.7-275120	LESS 40	$03^{\rm h}32^{\rm m}46\overset{\rm s}{.}77$	$-27°51'20\overset{''}{.}7$	$1.90^{+0.10}_{-0.11}$	3.1	17 [0]	-23.61	$10.5^{+2.0}_{-1.8}$	$39.7^{+2.7}_{-2.8}$	RM
LESSJ033110.5-275233	LESS 41	$03^{\rm h}31^{\rm m}10\overset{\rm s}{.}09$	$-27°52'36\overset{''}{.}3$	$2.74^{+4.26}_{-0.91}$	0.0	4 [0]	-25.56	< 4.0	< 29.9	I
LESSJ033307.0-274801	LESS 43	$03^{\rm h}33^{\rm m}06\overset{\rm s}{.}63$	$-27°48'01\overset{''}{.}9$	$1.67^{+0.23}_{-0.14}$	2.0	8 [9]	-23.35	< 1.3	< 22.8	MI
LESSJ033131.0-273238	LESS 44	$03^{\rm h}31^{\rm m}31\overset{\rm s}{.}19$	$-27°32'38\overset{''}{.}6$	$2.49^{+0.00}_{-0.08}$	2.8	11 [0]	-24.82	$14.8^{+1.7}_{-2.6}$	$43.0^{+2.9}_{-3.1}$	RM
LESSJ033256.0-273317	LESS 47	$03^{\rm h}32^{\rm m}55\overset{\rm s}{.}99$	$-27°33'18\overset{''}{.}9$	$2.90^{+0.14}_{-0.42}$	1.5	8 [6]	-23.77	< 4.5	< 32.7	MI
LESSJ033237.8-273202	LESS 48	$03^{\rm h}32^{\rm m}38\overset{\rm s}{.}00$	$-27°31'59\overset{''}{.}4$	$1.91^{+0.36}_{-0.43}$	0.2	4 [1]	-24.57	$7.5^{+4.8}_{-3.8}$	$35.0^{+4.9}_{-5.8}$	RM
LESSJ033124.5-275040	LESS 49a	$03^{\rm h}31^{\rm m}24\overset{\rm s}{.}45$	$-27°50'37\overset{''}{.}5$	$1.50^{+0.15}_{-0.10}$	5.0	12 [1]	-23.22	$1.8^{+1.0}_{-0.6}$	$25.0^{+2.6}_{-2.4}$	RM
LESSJ033124.5-275040	LESS 49b	$03^{\rm h}31^{\rm m}24\overset{\rm s}{.}69$	$-27°50'46\overset{''}{.}4$	$3.31^{+0.22}_{-0.38}$	0.7	11 [2]	-24.13	$35.9^{+8.5}_{-10.6}$	$58.4^{+4.8}_{-6.4}$	R
LESSJ033141.2-274441	LESS 50a	$03^{\rm h}31^{\rm m}41\overset{\rm s}{.}11$	$-27°44'42\overset{''}{.}4$	$0.85^{+0.16}_{-0.11}$	2.3	17 [0]	-21.91	< 0.3	< 15.9	M
LESSJ033141.2-274441	LESS 50b	$03^{\rm h}31^{\rm m}40\overset{\rm s}{.}97$	$-27°44'34\overset{''}{.}8$	$2.69^{+0.49}_{-0.25}$	7.6	11 [5]	-24.67	$15.1^{+9.0}_{-4.1}$	$45.6^{+6.7}_{-4.3}$	RM
LESSJ033243.6-273353	LESS 54	$03^{\rm h}32^{\rm m}43\overset{\rm s}{.}62$	$-27°33'56\overset{''}{.}6$	$1.84^{+0.62}_{-0.25}$	3.7	7 [6]	-23.35	< 1.6	< 24.1	M
LESSJ033153.2-273936	LESS 56	$03^{\rm h}31^{\rm m}53\overset{\rm s}{.}11$	$-27°39'37\overset{''}{.}3$	$2.46^{+0.41}_{-0.24}$	0.6	9 [8]	-24.38	$5.1^{+3.8}_{-2.0}$	$34.3^{+5.1}_{-3.9}$	RM
LESSJ033152.0-275329	LESS 57	$03^{\rm h}31^{\rm m}51\overset{\rm s}{.}93$	$-27°53'26\overset{''}{.}8$	$2.94^{+0.14}_{-0.11}$	10.8	11 [6]	-24.26	$11.8^{+3.2}_{-2.6}$	$43.6^{+3.6}_{-3.5}$	RM
LESSJ033303.9-274412	LESS 59	$03^{\rm h}33^{\rm m}03\overset{\rm s}{.}62$	$-27°44'12\overset{''}{.}6$	$1.40^{+0.29}_{-0.13}$	1.9	13 [4]	-23.52	$1.3^{+1.2}_{-0.5}$	$23.5^{+3.6}_{-2.5}$	RM
LESSJ033317.5-275121	LESS 60	$03^{\rm h}33^{\rm m}17\overset{\rm s}{.}53$	$-27°51'27\overset{''}{.}5$	$1.64^{+0.10}_{-0.24}$	5.1	17 [0]	-24.01	$4.0^{+1.1}_{-1.6}$	$31.8^{+2.7}_{-3.8}$	RM
LESSJ033236.4-273452	LESS 62	$03^{\rm h}32^{\rm m}36\overset{\rm s}{.}52$	$-27°34'53\overset{''}{.}0$	$1.52^{+0.10}_{-0.21}$	0.8	16 [1]	-24.45	$7.9^{+1.7}_{-2.6}$	$37.5^{+3.1}_{-4.2}$	RM
LESSJ033308.5-280044	LESS 63	$03^{\rm h}33^{\rm m}08\overset{\rm s}{.}49$	$-28°00'42\overset{''}{.}8$	$1.39^{+0.07}_{-0.05}$	2.5	15 [1]	-23.50	$1.3^{+0.6}_{-0.4}$	$23.8^{+2.4}_{-2.4}$	RM
LESSJ033201.0-280025	LESS 64	$03^{\rm h}32^{\rm m}00\overset{\rm s}{.}98$	$-28°00'25\overset{''}{.}3$	$4.19^{+0.04}_{-0.32}$	1.9	11 [4]	-24.31	$12.4^{+4.4}_{-5.4}$	$48.3^{+5.4}_{-6.1}$	RM
LESSJ033331.7-275406	LESS 66	$03^{\rm h}33^{\rm m}31\overset{\rm s}{.}92$	$-27°54'10\overset{''}{.}3$	$2.39^{+0.04}_{-0.05}$	37.2	14 [0]	-25.78	$10.0^{+1.8}_{-1.7}$	$41.0^{+3.4}_{-3.4}$	RM
LESSJ033243.3-275517	LESS 67	$03^{\rm h}32^{\rm m}43\overset{\rm s}{.}18$	$-27°55'14\overset{''}{.}2$	$2.27^{+0.05}_{-0.11}$	3.2	16 [1]	-24.82	$11.9^{+1.6}_{-2.1}$	$42.8^{+3.2}_{-3.4}$	RM
LESSJ033144.0-273832	LESS 70	$03^{\rm h}31^{\rm m}43\overset{\rm s}{.}92$	$-27°38'35\overset{''}{.}2$	$2.31^{+0.15}_{-0.06}$	3.8	17 [0]	-24.48	$44.1^{+7.9}_{-3.7}$	$61.0^{+5.2}_{-4.6}$	RM
LESSJ033229.3-275619	LESS 73	$03^{\rm h}32^{\rm m}29\overset{\rm s}{.}28$	$-27°56'18\overset{''}{.}9$	$4.61^{+0.94}_{-0.59}$	1.1	8 [9]	-24.42	$12.3^{+12.2}_{-6.2}$	$49.3^{+9.9}_{-7.6}$	R
LESSJ033309.3-274809	LESS 74a	$03^{\rm h}33^{\rm m}09\overset{\rm s}{.}34$	$-27°48'15\overset{''}{.}9$	$1.84^{+0.32}_{-0.49}$	0.9	10 [6]	-23.49	$2.8^{+2.2}_{-1.8}$	$29.2^{+4.3}_{-5.8}$	RI
LESSJ033309.3-274809	LESS 74b	$03^{\rm h}33^{\rm m}09\overset{\rm s}{.}14$	$-27°48'16\overset{''}{.}6$	$1.71^{+0.20}_{-0.17}$	2.5	10 [6]	-23.29	$3.00^{+1.6}_{-1.1}$	$29.6^{+3.4}_{-3.1}$	RI
LESSJ033126.8-275554	LESS 75	$03^{\rm h}31^{\rm m}27\overset{\rm s}{.}17$	$-27°55'50\overset{''}{.}9$	$2.46^{+0.06}_{-0.09}$	33.2	15 [0]	-25.39	$11.5^{+2.1}_{-2.2}$	$43.1^{+3.4}_{-3.5}$	RM
LESSJ033221.3-275623	LESS 79	$03^{\rm h}32^{\rm m}21\overset{\rm s}{.}61$	$-27°56'23\overset{''}{.}1$	$1.41^{+0.23}_{-0.17}$	2.2	16 [1]	-23.89	$1.5^{+1.1}_{-0.6}$	$25.4^{+3.4}_{-3.0}$	RM
LESSJ033127.5-274440	LESS 81	$03^{\rm h}31^{\rm m}27\overset{\rm s}{.}54$	$-27°44'39\overset{''}{.}5$	$2.23^{+0.13}_{-0.15}$	27.9	14 [1]	-24.89	$27.7^{+5.0}_{-4.9}$	$54.4^{+5.0}_{-5.1}$	RM

Table 2 – *continued*

SMG[a]	Short name	RA[b]	Dec[b]	$z_{\rm phot}$[c]	$\chi^2_{\rm red}$[d]	Filters[e]	M_H[f] (mag)	L_{FIR}[g] ($10^{12}L_{\odot}$)	T_D[h] (K)	ID type[i]
LESSJ033154.2-275109	LESS 84	$03^{\rm h}31^{\rm m}54\overset{\rm s}{.}49$	$-27°51'05\overset{''}{.}3$	$2.29^{+0.15}_{-0.07}$	3.6	14 [3]	-24.14	$4.5^{+1.8}_{-1.2}$	$34.5^{+3.6}_{-3.4}$	I
LESSJ033251.1-273143	LESS 87	$03^{\rm h}32^{\rm m}50\overset{\rm s}{.}83$	$-27°31'41\overset{''}{.}2$	$3.20^{+0.10}_{-0.81}$	0.1	5 [0]	-24.84	$37.0^{+5.6}_{-19.3}$	$60.1^{+5.9}_{-12.9}$	RM
LESSJ033155.2-275345	LESS 88	$03^{\rm h}31^{\rm m}54\overset{\rm s}{.}81$	$-27°53'40\overset{''}{.}9$	$2.35^{+0.11}_{-0.10}$	1.1	16 [1]	-24.37	$11.7^{+2.3}_{-1.9}$	$44.0^{+4.0}_{-3.9}$	R
LESSJ033313.0-275556	LESS 96	$03^{\rm h}33^{\rm m}12\overset{\rm s}{.}62$	$-27°55'51\overset{''}{.}6$	$2.71^{+0.03}_{-0.09}$	22.0	17 [0]	-26.30	$16.0^{+1.9}_{-2.5}$	$49.7^{+4.4}_{-4.5}$	RM
LESSJ033130.2-275726	LESS 98	$03^{\rm h}31^{\rm m}29\overset{\rm s}{.}89$	$-27°57'22\overset{''}{.}4$	$1.55^{+0.17}_{-0.16}$	1.0	10 [4]	-24.40	$7.8^{+2.8}_{-2.1}$	$39.9^{+4.4}_{-4.3}$	RM
LESSJ033151.5-274552	LESS 101	$03^{\rm h}31^{\rm m}51\overset{\rm s}{.}53$	$-27°45'53\overset{''}{.}1$	$2.39^{+0.36}_{-0.52}$	2.5	10 [7]	-23.51	$3.8^{+2.9}_{-2.3}$	$33.8^{+5.3}_{-6.5}$	R
LESSJ033335.6-274020	LESS 102	$03^{\rm h}33^{\rm m}35\overset{\rm s}{.}56$	$-27°40'23\overset{''}{.}2$	$1.68^{+0.13}_{-0.25}$	1.1	11 [2]	-24.34	< 1.3	< 24.9	M
LESSJ033325.4-273400	LESS 103	$03^{\rm h}33^{\rm m}25\overset{\rm s}{.}37$	$-27°33'58\overset{''}{.}5$	$1.84^{+0.59}_{-0.87}$	0.3	5 [7]	-23.44	< 1.6	< 26.3	M
LESSJ033140.1-275631	LESS 106	$03^{\rm h}31^{\rm m}40\overset{\rm s}{.}17$	$-27°56'22\overset{''}{.}4$	$1.96^{+0.31}_{-0.48}$	2.1	11 [5]	-25.00	$6.3^{+3.4}_{-3.4}$	$38.5^{+5.4}_{-7.2}$	RI
LESSJ033316.4-275033	LESS 108	$03^{\rm h}33^{\rm m}16\overset{\rm s}{.}51$	$-27°50'39\overset{''}{.}3$	$0.20^{+0.03}_{-0.05}$	6.3	15 [0]	-22.75	$0.2^{+0.08}_{-0.08}$	$24.5^{+2.3}_{-2.4}$	RM
LESSJ033122.6-275417	LESS 110	$03^{\rm h}31^{\rm m}22\overset{\rm s}{.}63$	$-27°54'17\overset{''}{.}0$	$2.35^{+4.65}_{-0.44}$	0.0	4 [0]	-23.22	< 2.8	< 31.4	MI
LESSJ033325.6-273423	LESS 111	$03^{\rm h}33^{\rm m}25\overset{\rm s}{.}21$	$-27°34'25\overset{''}{.}9$	$2.61^{+0.14}_{-0.06}$	14.4	13 [0]	-24.49	$9.8^{+3.4}_{-2.3}$	$44.1^{+5.0}_{-4.8}$	RM
LESSJ033249.3-273112	LESS 112	$03^{\rm h}32^{\rm m}48\overset{\rm s}{.}85$	$-27°31'12\overset{''}{.}8$	$1.81^{+0.42}_{-0.30}$	0.7	5 [0]	-24.02	$2.3^{+2.5}_{-1.2}$	$28.5^{+5.8}_{-4.9}$	RI
LESSJ033150.8-274438	LESS 114	$03^{\rm h}31^{\rm m}51\overset{\rm s}{.}08$	$-27°44'37\overset{''}{.}0$	$1.57^{+0.08}_{-0.07}$	1.6	17 [0]	-24.61	$5.3^{+1.1}_{-0.9}$	$36.8^{+3.7}_{-3.7}$	RM
LESSJ033128.0-273925	LESS 117	$03^{\rm h}31^{\rm m}27\overset{\rm s}{.}62$	$-27°39'27\overset{''}{.}3$	$1.73^{+0.29}_{-0.34}$	3.3	9 [4]	-24.23	$5.7^{+3.4}_{-2.6}$	$37.7^{+5.5}_{-6.0}$	R
LESSJ033121.8-274936	LESS 118	$03^{\rm h}31^{\rm m}21\overset{\rm s}{.}91$	$-27°49'34\overset{''}{.}0$	$2.17^{+4.83}_{-1.49}$	1.7	5 [1]	-22.21	$2.8^{+47.5}_{-2.7}$	$31.8^{+48.7}_{-15.6}$	R
LESSJ033328.5-275655	LESS 120	$03^{\rm h}33^{\rm m}28\overset{\rm s}{.}55$	$-27°56'54\overset{''}{.}1$	$1.43^{+0.30}_{-0.21}$	2.2	13 [3]	-23.41	$2.1^{+1.8}_{-0.9}$	$29.2^{+5.0}_{-4.3}$	RM
LESSJ033139.6-274120	LESS 122	$03^{\rm h}31^{\rm m}39\overset{\rm s}{.}52$	$-27°41'19\overset{''}{.}4$	$2.08^{+0.08}_{-0.08}$	5.2	17 [0]	-25.14	$22.4^{+2.8}_{-2.7}$	$55.2^{+6.2}_{-6.2}$	RM
LESSJ033209.8-274102	LESS 126	$03^{\rm h}32^{\rm m}09\overset{\rm s}{.}60$	$-27°41'06\overset{''}{.}9$	$2.02^{+0.17}_{-0.13}$	2.4	12 [4]	-23.84	$2.3^{+1.3}_{-0.9}$	$30.6^{+4.2}_{-4.1}$	MI

[a] The SMG names correspond to those in Weiß et al. (2009) and Biggs et al. (2010).
[b] Coordinates are the J2000 position of the optical/near-infrared counterpart.
[c] Since HYPERZ was restricted to $0 < z < 7$ the six galaxies whose upper redshift limits yield a formal maximum redshift of $z_{\rm max} = 7$ are actually only constrained in the lower redshift limit. Therefore, throughout this paper the redshifts of these galaxies are plotted as lower limits.
[d] The reduced χ^2 of the best-fit SED at the derived photometric redshift.
[e] The number of photometric filters in which each SMG counterpart was detected [and the number of filters in which the SMG was observed but not detected, providing a limiting flux].
[f] M_H is the absolute magnitude in the rest-frame *H*-band.
[g] As discussed in §4.6 the far-infrared luminosity (L_{FIR}) is derived from the infrared-radio correlation using the radio flux and the photometric redshift of each SMG.
[h] The characteristic dust temperature (T_D) is derived as discussed in §4.6 from radio and submillimetre fluxes and the photometric redshift of each SMG.
[i] ID types R, M and I indicate radio, 24 μm and IRAC identified counterparts respectively (see Biggs et al. 2010 for details).
[j] As shown in §4.1 LESS 20 appears to contain a radio-loud AGN. Therefore, the L_{FIR} and T_D presented here are likely significantly overestimated due to the AGN contribution to the radio flux, as such LESS 20 is excluded from our studies of the luminosity function, star-formation rates and star-formation history of SMGs (§4.6).

resistant normalised median absolute deviation (NMAD) of Δz, $\sigma_{\rm NMAD} = 1.48 \times {\rm median}(|\Delta z - {\rm median}(\Delta z)|/(1+z)) = 0.097$. These statistics show that our photometric redshifts are a good proxy for spectroscopic redshift for these sources. However, the median redshift, $z = 0.84$, is lower than that expected for SMGs and the targets are typically brighter at optical wavelengths, limiting the usefulness of these comparisons for the SMGs. Therefore, we also test our photometric redshift calculation on the 30 robust SMG counterparts with available spectroscopic redshifts.

Fig. 1 shows spectroscopic redshift against $\Delta z/(1+z)$ for the 30 robust LESS SMG counterparts with spectroscopic redshifts from archival surveys of the ECDFS (10 counterparts) and our spectroscopic survey of SMGs in the ECDFS (20 counterparts). Quality flags are published in many catalogues and where possible we distinguish between high- and low-quality spectroscopic redshifts. The median $\Delta z/(1+z)$ for SMGs is 0.023 ± 0.021 (here are throughout this paper errors on median measurements are from bootstrapping) the mean $\Delta z/(1+z) = -0.013 \pm 0.178$, and $\sigma_{\rm NMAD} = 0.037$, suggesting that for SMGs our photometric redshifts are reliable. We caution that the SMGs without reliable spectroscopic redshifts are fainter on average than the SMGs with spectroscopic redshifts, which could affect the quality of their photometric redshifts. Although the median R-band magnitude of the SMGs detected in the MUSYC survey is the same for the counterparts with and without spectroscopic redshifts, all of the 30 SMGs with spectroscopic redshifts are detected in the MUSYC R band, while only 18 of the 45 SMGs without spectroscopic redshifts are detected.

Dunlop et al. (2009) have independently calculated photometric redshifts for the six LESS SMGs (five with robust counterparts) in GOODS-South that were also detected by BLAST at 250 μm (Devlin et al. 2009). Their photometry uses imaging from *HST* (B_{435}, V_{606}, i_{775}, z_{850}), the VLT (J, H, K) and *Spitzer* (3.6, 4.5, 5.8 and 8 μm) and they use HYPERZ with the stellar population models of Charlot & Bruzual (e.g. Bruzual 2007) which have a Salpeter IMF. In all cases the (Dunlop et al. 2009) photometric redshifts agree with those presented in Table 2, providing further confidence that our photometric redshifts are reasonable for SMGs.

To assess the level of systematic uncertainties for the derived photometric redshifts due to the adopted methodology, SED tem-

plates, and/or photometric data, we also use the Zurich Extragalactic Bayesian Redshift Analyzer (ZEBRA; Feldmann et al. 2006) to calculate photometric redshifts. Our adopted procedure is similar to that discussed in §3.2 of Luo et al. (2010). Briefly, we use ZEBRA to obtain a maximum-likelihood estimate for the photometric redshifts of individual galaxies or AGNs using an initial set of 265 galaxy, AGN, and galaxy/AGN hybrid SED templates. These SED templates were then expanded to 463 templates during the template-training mode of ZEBRA to best represent the SEDs of the ≈ 2 Ms CDFS X-ray sources (Luo et al. 2010), including AGN. Besides the different SED templates used, this method differs from the HYPERZ approach described in §3.1 in some additional details such as how the redshift intervals and minimum photometric errors are determined; see §3.2 of Luo et al. (2010) for details.

The ZEBRA-derived photometric redshifts ($z_{\rm phot,check}$) were compared to those listed in Table 1 ($z_{\rm phot}$); the difference was measured by $\delta z_{\rm phot} = (z_{\rm phot,check} - z_{\rm phot})/(1 + z_{\rm phot})$. For sources with secure spectroscopic redshifts, individual $|\delta z_{\rm phot}|$ values range from ≈ 0.01 to 0.10, indicating that both methods are able to deliver photometric redshifts to a similar accuracy. For the full sample, the mean (median) value of $\delta z_{\rm phot}$ is -0.006 (0.011), with an rms scatter of 0.028, suggesting that the photometric redshifts in Table 1 are fairly robust. After accounting for the effective 1σ errors of the photometric redshifts, only three (sources LESS 7, LESS 37 and LESS 111) of the 74 sources have inconsistent $z_{\rm phot}$ and $z_{\rm phot,check}$. As some sources have photometry data in addition to those presented in Table 2, we also tested the effect of including more data points. The photometric redshifts differ by a mean value of $|\delta z_{\rm phot}|$ of 0.024 with an rms error of 0.030, after including the WFI R-band data (Giacconi et al. 2002; Giavalisco et al. 2004) for 25 sources and the *GALEX* near-UV and far-UV data (Morrissey et al. 2007) for 3 sources. Given the small difference caused by the additional data, we consider the consistent aperture photometry in Table 2 suitable for the purpose of deriving reliable photometric redshifts.

3.3 Sample subsets

As discussed in §1, Biggs et al. (2010) identified robust counterparts to 71 SMGs (of which 68 have detectable optical counterparts) and tentative counterparts to 26 LESS SMGs, respectively. In Fig. 2 we compare the redshift distributions of the robust and tentative counterparts to determine whether our results may be biased by the exclusion of tentative counterparts in our main analysis. The median redshifts of robust and tentative counterparts are 2.2 ± 0.1 and 2.0 ± 0.2 and the interquartile ranges are $z = 1.8$–2.7 and $z = 1.2$–2.8, respectively. We also use a Kolmogorov-Smirnov test (KS-test), which calculates the probability that two samples are drawn from the same parent population (P_{KS}), to compare the redshift distributions of robust and tentative counterparts statistically. We find $P_{KS} = 0.09$ and conclude that it is likely that there is some contamination from physically unassociated foreground ($z \lesssim 1$) galaxies in the tentative identifications. Therefore, throughout the remainder of this paper we restrict our analysis to robust counterparts.

We note that our identified sample may contain a small number of potential gravitational lenses. These are typically low-redshift counterparts where the radio or mid-infrared emission is offset from the optical source. These are discussed individually in Appendix A and we have confirmed that their inclusion does not affect our results.

In Fig. 2 we also compare the redshift distributions of counterparts with $p \leqslant 0.05$ in the radio, 24 μm and IRAC data. The median redshifts are $z = 2.3 \pm 0.1$, 2.1 ± 0.2 and 2.3 ± 0.2, and the interquartile ranges are $z = 1.8$–2.8, 1.6–2.5 and 1.9–2.7 for the radio, 24μm and IRAC samples respectively. A comparison of the three redshift samples shows that they are statistically indistinguishable. We conclude that the three counterpart identification methods select galaxies with similar redshift distributions, and are not significantly biased with respect to each other.

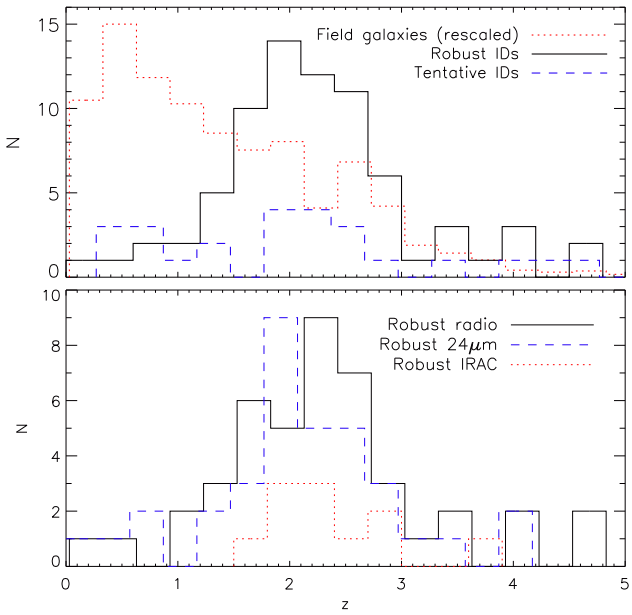

Figure 2. In the top panel we present a comparison between robustly and tentatively identified SMG counterparts and the field population of the ECDFS; tentative counterparts and field galaxies are offset slightly in redshift for clarity. The robust counterparts have a median redshift of $z = 2.2 \pm 0.1$, compared to $z = 2.0 \pm 0.2$ for the tentative counterparts. Tentative counterparts have a larger interquartile range – 1.2–2.8 compared to 1.8–2.7 for the robust SMG counterparts. We interpret these distributions as evidence that tentative counterparts are mainly drawn from the same parent population as the robust counterparts, but with the addition of some contamination, particularly at low redshifts. In the lower panel we compare the redshift distributions of robust counterparts (with $p \leqslant 0.05$) in radio, 24 μm and IRAC data; for clarity radio and 24 μm counterparts are plotted offset slightly in redshift. The radio, 24 μm and IRAC samples have median redshifts of 2.3 ± 0.1, 2.1 ± 0.2 and 2.3 ± 0.2 and interquartile ranges of 1.8–2.8, 1.6–2.5 and 1.9–2.7 respectively. Therefore, we find no significant differences in the redshift distributions of the three identification methods.

3.4 The effect of AGN on photometric redshifts

As discussed in §3.1 our photometric redshift calculations are based on fitting stellar templates to the SMG photometry. However, studies have shown that the 8 μm flux in SMGs with a luminous AGN component can be dominated by the AGN and therefore fitting stellar templates may yield misleading results (Hainline et al. 2009, 2010; Coppin et al. 2010b).

We employ two methods to identify potential AGN in the LESS SMGs. Firstly, we cross-correlate the LESS SMG counterparts with the *Chandra* X-ray catalogues of the CDFS (Luo et al. 2008) and ECDFS (Lehmer et al. 2005) with a matching radius of $1''$. This yields 12 X-ray luminous SMG counterparts (16% of the robust LESS counterparts). Secondly, we identify nine SMG coun-

terparts (12% of the robust LESS counterparts) with a large excess of 8 μm flux compared to the best-fit SED template, which potentially indicates obscured power-law emission from an AGN. In total this yields 16 SMG counterparts (22% of the robust LESS counterparts) which may contain AGN (five are both X-ray detected and have an 8 μm excess).

To determine whether AGN contamination in the 8-μm filter reduces the accuracy of our photometric redshift estimates we re-fit the photometry of the counterparts which display an 8-μm excess whilst excluding the 8 μm photometry. Spectroscopic redshifts are available for eight of the affected galaxies and we find that the average $|\Delta z|$ of these eight galaxies is not significantly decreased, while the median reduced χ^2 drops by 1.2, when the 8 μm photometry is excluded from the fitting. This result does not change if we also exclude the 8 μm photometry of the SMGs which are X-ray detected.

It is also possible that our sample of SMG counterparts contains AGN which enhance the 8 μm flux but do not cause a detectable excess. Therefore, we also exclude the 8 μm photometry of *all* the SMG counterparts during the fitting procedure. Once again the average $|\Delta z|$ for the spectroscopic sample does not change significantly (median $\Delta z/(1+z) = 0.032 \pm 0.021$, compared to median $\Delta z/(1+z) = 0.023 \pm 0.021$ originally). These results indicate that when calculating photometric redshifts the benefit of including the longer-wavelength data is greater than the bias which is removed by ignoring the 8 μm photometry. Therefore, we include the 8 μm photometry in the SED fitting.

3.5 Reliability of SED parameters

In addition to calculating photometric redshifts, HYPERZ also returns the spectral type, age and reddening of the best-fit SED template. To test the sensitivity of the choice of template we refit the photometry of the SMGs allowing only the Burst template, and then only a constant star-formation rate history (Im). These two templates represent the extremes of the star-formation histories and so they will let us gauge the sensitivity of the derived parameters to the choice of the best-fit template.

We compare the quality of the Burst and Im fits of each galaxy with $\Delta\chi^2_{\rm red}$ – the difference in the reduced χ^2 of the Burst and Im fits. We find that 63% of the SMGs have $|\Delta\chi^2_{\rm red}| \leqslant 1$ and as such the Burst and Im templates are indistinguishable at the 99% level for these SMGs. 61% (17) of the SMGs with $|\Delta\chi^2_{\rm red}| > 1$ between the two template fits are best-fit by Bursts and 39% (11) by Im templates. If three templates – Burst, Sb and Im – are considered the star-formation histories of only 23% (17) of all the SMG counterparts can be distinguished. Therefore, although it may be possible to crudely distinguish the star-formation histories of a fraction ($\sim$ 20–40%) of SMG counterparts with HYPERZ, the star-formation histories of most SMGs counterparts cannot be reliably established.

We find that the SMGs that have SED fits with $|\Delta\chi^2_{\rm red}| \leqslant 1$ and can be equally well fit by either Burst or Im templates have different age estimates depending on the template. The age and star-formation history of a stellar population affects the light-to-mass ratio; thus our inability to distinguish between star-formation histories leads to uncertainties in the light-to-mass ratios and stellar mass estimates. Using the H-band light-to-mass ratios for Burst and Im models from the STARBURST99 stellar population model (Leitherer et al. 1999) we calculate that the uncertainties in SED fitting parameters result in a 1σ dispersion of a factor of 4.6 range in the light-to-mass ratios and consequently in the stellar mass estimates (see also Fig. 9).

We also compare reddening measurements for those galaxies with SED fits with $|\Delta\chi^2| \leqslant 1$ and find that on average the difference between A_V for the best-fit Im and Burst templates, ΔA_V, is equal to 0.32 ± 0.16. Since average estimates based on either template return the same value of A_V (to $\sim 2\sigma$) we conclude that average reddening measurements for the SMG population are not strongly sensitive to the adopted star-formation history and are likely to be statistically meaningful (although we caution against trusting values for individual SMGs). When fitting E, Sb, Burst, or Im templates and allowing $A_V = 0$–5, as in our photometric redshift calculations we determine a median $A_V = 1.5 \pm 0.1$ and 96% of SMGs have $A_V \leqslant 3$. We conclude that in most instances restricting to $A_V \leqslant 3$ is sufficient for calculating photometric redshifts of SMGs. We note that these values of A_V are integrated across the whole galaxy and that obscuration in the regions responsible for the majority of the far-infrared/submillimetre emission is considerably larger (e.g. Chapman et al. 2004b; Takata et al. 2006; Ivison et al. 2010b).

4 RESULTS AND DISCUSSION

In §3 we derived reliable photometric redshifts for 74 counterparts to 68 robustly identified SMGs. We now use these photometric redshifts and the SED fits to further investigate the properties of SMGs.

4.1 Photometric redshifts

In Fig. 3 we show our photometric redshift distribution for the 74 robust SMG counterparts; it peaks at $z = 2.2 \pm 0.1$ and has an interquartile range of 1.8–2.7. We compare to the photometric redshift distribution of SMG counterparts in the SCUBA Half-Degree Extragalactic Survey (SHADES) (Clements et al. 2008; Dye et al. 2008), median $z = 1.5 \pm 0.1$, and the spectroscopic sample from Chapman et al. (2005), median $z = 2.2 \pm 0.1$, both of which have similar submillimetre flux limits as our survey. The LESS SMGs have a similar redshift distribution to Chapman et al. (2005), although in LESS the spectroscopic 'redshift desert' at $z \sim 1.2$–1.8 is filled and there is a larger high-redshift tail. The redshift distributions of both LESS and Chapman et al. (2005) SMGs are peaked at higher redshifts than the SHADES SMGs. A KS-test between Chapman et al. (2005) and LESS SMGs yields $P_{KS} = 0.44$, suggesting the two samples appear to be drawn from the same parent population. However, a KS-test between the LESS and SHADES SMGs gives $P_{KS} = 1.3 \times 10^{-5}$ indicating that these samples are likely drawn from intrinsically different populations.

We conclude that the global properties of our photometric redshifts are consistent with the largest previous spectroscopic survey, albeit with a higher-redshift tail – we find 10 (14%) SMGs with $z \geqslant 3$ and eight (11%) with $z \geqslant 3.5$, of which LESS 73 is spectroscopically confirmed at $z = 4.76$ (see Coppin et al. 2009, 2010a). It is likely that the larger number of high-redshift sources in the LESS survey compared to Chapman et al. (2005), where there are 10% at $z \geqslant 3$ and just 1% at $z \geqslant 3.5$, is due to deeper radio data (on average) and the inclusion of 24-μm counterparts in LESS (Biggs et al. 2010) and most critically the use of photometric redshifts covering the UV to mid-infrared which are less reliant on the detection of spectral features in the optical. Conversely, the SHADES SMGs appear to typically lie at lower redshifts. We stress that compared to the SHADES analyses we have used about twice

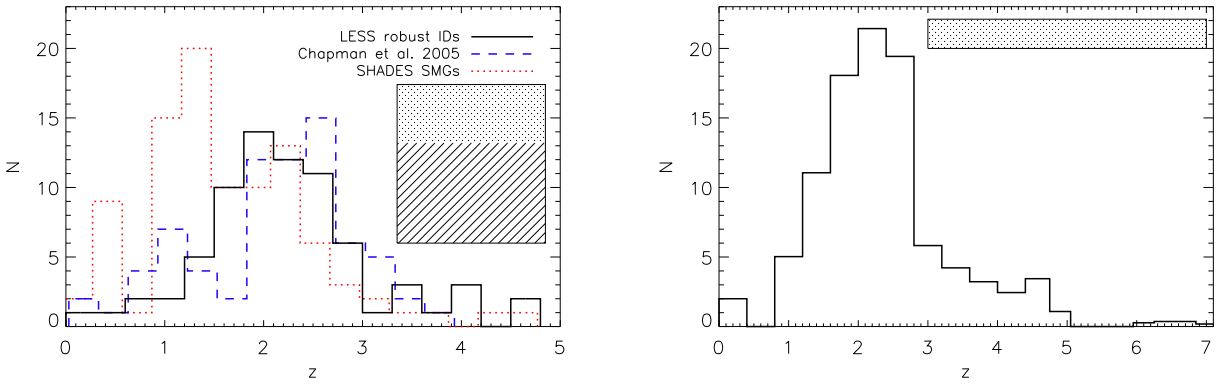

Figure 3. [left] The photometric redshift distribution of the LESS SMGs. We compare this to the photometric redshift distribution of SHADES SMG counterparts (Clements et al. 2008; Dye et al. 2008), and the spectroscopic redshift distribution of SMGs from Chapman et al. (2005); for clarity the SHADES and Chapman et al. (2005) samples are offset slightly in redshift. The median redshift of identified SMGs in LESS is $z = 2.2 \pm 0.1$, which is the same as that from the Chapman et al. (2005) spectroscopic survey; SHADES has a lower median redshift of $z = 1.5 \pm 0.1$. There is a slightly larger high-redshift tail in the LESS SMG population than the Chapman et al. (2005) SMG population. Additionally, the so-called 'redshift desert' at $z \sim 1.5$, which is evident in the Chapman et al. (2005) study does not affect our photometric redshifts and as such, in contrast with Chapman et al. (2005), the increase in the number of galaxies from $z \sim 1$ to $z \sim 2$ is smooth. Statistical comparisons show that the Chapman et al. (2005) and LESS SMGs are most likely drawn from populations with similar redshift distributions, but that the SHADES SMGs are biased to low redshifts either from systematic errors in the photometric redshift calculations, sample selection, or cosmic variance. The shaded region represents the area that would be added to the histogram were the redshifts of the 57 statistically identified or completely unidentified SMGs known and is designed to give an impression of the potential contribution of the unidentified SMGs to this figure. The lower region corresponds to the unidentified SMGs that we statistically identify in §4.2, and which have redshifts similar to the identified SMGs. The upper shaded region represents the SMGs which remain unaccounted for after the statistical analysis and likely have $z \gtrsim 3$. [right] The same distribution but now including the statistically identified SMG population from §4.2 in addition to the identified sample. These are distributed uniformly within the relevant $\Delta z = 1$ ranges. The shaded area now represents the remaining unidentified SMGs, which are likely to lie at $z \gtrsim 3$. We conclude that the median redshift of the $S_{870\mu m} \gtrsim 4$ mJy SMG population is likely to be $z = 2.5 \pm 0.6$.

as many photometric bands, tested against a larger spectroscopic sample of SMGs, and obtained qualitatively better fits to the SEDs. We suggest that either there is a systematic error in the original SHADES photometric redshifts or their counterpart identifications, or that cosmic variance is the cause of the different redshift distributions. However, we note that a re-analysis of the optical-to-infrared photometry of the SHADES SMGs yields a median photometric redshift of $z = 2.05$ (Schael et al. in prep.) – more similar to LESS and Chapman et al. (2005) than the original SHADES analyses.

Studies have suggested that the brightest SMGs may have higher redshifts than those with lower submillimetre fluxes (e.g. Ivison et al. 2002; Pope et al. 2005; Biggs et al. 2010). In Fig. 4 we plot the photometric redshift against 870 μm flux ($S_{870\mu m}$) for robust LESS SMG counterparts. We split the galaxies into those brighter and fainter than the median deboosted submillimetre flux of the sample, $S_{870\mu m} = 5.6$ mJy (we use deboosted 870-μm fluxes through out). SMGs with $S_{870\mu m} \leqslant 5.6$ mJy have a median redshift of $z = 2.1 \pm 0.2$ and SMGs with $S_{870\mu m} > 5.6$ mJy have a median redshift of $z = 2.3 \pm 0.2$, where the errors are bootstrap uncertainties on the medians. Spearman's rank correlation coefficient between $S_{870\mu m}$ and $z_{\rm phot}$ is 0.20, which corresponds to a probability of zero correlation of 0.08 and indicates that there is no significant correlation between submillimetre flux and redshift for SMGs in our sample. We have verified that the result is not dependent on the choice of the flux limit between the two bins. Additionally, if all the unidentified SMGs lie at $z = 5$ or $z = 1$ (in §4.2 both of these scenarios are shown to be unlikely) we still find no statistically significant difference between the redshifts of SMGs in the two flux bins. The sample of SMGs with optical-infrared photometric redshifts in this work is larger than previous studies of this phenomenon and our analysis finds no significant correlation between $S_{870\mu m}$ and redshift for robustly identified sources, also implying that $S_{870\mu m}$ is not a good proxy for redshift. This result agrees with Knudsen et al. (2010), who find no difference in the redshift distributions of faint lensed SMGs ($S_{850\mu m} < 2$ mJy) and the brighter ($S_{850\mu m} \gtrsim 3$ mJy) SMGs from Chapman et al. (2005).

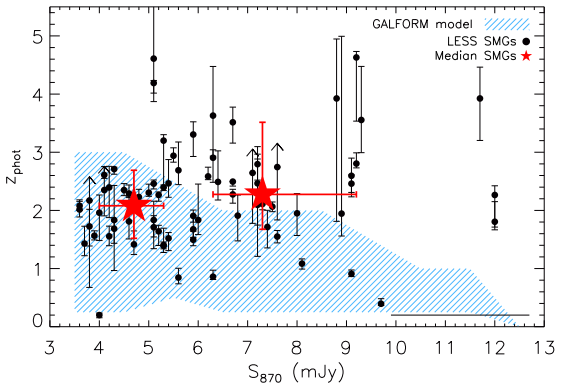

Figure 4. Photometric redshift versus submillimetre flux for LESS SMGs; the median $S_{870\mu m}$ error bar is shown in the bottom right. The median $S_{870\mu m}$ and redshift, with 1σ error bars, are presented for SMGs with $S_{870\mu m} \leqslant 5.6$ mJy and $S_{870\mu m} > 5.6$ mJy. Previous studies have suggested that the brightest SMGs may lie at the highest redshifts. This work contains optical-infrared photometric redshifts for a larger sample of SMGs than previous studies of the phenomenon and finds no evidence for a trend. For comparison we also highlight the 1-σ distribution of SMGs in flux bins of 1 mJy in the ΛCDM GALFORM model (Baugh et al. 2005; Lacey et al. 2008; Swinbank et al. 2008).

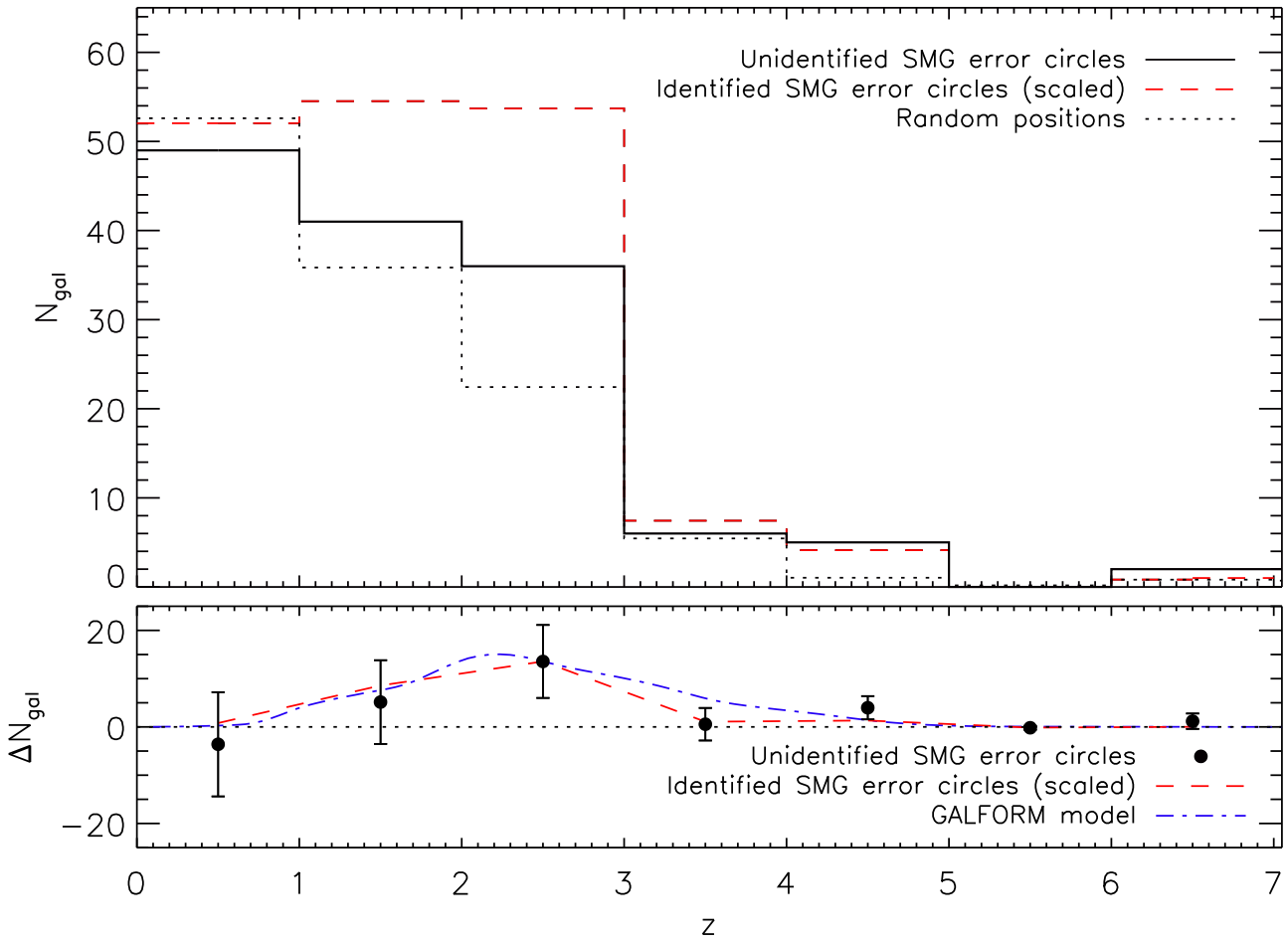

Figure 5. The top panel shows the redshift histogram of sources within the submillimetre positional error circles of SMGs without robust radio, 24 μm or IRAC counterparts compared to the same number of random positions in the field. For comparison we also plot the redshift histogram for sources in the submillimetre positional error circles of SMGs *with* robust counterparts, also scaled to the same number of error circles. In the bottom panel we show the difference between the redshift histogram of galaxies around unidentified SMGs and the field population (from random positions). We also plot both the difference in redshift of galaxies around identified SMGs and the field population, and the redshift distribution of radio-undetected SMGs in the ΛCDM GALFORM model (Swinbank et al. 2008). In order to highlight potential differences in the redshift distributions of the populations the latter two datasets are scaled to match the value of $\Delta N_{\rm gal}$ of unidentified SMGs in the $z = 2$–3 bin. By using $\Delta N_{\rm gal}$ and assuming a uniform distribution of galaxies within the bins we calculate that the average redshift of unidentified SMGs is $z = 2.5 \pm 0.3$.

We note that SMGs in the semi-analytic ΛCDM GALFORM model (Baugh et al. 2005; Lacey et al. 2008; Swinbank et al. 2008) also show no correlation between $S_{870\mu m}$ and redshift (although the error range decreases at high fluxes where there are few galaxies in the model).

4.2 Redshift distribution of unidentified SMGs

To date, redshift surveys of SMGs have focused on the $\sim$ 60–80% of the population with counterparts identified from radio and 24 μm imaging, and a few located using high-resolution (sub-)millimetre interferometry. The requirement for radio or infrared counterparts to SMGs can bias the redshift or the dust temperature distributions of identified SMGs (Chapman et al. 2005) and it is currently unknown if the identified population is representative of the $\sim$ 20–40% of SMGs without identified counterparts. In particular, it is unclear whether they have the same redshift distribution. In order to investigate the redshift distribution of the unidentified SMGs we utilise our extensive 17-band photometric redshifts in the ECDFS to investigate the photometric redshifts of sources around SMGs without robustly identified counterparts to the field population.

In Fig. 5 we show the redshift histogram of galaxies within the error circles of the 55 unidentified SMGs in the ECDFS, where the region considered is that used by Biggs et al. (2010) to identify SMG counterparts (both the completely unidentified and those with only tentative identifications). For comparison, we show the redshift histogram of all the galaxies in the submillimetre error circles of SMGs with robustly identified counterparts, scaled such that the number of error circles examined is the same as the unidentified SMG sample. We also consider the photometric redshifts of galaxies in the same area around random positions in the field, which are required to be $> 15''$ from any LESS SMGs. We consider 50 Monte Carlo simulations of 55 random field positions (equal to the number of unidentified SMGs), and employ the mean and standard deviation of the 50 simulations in each redshift bin for our statistical analyses. As discussed in §2.1 our photometric source extraction procedure included manually examining the regions around the SMGs and adding to the catalogue potential sources which may

have been missed by the automated procedure. To remove any bias and ensure a fair comparison between the SMGs and random positions, we exclude these additional sources from this analysis.

In the lower panel of Fig. 5 we show the difference between the redshift distributions of the field and SMGs without robustly identified counterparts. Compared to the field there is an excess of 26 ± 12 (2.2σ) at $z > 1$ around unidentified SMGs. There are positive excesses of galaxies in the $z = 2$–3 (14 ± 8; 1.8σ) and $z = 4$–5 (4 ± 2; 1.6σ) bins around unidentified SMGs. This suggests that the peak of the redshift distribution of the population of radio, 24-μm and IRAC unidentified SMGs is at $z = 2$–3.

To crudely compare the redshift distributions of the identified and unidentified SMGs we also plot the difference between redshifts of sources in the submillimetre error circles of the identified SMGs to the field (scaled to the value in the $z = 2$–3 bin of the unidentified SMGs). We conclude that the redshift distribution of unidentified SMGs is broadly similar to that of robustly identified SMGs.

To provide a more reliable estimate of the average redshift of the unidentified SMGs we evenly distribute the excess galaxies in the SMG error circles in each redshift bin. We verify that this method is valid by using it to calculate the average redshift for identified SMGs, which yields $z = 2.2 \pm 0.1$, in agreement with that derived using the robust counterparts alone (§4.1). For unidentified SMGs we derive an average redshift of $z = 2.5 \pm 0.3$. This suggests that unidentified SMGs may lie at marginally higher redshifts than the identified sample, although we stress that the difference is not statistically significant. This conclusion is consistent with the predicted redshift distribution of radio undetected SMGs from the semi-analytic ΛCDM GALFORM model, which predicts they should lie at $z \sim 2.2$, similar to the observed SMGs (Swinbank et al. 2008).

There are 14 ± 8 more galaxies at $z = 2$–3 in the error circles of unidentified SMGs than expected from comparing to the field population. We showed in §3.3 that there are nine tentative SMG counterparts with $z = 2$–3 and two with $z = 4$–5. Thus potentially half of the excess seen around the unidentified SMGs could be attributed to tentative counterparts. Indeed, if tentative SMGs are removed from this analysis a 0.6σ (3 ± 5) excess of $z = 2$–3 galaxies and a 1.3σ (2.4 ± 1.9) excess of $z = 4$–5 galaxies around SMGs remains.

Finally, we use statistical arguments to estimate how many SMGs are still unaccounted for. There are 55 out of the sample of 126 LESS SMGs without robust radio, 24 μm or IRAC counterparts (Biggs et al. 2010). Due to the signal-to-noise ratio limit on the submillimetre catalogue ($S/N \geqslant 3.7\sigma$) five of the 126 SMGs are expected to be false detections (Weiß et al. 2009); an additional 1–2 are expected to have counterparts outside of the search radii used (Biggs et al. 2010). This leaves 48–49 SMGs with currently unidentified counterparts that are expected to lie within our search area. We then calculate the total excess of galaxies in unidentified error circles over the field. Due to clustering, an error circle can contain more than one galaxy associated with the SMG. We then compare the sources around identified SMGs with the number of identified counterparts to determine this "overcounting factor": $\sim 1.2\times$. We scale the difference between the field and unidentified SMG regions by this factor to estimate that there are 21 ± 19 LESS SMGs ($17 \pm 15\%$ of the total) which are still unaccounted for. These have no robust radio, 24 μm and IRAC counterparts and have mid-infrared fluxes below the limits of our imaging.

These counterparts could lie at $z \sim 1$–3 and be fainter than $M_H \lesssim -23$ (Fig. 10). However, the specific star-formation rates of such sources would be $\gtrsim 10^{-7}\,\mathrm{yr}^{-1}$, corresponding to life times of $\lesssim 10\,\mathrm{Myr}$. The corresponding duty cycle for such short-lived sources means that to detect ~ 20 sources in our $0.5\,\mathrm{deg}^2$ survey, we require a parent population with a space density of $\gtrsim 0.02\,\mathrm{Mpc}^{-3}$, which we consider unlikely. Alternatively, if they have restframe near-infrared luminosities similar to the identified SMG population, then Fig. 10 suggests that they must lie at $z \gtrsim 3$. If correct we should add these sources to the SMGs identified at $z \gtrsim 3$. We have identified 10 SMGs at $z > 3$, as well as 4 ± 2 which have been statistically identified in our IRAC sample. To these we add the 21 ± 19 SMGs which are unaccounted for in our statistical analysis, to derive a total of 35 ± 19 SMGs ($28 \pm 15\%$ of the whole population) at $z \geqslant 3$ in our survey. We conclude that $\sim 30\%$, and at most $\sim 45\%$ of the SMG population could reside at $z \gtrsim 3$. This corresponds to a volume density of $2.8 \times 10^{-6}\,\mathrm{Mpc}^{-3}$ (assuming they span the range $z = 3$–7, or 80% higher if they only span $z = 3$–5). For comparison, the equivalent volume density of $z = 2$–3 SMGs, including identified counterparts and the 14 that are statistically identified in this redshift range, is $1.2 \times 10^{-5}\,\mathrm{Mpc}^{-3}$, signifying strong evolution in the abundance of SMGs from $z > 3$ to $z \sim 2.5$.

We have statistically identified the redshifts of $\sim 60\%$ of the unidentified SMGs, and shown that the remainder likely lie at $z \gtrsim 3$. In the right-hand panel of Fig. 3 we combine the redshift distributions of the identified and unidentified SMGs to provide the probable redshift distribution of the *entire* $S_{870\mu m} \gtrsim 4$ mJy SMG population. We conclude that the most likely median redshift for the $S_{870\mu m} \gtrsim 4$ mJy SMG population is $z = 2.5 \pm 0.6$.

4.3 Simple redshift estimators for SMGs

Previous studies have investigated and used optical (BzK), ultraviolet (BX/BM; Steidel et al. 2004; Chapman et al. 2005) and IRAC colours (Yun et al. 2008; Hainline et al. 2009) and radio-to-submillimetre flux ratios (e.g. Carilli & Yun 1999; Ivison et al. 2007; Biggs et al. 2010) as simple estimators of the redshifts of SMGs. Here we use our 17-band photometric redshifts to investigate the reliability of such the BzK colours and radio-to-submillimetre fluxes as redshift estimators and derive a simple IRAC colour indicator of redshift.

In Fig. 6 we show the BzK colour-colour plot (Daddi et al. 2004), which is designed to identify galaxies at $1.4 < z \lesssim 2.5$, for LESS SMG counterparts. We have distinguished between counterparts with photometric redshifts above and below $z = 1.4$ and find that all the SMGs with $z_{\mathrm{phot}} < 1.4$ lie in the expected region of colour-colour space. However, whilst SMG counterparts with $z_{\mathrm{phot}} \geqslant 1.4$ typically have the colours of high-redshift star-forming galaxies, this population does scatter into the low-redshift region. Two galaxies with $z_{\mathrm{phot}} > 1.4$, $B - z \sim 1$ and $z - K \sim -0.1$ lie near the separation between $z < 1.4$ galaxies and stars and are both X-ray luminous, bright unresolved sources which may be submillimetre-bright quasars (see Appendix A). We conclude that the BzK analysis of SMG counterparts can select clean but incomplete samples of $z > 1.4$ SMGs, and that samples selected to have $z < 1.4$ will contain $\sim 45\%$ contamination from galaxies at higher redshift. We compare the observed BzK colours with a redshift track of the average SMG SED (§4.4) and note that the median SED of SMGs has a redder restframe $(U - z)$ colour (corresponding to observed $(z - K)$ at $z \sim 1.4$) than used to define the selection areas for $z > 1.4$ galaxies and that the SMGs at the highest redshifts may fall in the passive BzK or $z < 1.4$ region.

In Fig. 7 we plot the photometric redshift against

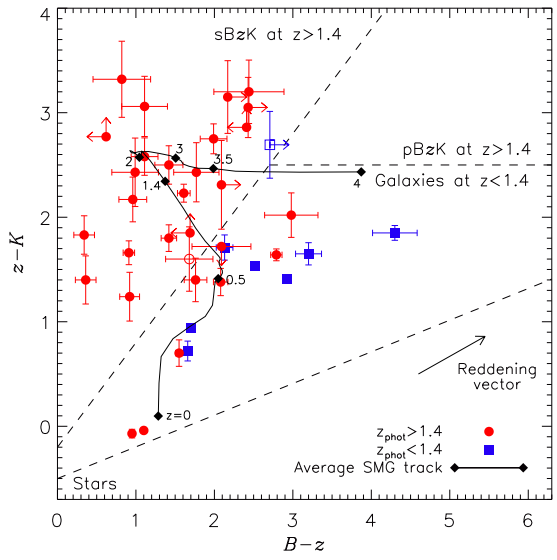

Figure 6. $(B-z)$ versus $(z-K)$ colour-colour plot of LESS SMG counterparts. The selection regions for star-forming and passive $z>1.4$ BzK galaxies (sBzK and pBzK respectively), $z<1.4$ galaxies, and stars (Daddi et al. 2004) are shown, and we distinguish between SMG counterparts with $z_{\rm phot}\geqslant 1.4$ and $z_{\rm phot}<1.4$. The photometric redshifts typically agree with the BzK colours and most of the SMG counterparts have BzK colours of $z>1.4$ star-forming galaxies and none have colours of stars or $z>1.4$ passive galaxies (similar to the result of Bertoldi et al. 2007). All of the counterparts with sBzK colours are found to have $z_{\rm phot}\geqslant 1.4$, but galaxies with BzK colours suggesting $z<1.4$ have a $\sim 45\%$ contamination from counterparts with $z_{\rm phot}\geqslant 1.4$. We also show the redshift track of the average SMG SED (§4.4) from $z=0$–4 and the reddening vector for $A_V=1$ mag. The scatter in the photometry of individual SMGs compared to the redshift track of the average SMG SED suggests that the SMGs have a range in optical SEDs. Open symbols show galaxies which lie in halos of bright stars in the z-band, in these cases, for the purpose of this plot only, the z-band magnitude is extrapolated from the SED fit and the measured I-band magnitude.

$S_{870\mu m}/S_{1.4{\rm GHz}}$ for the LESS SMGs (Weiß et al. 2009; Biggs et al. 2010), the tracks of Arp 220 and M82 (based on the SEDs of Silva et al. 1998). We also show the ΛCDM GALFORM predictions (Baugh et al. 2005) and the Carilli & Yun (2000) relationship. The wide range in $S_{870\mu m}/S_{1.4{\rm GHz}}$ at a fixed redshift limits the usefulness of $S_{870\mu m}/S_{1.4{\rm GHz}}$ as a redshift indicator for SMGs and indicates that SMGs have a variety of submillimetre-to-radio flux ratios, suggesting a range in dust temperatures (Chapman et al. 2005; Clements et al. 2008). We also note that the majority of SMGs lie above the redshift track of M82, suggesting higher submillimetre-to-radio flux ratios (potentially due to the presence of more cold dust). LESS 20 has $z_{\rm phot}\sim 2.8$ and $S_{870\mu m}/S_{1.4{\rm GHz}}\sim 1.7$, which is significantly lower than expected from its redshift, indicating that it is most likely a radio-bright AGN, so we remove it from our subsequent analyses of far-infrared luminosities, star-formation rates, and characteristic dust temperature (§4.6).

Studies of mid-infrared spectra of SMGs have shown that they are similar to M82 with an additional power-law contribution from AGN emission (Menéndez-Delmestre et al. 2007, 2009; Pope et al. 2008; Coppin et al. 2010b). In Fig. 7 we plot photometric redshift against $S_{870\mu m}/S_{24\mu m}$, which shows that the mid-infrared to submillimetre flux ratios of SMGs are similar to Arp 220 and those derived in the ΛCDM GALFORM model, but are poorly represented by M82. This suggests that although SMGs have mid-infrared spectra similar to M82, the mid-infrared continuum emission is fainter compared to the far-infrared emission and is more comparable to that of Arp 220. We note that although $S_{870\mu m}/S_{24\mu m}$ for SMGs varies with redshift in a manner comparable to Arp 220, the scatter and the effect of PAH and silicate features passing through the 24 μm filter makes this measurement unsuitable for redshift derivation (Pope et al. 2006).

We expand on the work of Yun et al. (2008) and Hainline et al. (2009) and propose a new redshift estimator for SMGs, which is based on the IRAC 8 and 3.6 μm fluxes and exhibits less scatter than the commonly-employed radio-to-submillimetre flux ratio. In Fig. 8 we plot this ratio against redshift for the LESS SMGs and using the ROBUST_LINEFIT procedure from the IDL Astronomy Library (Landsman 1993) we fit an outlier-resistant linear relationship to SMGs with $z_{\rm phot}<4$, which yields:

$$z=(2.1\pm0.1)+(1.9\pm0.2)\log_{10}(S_8/S_{3.6}) \quad (1)$$

We exclude SMGs with $z_{\rm phot}\geqslant 4$ from the fit because at high redshifts the 1.6 μm stellar peak passes through the 8 μm filter making this redshift estimator unreliable. For SMGs with $z<4$ the 1σ dispersion in redshift estimated using Eqn. 1 is $\sigma_z=0.44$ and we find that $\sim 90\%$ of SMGs at $z>2$ have $S_8/S_{3.6}>1$.

4.4 Typical SMG SEDs

To investigate the SED of a typical SMG we show in Fig. 9 the SMG photometry in the rest-frame and normalised in the H-band. We also calculate the expected fluxes expected in each of the 17 photometric filters used throughout this paper as observed at $z=2.2$ and determine the median flux in each.

We begin by noting that the data show evidence for a break at $\sim$ 3500–4000Å suggestive of a Balmer or 4000Å break. Closer inspection hints at it being a Balmer break indicating that the blue rest-frame light is dominated by stars older than 20 Myr and younger than $\sim$ 2 Gyr. Then, as in §3.1, we use HYPERZ to fit this photometry, with redshift fixed at $z=2.2$, and show the best-fit templates for both the Burst and Im star-formation histories on Fig. 9. Comparing the χ^2 for these two models in the same manner as §3.5, we find that we cannot accurately distinguish between different star-formation histories (and hence ages or light-to-mass ratios). The best-fit Burst model has an age of just 33 Myrs, an $A_V=1.7$ and a resulting light-to-mass ratio of $L_H/M^*\sim 24$, in contrast the Im template yields an age of 3.5 Gyrs, $A_V=1.1$ and an $L_H/M^*\sim 6$. The reddening derived from these two template fits are agreement with the median of the individual SED fits ($A_V=1.5\pm0.1$; §3.5), while the L_H/M^* span a range of $4\times$.

We also estimate the extinction in LESS SMGs by comparing the star-formation rate (SFR) derived from the rest-frame far-ultraviolet luminosity (median ${\rm SFR_{UV}}=2\,{\rm M_\odot yr^{-1}}$; Kennicutt 1998) with the SFR derived from the far-infrared luminosity (median ${\rm SFR_{FIR}}=1400\,{\rm M_\odot yr^{-1}}$; §4.6). Comparing the two values yields $A_V=2.6\pm0.2$, corresponding to reddening ~ 4 times higher than the SED fit and indicating that the majority of the star formation within SMGs occurs in totally obscured regions. As discussed in Kennicutt (1998) the conversion from far-ultraviolet luminosity to ${\rm SFR_{UV}}$ assumes that the star-formation rate has been constant for $>10^8$ years. SMGs are likely to be shorter bursts of activity and therefore for a fixed SFR they will brighter at ultraviolet wavelengths and likely have higher A_V than estimated above.

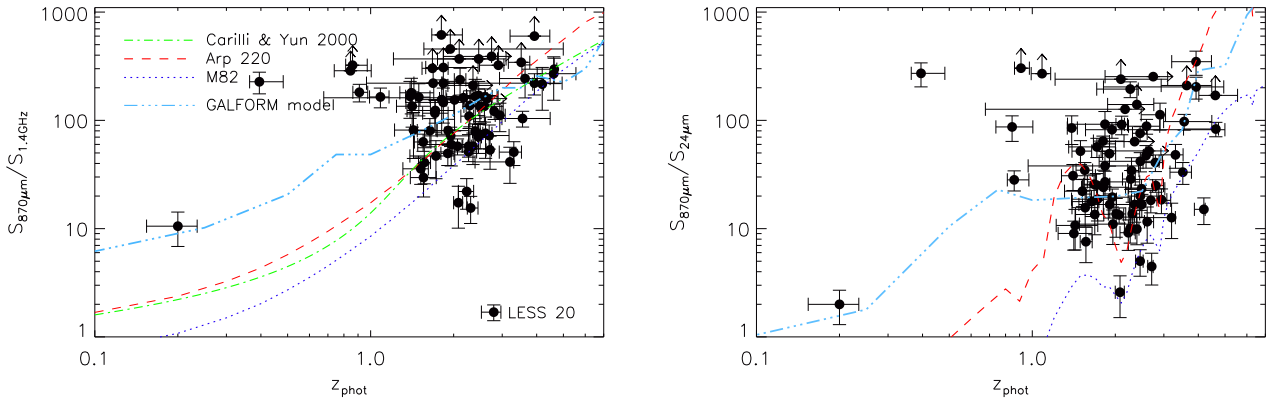

Figure 7. The variation of submillimetre to radio (left) and submillimetre to mid-infrared (right) flux ratios with redshift, compared with Arp 220 and M82 (based on the SEDs of Silva et al. 1998) and SMGs in the ΛCDM GALFORM model (Baugh et al. 2005) with $S_{850\mu m} \geqslant 3$ mJy; we also show the relationship between redshift and radio-to-submillimetre spectral index derived by Carilli & Yun (2000) in the left-hand panel. The SMGs show two orders of magnitude dispersion in both $S_{870\mu m}/S_{1.4GHz}$ and $S_{870\mu m}/S_{24\mu m}$. The model track of $S_{870\mu m}/S_{1.4GHz}$ for M82 lies below the majority of the SMGs, while that of Arp 220 more closely follows the SMGs suggesting that they typically have a characteristic dust temperature which is cooler than that in M82 and more like that in Arp 220. Similarly, although studies have found that mid-infrared spectral properties of SMGs are similar to M82 (Menéndez-Delmestre et al. 2009) we find that M82 does not describe the submillimetre to mid-infrared continuum flux ratios well, and that Arp 220 fits better to this data. LESS 20 (labelled) is significantly brighter at 1.4 GHz than expected from its submillimetre flux and redshift and is most likely a radio-bright AGN.

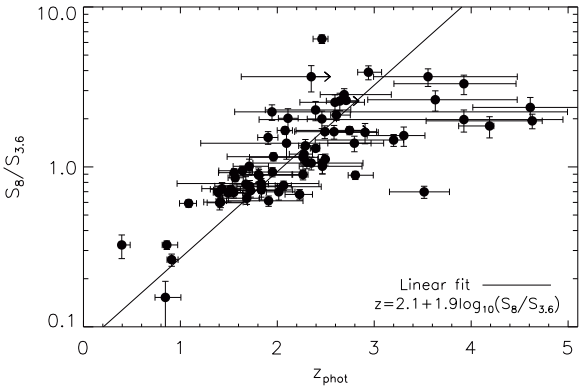

Figure 8. The correlation between redshift and the ratio of 8 μm to 3.6 μm flux for the LESS SMGs. This shows a trend and so we plot a linear fit to the SMGs with $z < 4$, which yields $z = 2.1 + 1.9\log_{10}(S_8/S_{3.6})$, with a 1σ dispersion in redshift of $\sigma_z = 0.44$. This relation may be useful as a crude redshift indicator for SMGs as we note that $\sim 90\%$ of all SMGs with $z > 2$ have $S_8/S_{3.6} > 1$, while similarly $\sim 90\%$ of all SMGs with $z < 2$ have $S_8/S_{3.6} < 1$.

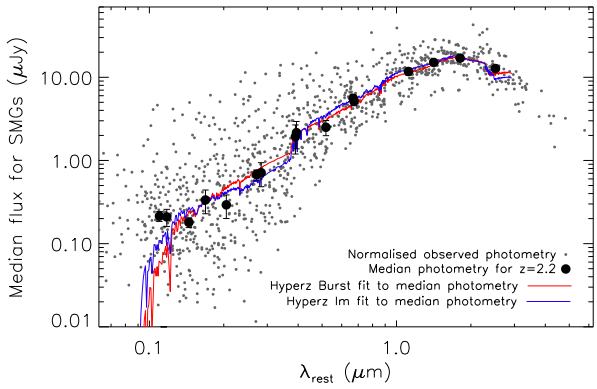

Figure 9. The photometry of SMG counterparts shifted to the rest frame and normalised to the H band (1.6μm). Redshifting this data to $z = 2.2$ we calculate the apparent fluxes in the 17 photometric filters considered throughout this paper and use HYPERZ to fit galaxy templates at this redshift. The median photometric points are shown and the resulting best HYPERZ Burst and Im template fits are displayed. The best fit HYPERZ templates have: Burst, $A_V = 1.7$, an age of 33 Myrs and a $L_H/M^* \sim 24$; Im, $A_V = 1.1$, an age of 3.5 Gyrs and an $L_H/M^* \sim 6$. It is clear that it is not possible to distinguish between these two very different star-formation histories and hence there is a factor of ~ 5 uncertainty in the resulting masses. The MUSYC U38 filter has an $\geqslant 50\%$ contribution from limiting magnitudes and is excluded from the fit.

4.5 Stellar masses

We use HYPERZ to estimate the rest-frame H-band absolute magnitudes (M_H) from our SED fits and find the median $M_H = -24.1 \pm 0.1$, with an interquartile range of -24.7 to -23.6. In Fig. 10 we plot M_H against photometric redshift for the LESS SMG counterparts. There is the suggestion of a weak trend of M_H with redshift. However, as the plotted detection limit shows this is most likely a selection effect, with the higher redshift galaxies needing to be more luminous to be detected. The average $z = 2$–3 SMG has $M_H = -24.4$ and would be detected in our survey out to $z \sim 3$–4, and therefore, any incompleteness in our SMG sample due to the IRAC flux limits is only significant at $z \gtrsim 3$.

M_H is used to estimate the stellar mass of galaxies because it is less influenced by young stars than optical bands and is relatively unaffected by dust. As discussed in §3.5 the uncertainties in the derived spectral types and ages result in an estimated factor of ~ 5 uncertainty in assumed mass-to-light ratios and thus stellar masses derived from M_H. Therefore, we only consider the stellar masses of the LESS SMGs statistically.

Hainline et al. (2010) estimated H-band mass-to-light ratios for SMGs with Burst and Im templates, based on a Chabrier (2003) IMF . We use the average of their values converted to a Salpeter

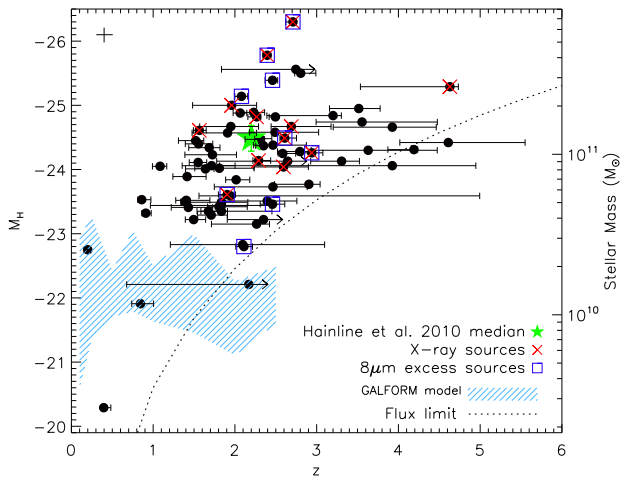

Figure 10. A plot of photometric redshift against rest-frame H-band absolute magnitude for LESS SMGs, and the approximate correspondence with stellar mass (as described in the text). The median M_H is -24.1 ± 0.1 with an interquartile range of -24.7 to -23.6 which corresponds to a median stellar mass of $\sim 9.2 \times 10^{10} M_\odot$ and interquartile range of $(4.7\text{–}14) \times 10^{10} M_\odot$ in good agreement with the median M_H from Hainline et al. (2010). We also highlight SMGs with evidence for AGN activity from X-ray detections or 8 μm excesses, which appear brighter than the average SMG. We also show the 1-σ distribution of absolute H-band magnitudes of SMGs with $S_{850\mu m} \geqslant 3$ mJy that are brighter than our flux limit at 4.5 μm (approximately the rest-frame H-band at $z = 2$) from GALFORM (Baugh et al. 2005; Lacey et al. 2008; Swinbank et al. 2008) and note that M_H is under-predicted in the model. Errors in M_H are dominated by the error in the photometric redshift; we calculate the error in M_H for SMGs with median redshift error by re-running the HYPERZ with the redshift forced to the extremes of the error range; the corresponding errors are shown in the top left-hand corner of the plot and can be scaled with the error in redshift. The dotted line illustrates the trend in M_H with redshift resulting from the flux limited nature of our survey.

IMF (with a lower mass limit of $0.1\,M_\odot$ and an upper mass cutoff of $100\,M_\odot$) for our stellar mass calculation: $L_H/M^* = 3.8\,L_\odot M_\odot^{-1}$. We estimate that the median stellar mass of the SMGs in our sample is $M^* = (9.2 \pm 0.9) \times 10^{10} M_\odot$ and the interquartile range is $(4.7\text{–}14) \times 10^{10} M_\odot$. The quoted errors do not include the systematic uncertainty from the star-formation histories and mass-to-light ratios, which adds a factor of ~ 5 uncertainty to the values (§3.5; Fig. 9). We also caution that the choice of IMF coupled with the assumption that all the light is from the current burst can affect the derived stellar masses by an additional factor of ~ 2. Finally, we note that on average we observe the SMGs approximately halfway through the burst and typical SMG gas masses (Greve et al. 2005) suggest an additional $\sim 3 \times 10^{10} M_\odot$ could be added by the end of the burst.

We find that galaxies with evidence for AGN activity from an 8 μm excess or X-ray emission have median $M_H = -24.6 \pm 0.3$, compared to $M_H = -24.1 \pm 0.1$ for the remainder of the SMGs. The two SMGs with the brightest M_H are the two submillimetre bright quasars (LESS 66 and LESS 96; Appendix A) in which the observed emission is expected to be dominated by the AGN rather than starlight (Hainline et al. 2010). If these are excluded the median M_H of SMGs containing AGN is $M_H = -24.5 \pm 0.3$.

The median stellar mass for SMGs in SHADES Lockman Hole was claimed to be $M^* = (6.3^{+1.6}_{-1.3}) \times 10^{11} M_\odot$ by Dye et al. (2008). This is a factor of ~ 7 higher than our estimate for LESS SMGs. Dye et al. (2008) use nine-band photometry for their photometric redshift determination and claim to also be able to disentangle the star-formation histories of the SMGs with sufficient accuracy to identify a significant mass of old stars which underlies the current burst. This leads to a higher effective mass-to-light ratio and correspondingly higher stellar masses. In contrast, as discussed earlier (§3.5), we do not believe that with existing data it is possible to untangle the influences of the potentially complex star-formation histories and dust distributions on the SEDs of SMGs. Hence, we do not believe that there is any observational evidence for significant old stellar populations in these galaxies, as required by the Dye et al. (2008) results. Hainline et al. (2010) have used optical and IRAC photometric data to calculated an average stellar mass for the Chapman et al. (2005) SMGs and they find $M^* = (1.4 \pm 0.3) \times 10^{11} M_\odot$ (converted to Salpeter IMF), comparable to our survey and a factor of ~ 5 lower than Dye et al. (2008).

In Fig. 10 we also show the absolute H-band magnitudes of SMGs in the ΛCDM GALFORM model (Baugh et al. 2005), which assumes a top-heavy IMF with slope $x = 0$. We consider only galaxies with $S_{850\mu m} \geqslant 3$ mJy and fluxes in the IRAC 4.5 μm filter brighter than our detection limit (4.5 μm corresponds to the rest-frame H-band at $z \sim 2$). Swinbank et al. (2008) showed that GALFORM predicts rest-frame absolute K-band luminosities of SMGs which are a factor of ten lower than observed. This arises primarily due to an order of magnitude lower stellar masses than implied by observations for SMGs (see also Lacey et al. 2010). As Fig. 10 shows the predicted rest-frame H-band magnitudes of the model SMGs are also a factor of ten lower than our observations. Indeed, if SMGs formed stars following the prescriptions used in the Baugh et al. (2005), then few of the SMGs above a redshift of $z \sim 2$ would have be detected.

4.6 Dust temperatures, far-infrared luminosities and star-formation

In order to further investigate the intrinsic properties of the LESS SMGs we next use our photometric redshifts and the observed radio and submillimetre fluxes to derive the characteristic dust temperatures (T_D), far-infrared luminosities (8–1000 μm; L_{FIR}) and star-formation rates.

Blain et al. (2002) showed that the submillimetre-to-radio flux ratio in SMGs is mainly influenced by redshift and the characteristic dust temperature. Chapman et al. (2005) assumed a dust emissivity, $\beta = 1.5$, and the $z = 0$ far-infrared–radio correlation, to determine empirically that for their sample of SMGs:

$$T_D = \frac{6.25(1+z)}{(S_{850\mu\mathrm{m}}/S_{1.4\mathrm{GHz}})^{0.26}} \quad (2)$$

We note that the most reliable method of calculating T_D is to fit template SEDs to multiple far-infrared and submillimetre photometric points, but for simplicity and due to the absence of published deep far-infrared photometry we use Eqn. 2 to calculate T_D of LESS SMGs (although we next use shallow far-infrared observations to confirm the validity of this assumption).

We also use the infrared-radio correlation (Helou et al. 1985; Condon 1992),

$$q_{FIR} = \log_{10}\left(\frac{L_{FIR}}{3.75 \times 10^{12}\mathrm{W}}\right) - \log_{10}\left(\frac{L_{1.4\mathrm{GHz}}}{\mathrm{WHz^{-1}}}\right) \quad (3)$$

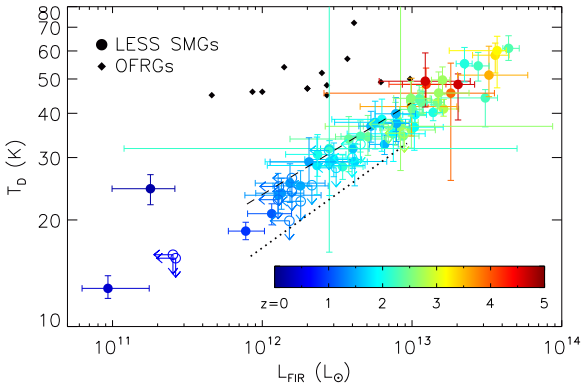

Figure 11. The characteristic dust temperature (T_D) versus far-infrared luminosity (L_{FIR}) for our SMGs. The SMGs are colour coded on the basis of their photometric redshifts and as expected the most luminous galaxies are the hottest, and are also tend to be those at the highest redshifts. This trend is driven in part by the radio luminosities of the SMGs (which lack the positive K correction of the submillimetre waveband) hence why there is a correlation between L_{FIR} and z, but not between $S_{870\mu m}$ and z (Fig. 4). The regions above the dashed line and below the dotted line are illustrative of the regions excluded by our submillimetre and radio detection limits respectively. The dashed line, which roughly demarcates the upper envelope of the data, represents the derived temperature of galaxies at $z = 2$ with various radio fluxes and $S_{870\mu m} = 4.2$ mJy. The dotted line, which similarly demarcates the lower envelope, is derived for submillimetre-luminous ($S_{870\mu m} = 16$ mJy) sources with radio flux equal to our detection limit ($3\sigma = 19.5\mu$Jy) at redshifts of $z = 1.4$–4. This reflects both the strong cut-off in the submillimetre luminosity function at high luminosities and the fact that our radio data is only just deep enough to detect counterparts to the majority of SMGs. We conclude that the apparent correlation between T_D and L_{FIR} is in part caused by selection bias. We note that the OFRGs (Chapman et al. 2004a; Casey et al. 2009; Magnelli et al. 2010), which are detected in the radio but not the submillimetre lie above the upper dashed line.

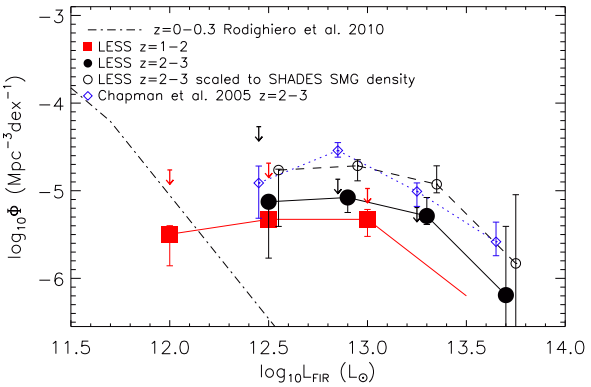

Figure 12. Far-infrared luminosity functions of the radio-detected LESS SMGs with $z = 1$–2 and $z = 2$–3. Evolution is evident in the luminosity function of the LESS SMGs between the two redshift bins, and from the 24-μm selected low redshift comparison sample (Rodighiero et al. 2010). The SMGs have higher luminosities than the $z < 0.3$ 24-μm galaxies, and the $z = 2$–3 SMGs having higher luminosities and Φ^*. We also show the $z = 2$–3 luminosity function of Chapman et al. (2005) SMGs (offset slightly in $\log_{10}L_{FIR}$ for clarity) for comparison. The LESS $z = 2$–3 sample has a systematically lower luminosity density than Chapman et al. (2005) SMGs in the same redshift range. Weiß et al. (2009) showed that the ECDFS is underdense at submillimetre wavelengths and by scaling the LESS luminosity function such that the SMG number density matches that of SHADES survey (Coppin et al. 2006) we show that the disparity in Φ^* between LESS and Chapman et al. (2005) is likely due to the relative density of SMGs in the two surveys (the scaled LESS luminosity function is offset slightly in $\log_{10}L_{FIR}$ SMGs for clarity). We calculate the maximum contribution from unidentified SMGs, by assigning them the redshift distribution that we measure in §4.2 and radio fluxes equal to our detection limit. Including the contribution from unidentified SMGs the total maximum Φ in each luminosity bin is represented by an arrow (offset slightly in $\log_{10}L_{FIR}$ for $z = 2$–3 SMGs for clarity).

with radio spectral index $\alpha = 0.8$ (where $S_\nu \propto \nu^{-\alpha}$) and $q_{FIR} = 2.64$ (Bell 2003, for star-forming galaxies), to calculate far-infrared luminosities of the LESS SMGs from their radio fluxes, as done by Chapman et al. (2005). Although this approach was recently verified by Magnelli et al. (2010) who used *Herschel* data to show that the local far-infrared radio correlation is consistent with SMGs, we caution that there may be a factor of ~ 2 uncertainty in the derived luminosities due to possible evolution in the far-infrared–radio correlation (Ivison et al. 2010a) and hence the appropriate value of q_{FIR}.

In Fig. 11 we plot the far-infrared luminosity against T_D for the LESS SMGs and optically faint radio galaxies (OFRGs; Chapman et al. 2004a; Casey et al. 2009; Magnelli et al. 2010. The LESS SMGs have a median $T_D = 35.9 \pm 1.4$ K, with an interquartile range of 28.5–43.3 K, and $L_{FIR} = (8.2 \pm 1.2) \times 10^{12}\,L_\odot$, with an interquartile range of $(3.0\text{–}13) \times 10^{12} L_\odot$, comparable to previous surveys (e.g. Chapman et al. 2005; Magnelli et al. 2010).

To check this result we also employ the 250, 350, and 500 μm Balloon-borne Large Aperture Submillimeter Telescope (BLAST) maps of the ECDFS (Devlin et al. 2009). We can stack the emission in these maps at the positions of the LESS SMG counterparts and fit the stacked fluxes with a modified black body with $\beta = 1.5$ at $z = 2.2$ and correct the luminosity of the fitted black body to *total* infrared luminosity, 8–1000 μm, based on Ivison et al. (2010c). From this calculation the typical characteristic dust temperature of the LESS SMGs is $T_D = 33.6 \pm 1.1$, and the typical far-infrared luminosity is $L_{FIR} = (7.6^{+1.7}_{-1.5}) \times 10^{12} L_\odot$. These values are in good agreement with those derived above from the local far-infrared–radio correlation.

We find that the highest redshift galaxies also have the highest luminosities due to a combination of the radio K-correction (preventing the detection of low-luminosity galaxies at high redshifts) and luminosity evolution (see Fig. 12). There is an apparent trend between the T_D and L_{FIR} but this is likely at least partially a selection effect, although we note that locally *IRAS* galaxies exhibit a tight correlation between T_D and L_{IR} (Chapman et al. 2003b; Chapin et al. 2009). To illustrate the selection effects we also show in Fig. 11 OFRGs (Chapman et al. 2004a), which are detected at radio but not submillimetre wavelengths and have radio luminosities similar to SMGs, but contain warmer dust ($T_D \sim 45$ K; Casey et al. 2009; Magnelli et al. 2010). Our 870-μm detection limit misses warmer and lower luminosity galaxies from the sample and the radio detection limit excludes the colder luminous galaxies (e.g. Chapman et al. 2005).

In Fig. 12 and Table 3 we present the far-infrared luminosity functions of the radio-detected LESS SMGs with $z = 1$–2 and $z = 2$–3, compared to the $z = 2$–3 result from Chapman et al. (2005). We calculate the LESS SMG luminosity function with an accessible volume technique where:

Table 3. Far-infrared luminosity function for radio-detected LESS SMGs

$z = 1$–2 SMGs		$z = 2$–3 SMGs	
$\log_{10} L_{FIR}$ ($L_\odot$)	$\log_{10}\Phi$ ($\mathrm{Mpc^{-3}dex^{-1}}$)	$\log_{10} L_{FIR}$ ($L_\odot$)	$\log_{10}\Phi$ ($\mathrm{Mpc^{-3}dex^{-1}}$)
12.0	$-5.5^{+0.2}_{-0.3}$	12.5	$-5.1^{+0.1}_{-0.6}$
12.5	-5.3 ± 0.1	12.9	$-5.1^{+0.1}_{-0.2}$
13.0	$-5.3^{+0.1}_{-0.2}$	13.3	$-5.3^{+0.2}_{-0.1}$
13.5	< -6.2	13.7	$-6.2^{+0.7}_{-6.2}$

$$\Phi(L)\Delta L = \sum_i \frac{1}{V_i} \quad (4)$$

which accounts for the flux limited nature of our survey. $\Phi(L)\Delta L$ is the number density of sources with luminosities between L and $L + \Delta L$, and V_i is the comoving volume within which the ith source can be detected in the luminosity bin under consideration. Since we derive the far-infrared luminosity from the radio flux, V_i is calculated using the radio luminosity. Error bars are calculated by bootstrapping and account for the redshift, luminosity and binning errors. We use the same method to calculate the luminosity function for Chapman et al. (2005) SMGs based on the redshifts and radio fluxes listed in that paper. By assuming that unidentified SMGs have radio fluxes equal to our detection limit and the redshift distribution that we measure in §4.2, we also calculate the maximum contribution of unidentified SMGs to the far-infrared luminosity functions.

We observe strong evolution in the far-infrared luminosity function: the $z = 2$–3 SMGs are more luminous and have higher space densities than the $z = 1$–2 SMGs, which in turn are more luminous than the $z < 0.3$ 24 μm-selected galaxies from Rodighiero et al. (2010) (see also the *Herschel* sample of Vaccari et al. 2010). LESS SMGs at $z = 2$–3 have $\Phi^* \sim 60\%$ and $L^* \sim 2\times$ larger than those at $z = 1$–2.

The $z = 2$–3 LESS SMGs have systematically lower Φ^* than the Chapman et al. (2005) SMGs in the same redshift range. This may be due to cosmic variance since Weiß et al. (2009) showed that the ECDFS is a factor of ~ 2 underdense compared to other large submillimetre surveys at flux densities $\gtrsim 3$ mJy. By rescaling the LESS luminosity function so that the 870 μm number counts agree with those of the SHADES survey (Coppin et al. 2006), which should be similar to that of Chapman et al. (2005) since both covered multiple fields, Fig. 12 shows that the low surface density of SMGs in the ECDFS is most likely the cause of the disparity in Φ^*.

In Fig. 13 we show the evolution of the star-formation rate density (SFRD) of the radio-detected LESS SMGs. We use the same accessible volume technique as in our luminosity function calculations to account for the flux limited nature of the survey. Error bars are calculated from bootstrapping and include the uncertainties in binning, redshifts and SFRs. Since the SFRs are based upon radio fluxes we exclude the suspected radio-bright AGN LESS 20 from this analysis.

We do not know the individual redshifts, infrared luminosities or SFRs for 45% of the LESS SMGs because they do not have robustly identified optical counterparts. In Fig. 13 we account for this population by assigning them the redshift distribution that we measure in §4.2) and assuming radio fluxes equal to our detection limit. The calculated SFRD of the unidentified SMGs from this analysis is an upper limit since the actual radio fluxes will typically be lower than the detection limit. In Fig. 13 we indicate the maximum contribution to the SFRD of unidentified SMGs in each redshift bin.

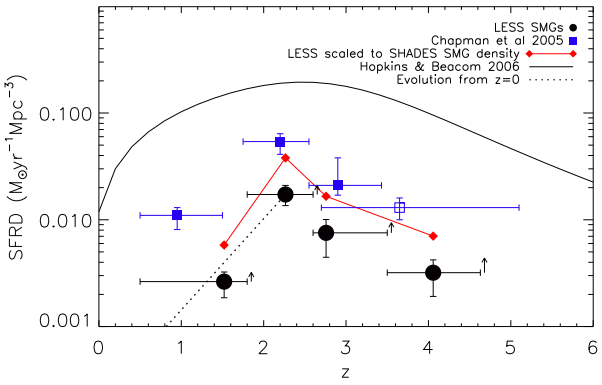

Figure 13. Evolution of the SFRD for the radio-detected LESS SMGs compared to Chapman et al. (2005). Arrows to the right of each LESS redshift bin indicate the maximum additional contribution from unidentified SMGs and the open symbol represents unidentified SMGs from Chapman et al. (2005). We also show the modified Salpeter A IMF fit to the SFRD compilation from Hopkins & Beacom (2006) and a line showing the evolution from *IRAS* ULIRGs at $z = 0$ (Elbaz & Cesarsky 2003) to LESS SMGs at $z = 2.3$. The LESS SMG activity peaks at $z \sim 2$ – similar to that found by previous studies of star-forming galaxies and the peak activity of quasars (Hopkins et al. 2007). The contribution from SMGs to the total SFRD also peaks at $z \sim 2$ where they are responsible for $\sim 10\%$ of the Hopkins & Beacom (2006) SFRD. The ECDFS is underdense at submillimetre wavelengths (Weiß et al. 2009) so similarly to Fig. 12 we also scale the SFRD of the LESS SMGs such that the number counts match the SHADES survey allowing a closer comparison to Chapman et al. (2005).

The SFRD of the LESS SMGs appears to peak at $z \sim 2$, similar to Chapman et al. (2005). The LESS SMGs have a lower SFRD than the SMGs from Chapman et al. (2005) but we note that the lower number density of SMGs in the ECDFS is sufficient to account for this effect. This corresponds to the peak of quasar activity at $z = 2.15 \pm 0.05$ (Hopkins et al. 2007). The fractional contribution of LESS SMGs to the SFRD of the Universe also peaks at $z \sim 2$ where they are responsible for $\sim 10\%$ of the SFRD as estimated by Hopkins & Beacom (2006) from a compilation of surveys that does not include any submillimetre surveys. We stress that this only includes SMGs with $S_{870\mu m} \gtrsim 4$ mJy. Assuming that fainter sources have the same redshift distribution then the contribution of SMGs with $S_{870\mu m} \gtrsim 1$ mJy is $\sim 100\%$ of the (Hopkins et al. 2007) value. Thus, SMGs contribute $\sim 50\%$ of the *total* SFRD of the Universe at $z \sim 2$.

We use Kennicutt (1998), which assumes a Salpeter IMF with upper and lower mass limits of 0.1 and 100 $M_\odot$ respectively, to calculate the SFRs of the LESS SMGs from their inferred far-infrared luminosities. The median SFR is 1100 ± 200 $\mathrm{M_\odot yr^{-1}}$ and the interquartile range is 300–1900 $\mathrm{M_\odot yr^{-1}}$. The median specific star-formation rate $\mathrm{sSFR} = \mathrm{SFR}/M^* = (1.2 \pm 0.1) \times 10^{-8}\mathrm{yr^{-1}}$ and the interquartile range is $(0.6\text{–}1.8)\times 10^{-8}\mathrm{yr^{-1}}$. Although again, we caution that due to the uncertainties in the stellar mass estimates there is an additional factor of ~ 5 uncertainty in these values (see §3.5 for a full discussion). The median formation timescale of the LESS SMGs is thus ~ 100 Myr and it is feasible that all of the stellar mass we see could be formed in a single burst. In Fig. 14 we plot the trend of sSFR against the redshift of the LESS SMGs. We note that the apparent lack of galaxies with low sSFR at high redshifts is a selection effect due to the requirement for a radio counterpart and that galaxies with $\mathrm{sSFR} \gtrsim 10^{-7}\mathrm{yr^{-1}}$ are rare due the brevity of the

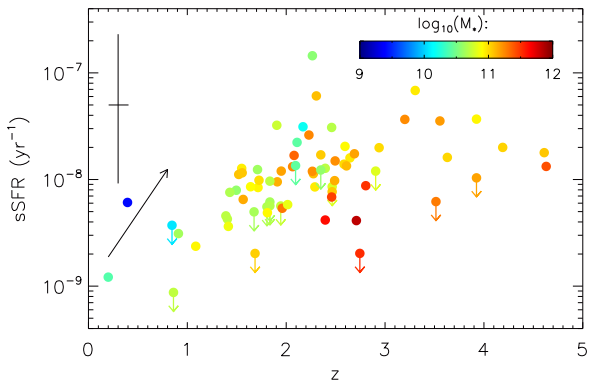

Figure 14. A plot of specific star-formation rate (sSFR) versus redshift for the LESS SMGs. Galaxies are colour-coded by mass and we show the median error bar in the top-left hand corner and note that similarly to Fig. 10 the error in sSFR is correlated with that in redshift. The arrow represents the gradient of the trend in sSFR with redshift for IRAC-selected galaxies with $\log_{10}(M_*) = 10.3$–$10.8\,M_{\odot}$, offset in sSFR by two orders of magnitude for the purpose of display. We note that due to the requirement for radio counterparts no SMGs are detected in the high redshift and low sSFR region of this plot. Similarly, the short lifetime of SMGs with sSFR $\gtrsim 10^{-7}\mathrm{yr}^{-1}$ and the limited volume of our survey means that few SMGs with very high sSFRs are detected. However, the dearth of SMGs at $z \lesssim 1.5$ with sSFR $\gtrsim 10^{-8}\mathrm{yr}^{-1}$ may indicate an upper-limit to the sSFR of SMGs with a similar scaling to the trends seen in lower activity galaxies at lower redshifts (Damen et al. 2009).

burst phase. However, the dearth of SMGs at $z \lesssim 1.5$ with sSFR $\sim 10^{-8}$–$10^{-7}\,\mathrm{yr}^{-1}$ is not a selection effect and this upper envelope may be following the same trend in sSFR with redshift seen in galaxies with similar masses but lower SFRs (e.g Damen et al. 2009).

Finally, we relate our new estimate of the redshift distribution of SMGs to constraints on the evolution of their likely descendants: massive early-type galaxies (Swinbank et al. 2006). As we have shown, the bulk of the SMG population with observed 870-μm fluxes above ~ 4 mJy lie at redshifts of $z \sim 1.5$–3 with a median redshift of $z \sim 2.5$. We estimate that the volume density of SMGs at $z = 2$–3 above our flux is $1.2 \times 10^{-5}\,\mathrm{Mpc}^{-3}$, where we include both the identified and statistically identified samples in this estimate. Using a characteristic lifetime of the SMG phase of ~ 100 Myr, we can correct this density for the burst duty cycle to derive a volume density for the remnants of $2 \times 10^{-4}\,\mathrm{Mpc}^{-3}$. As we have shown, the estimated baryonic masses of these galaxies are $\sim 1.2 \times 10^{11}\,\mathrm{M}_{\odot}$ combining our best estimate of the stellar mass with the typical gas masses from Greve et al. (2005). If the burst of star formation we are seeing in the SMG phase is the last major star formation event in these galaxies then we expect their descendants to appear as passive, red galaxies at $z \sim 1.5$ (> 1 Gyr after $z \sim 2$).

There have been various estimates of the volume density of massive, passive galaxies at $z \sim 1$–2 (McCarthy et al. 2004; Daddi et al. 2005; Taylor et al. 2009a). For galaxies with masses of $\gtrsim 10^{11}\,\mathrm{M}_{\odot}$, the estimated space densities are 1–$2 \times 10^{-4}\,\mathrm{Mpc}^{-3}$ (at $z = 1.5$–1.8; Taylor et al. 2009a), $3 \times 10^{-4}\,\mathrm{Mpc}^{-3}$ (at $<z>= 1.7$; Daddi et al. 2005) and $0.6 \times 10^{-4}\,\mathrm{Mpc}^{-3}$ (at $<z>= 1.5$; McCarthy et al. 2004). These estimates, with their various uncertainties, are comparable to the predicted volume density of massive, passive galaxies if these all undergo an SMG-phase at an earlier epoch. Hence, the starbursts in SMGs may be responsible for the formation of a large fraction of the passive, massive galaxies seen at $z \sim 1.5$.

We can attempt a similar calculation comparing the SMG population at $z > 3$ with the constraints on massive galaxies at $z \gtrsim 2$. We estimate the volume density of $z > 3$ SMGs from §4.2 as $2.8 \times 10^{-6}\,\mathrm{Mpc}^{-3}$. This includes the 10 identified SMGs, 4 ± 2 statistically identified SMGs and the remaining 21 ± 19 unidentified sources and assumes that they are contained within a redshift range of $z = 3$–7. Using a characteristic lifetime of the SMG phase of ~ 100 Myr, we can correct this density for the burst duty cycle to derive a volume density for the remnants of $3.8 \times 10^{-5}\,\mathrm{Mpc}^{-3}$. Again the estimated baryonic masses of these galaxies are $\sim 1.2 \times 10^{11}\,\mathrm{M}_{\odot}$. Unfortunately observable limits on the volume density of passive galaxies are increasingly uncertain at $z > 2$, but using the estimates from Coppin et al. (2009) of the volume density of massive galaxies of ~ 1–$5 \times 10^{-5}\,\mathrm{Mpc}^{-3}$, we again conclude that it is possible that the SMG population we have identified is also responsible for the formation of a significant of the most massive galaxies at $z \sim 2.5$.

Thus we conclude that the presence of a sizable population of passive galaxies at high redshift may be intimately linked to the strong evolution in dust obscured starbursts in the distant Universe. Theoretical attempts to match the properties of high-redshift galaxies therefore need to focus on these observable constraints as aspects of the same problem (Swinbank et al. 2008).

5 SUMMARY AND CONCLUSIONS

We use deep multicolour imaging of the ECDFS in 17-bands to derive the photometric properties of the counterparts of SMGs in the LESS LABOCA survey of the ECDFS (Weiß et al. 2009; Biggs et al. 2010). Our main results are as follows:

(i) LESS radio, 24 μm and IRAC-identified SMGs have a median redshift of $z = 2.2 \pm 0.1$ and interquartile range of $z = 1.8$–2.7. Thus the peak activity in SMGs corresponds to the epoch of maximal quasar and star-formation activity in the Universe. The redshift distribution of LESS SMGs is consistent with the spectroscopic survey of Chapman et al. (2005), but higher than the photometric studies of the SHADES survey (Clements et al. 2008; Dye et al. 2008). We find a higher-redshift tail to the distribution of LESS galaxies, with 10 (14%) identified SMGs at $z \gtrsim 3$. Counterparts identified through radio, 24 μm and IRAC emission have statistically indistinguishable redshift distributions; similarly robust and tentative counterparts have comparable redshift distributions, albeit with some foreground contamination in the tentative sample. Previous studies provided tentative evidence that SMGs with the highest submillimetre fluxes may be the highest redshift sources (e.g. Ivison et al. 2002; Pope et al. 2005), but with our extensive photometric redshifts we find no such correlation.

(ii) A statistical study of the source population in the error circles of the 55 SMGs that lack robust radio, 24 μm and IRAC counterparts suggests that there is an excess of 26 ± 12 (2.2σ) $z > 1$ galaxies in these regions. Of these 14 ± 8 (1.8σ) are at $z = 2$–3 and 4 ± 2 (1.6σ) are at $z = 4$–5. This excess population corresponds to the counterparts or companions of the unidentified SMGs and our analysis then suggests that the redshift distribution of these unidentified SMGs peaks at $z = 2.5 \pm 0.3$. This is similar to, but slightly higher than, that of the identified population, suggesting that many of the unidentified SMGs are at $z \sim 2$–3 and have radio or 24μm fluxes just below our detection limits.

(iii) We estimate that there are 21 ± 19 ($17 \pm 15\%$ of all the SMGs) LESS SMGs that are not robustly identified, and which are not accounted for in our statistical analysis of unidentified SMGs. These should be galaxies without any detectable mid-infrared emission and as a result are likely to lie at $z \gtrsim 3$. Including the identified SMGs at $z > 3$ we estimate that $28 \pm 15\%$ of all LESS SMGs lie at $z > 3$.

(iv) We combine the redshift distribution of identified SMGs with that statistically determined for unidentified SMGs, including the SMGs which are not detected in our survey and are likely to lie at $z \gtrsim 3$. We conclude that the likely median redshift of the *entire* population of $S_{870\mu m} \gtrsim 4$ mJy SMGs is $z = 2.5 \pm 0.6$.

(v) The separation of SMGs into those with redshifts above and below $z = 1.4$ broadly agrees with the BzK colour-colour criteria (Daddi et al. 2004), making the BzK colours a coarse but reliable redshift indicator for SMGs. Similarly the submillimetre-to-radio flux ratios of LESS SMGs broadly agrees with the prediction of Carilli & Yun (2000), although there is significant scatter, indicative of temperature variations between SMGs. This means that redshifts derived from submillimetre-to-radio flux ratios also exhibit significant scatter. Instead, we show that the IRAC colours of the $\sim 90\%$ of SMGs with $z < 4$ follow a trend with redshift of: $z = 2.1 + 1.9\log_{10}(S_8/S_{3.6})$ and this may be a potentially useful redshift indicator with a 1-σ accuracy of $\sigma_z = 0.4$.

(vi) The median rest-frame H-band absolute magnitude of the LESS SMGs is $M_H = -24.1 \pm 0.1$ with an interquartile range of -24.7 to -23.6. Using M_H and the average mass-to-light ratio from Hainline et al. (2010) (converted to a Salpeter IMF) we calculate that the median stellar mass of the LESS SMGs is $(9.2 \pm 0.9) \times 10^{10} M_{\odot}$, with an interquartile range of $(4.7\text{–}14) \times 10^{10} M_{\odot}$. However, a χ^2 analysis of the best-fit star-formation histories shows that, even with 17-band photometry spanning the ultraviolet to mid-infrared, we cannot reliably distinguish different star-formation histories and ages for the SMGs. We estimate that this results in an additional factor of ~ 5 uncertainty in the mass-to-light ratios and hence the derived stellar masses.

(vii) Using our photometric redshifts, submillimetre and radio fluxes we calculate that the median characteristic dust temperature of the SMGs is $T_D = 35.9 \pm 1.4$ K, with an interquartile range of 28.5–43.3 K. The median far-infrared luminosity of the SMGs, derived from the radio luminosity, is $L_{FIR} = (8.2 \pm 1.2) \times 10^{12} L_{\odot}$ and the interquartile range of $L_{FIR} = (3\text{–}13) \times 10^{12} L_{\odot}$. For a Salpeter IMF this corresponds to median SFR $= 1100\,\mathrm{M_{\odot} yr^{-1}}$, with an interquartile range of 300–1900 $\mathrm{M_{\odot} yr^{-1}}$. We show that, for LESS SMGs, the apparent correlation between the far-infrared luminosity and T_D is in part a selection effect.

(viii) The far-infrared luminosity function of the LESS SMGs exhibits a strong redshift evolution, such that SMGs at $z = 2\text{–}3$ are more numerous and have higher luminosities than those at $z = 1\text{–}2$. We find that the normalisation of the luminosity function is lower for LESS than for the Chapman et al. (2005) SMG sample, and by scaling the ECDFS submillimetre number counts we show that this is due to the underdensity of the ECDFS at submillimetre wavelengths (Weiß et al. 2009).

(ix) The SFRD and fractional contribution to the global SFRD of the LESS SMGs with $S_{870\mu m} \gtrsim 4$ mJy evolves with redshift and both peak at $z \sim 2$, where the LESS population contributes a total SFR density of $0.02\,M_{\odot}\mathrm{yr^{-1}Mpc^{-1}}$. If fainter submillimetre sources have the same redshift distribution then SMGs with $S_{870\mu m} > 1$ mJy produce $\sim 50\%$ of the SFRD of the Universe at $z \sim 2$.

(x) The masses and the volume density of LESS SMGs at $z = 2\text{–}3$ are comparable to those of massive, passive galaxies at $z \sim 1\text{–}2$, and similarly the volume density of $z > 3$ SMGs is comparable to the limits on the numbers of massive galaxies at $z \sim 2\text{–}3$. This suggests that a large fraction of the population of massive, passive galaxies at high-redshifts form most of their stars during an earlier SMG phase.

This analysis demonstrates the strengths and weaknesses of photometric redshift analysis for SMGs in a field with excellent photometry. In the impending era of SCUBA-2 and *Herschel* $\gg 10^5$ SMGs will be discovered; it will be impossible to obtain spectroscopic redshifts for such large samples and hence the challenge is to obtain sufficient photometric coverage of these survey fields to allow a photometric analysis of the type described here.

ACKNOWLEDGEMENTS

We thank Carlton Baugh, Mark Dickinson and Laura Hainline for help and useful discussions. J.L.W acknowledges the support of a Science and Technology Facilities Council (STFC) studentship; K.E.K.C acknowledges the support of an STFC fellowship; I.R.S acknowledges the support of STFC. W.N.B, B.L and Y.Q.X acknowledge Chandra X-ray Observatory grant SP8-9003A and NASA ADP grant NNX10AC99G. J.S.D acknowledges the support of the Royal Society through a Wolfson Research Merit award, and the support of the European Research Council through the award of an Advanced Grant. This publication is based on data acquired with the Atacama Pathfinder Experiment (APEX) under programme numbers 078.F-9028(A), 079.F-9500(A), 080.A-3023(A), and 081.F-9500(A). APEX is a collaboration between the Max-Planck-Institut fur Radioastronomie, the European Southern Observatory, and the Onsala Space Observatory. Based on observations made with ESO Telescopes at the Paranal and La Silla Observatories under programme numbers 171.A-3045, 168.A-0485, 082.A-0890 and 183.A-0666.

Table 4. Observed photometry for robust counterparts to LESS SMGs. 3σ limiting magnitudes are presented where sources are covered by imaging but not detected; SMGs which are not covered by imaging in a given filter have no photometry listed in that filter.

Source	MUSYC U	$U38$	VIMOS U	B	V	R	I	z	MUSYC J	HAWKI J	H	MUSYC K	HAWKI K	3.6μm	4.5μm	5.8μm	8μm
LESS 2a	25.67 ± 0.13	25.35 ± 0.32	25.19 ± 0.10	24.78 ± 0.05	24.65 ± 0.05	24.39 ± 0.09	24.08 ± 0.15	23.82 ± 0.17	22.81 ± 0.16	22.88 ± 0.04	> 23.02	21.65 ± 0.13	22.18 ± 0.03	21.37 ± 0.07	21.18 ± 0.07	21.13 ± 0.14	21.49 ± 0.09
LESS 2b	> 26.85	> 25.40	> 28.38	> 26.81	26.56 ± 0.29	> 25.79	> 24.94	> 24.48	> 23.64	24.44 ± 0.09	22.94 ± 0.29	> 22.72	23.26 ± 0.05	22.38 ± 0.11	22.08 ± 0.10	21.86 ± 0.20	22.23 ± 0.14
LESS 3	> 26.85	> 25.40	...	> 26.81	> 26.68	> 25.79	> 24.94	> 24.48	> 23.64	...	> 23.02	> 22.72	23.30 ± 0.05	22.72 ± 0.12	22.09 ± 0.10	21.74 ± 0.19	21.42 ± 0.09
LESS 6	26.57 ± 0.27	> 25.40	28.11 ± 0.23	25.95 ± 0.15	24.94 ± 0.07	24.00 ± 0.06	22.91 ± 0.05	22.75 ± 0.07	21.83 ± 0.07	22.09 ± 0.03	21.73 ± 0.10	21.10 ± 0.08	21.15 ± 0.02	21.14 ± 0.06	21.52 ± 0.08	21.92 ± 0.21	22.36 ± 0.17
LESS 7	26.46 ± 0.25	> 25.40	26.29 ± 0.12	24.90 ± 0.06	24.08 ± 0.03	23.37 ± 0.04	22.22 ± 0.03	22.11 ± 0.04	21.69 ± 0.06	21.44 ± 0.02	21.07 ± 0.06	20.47 ± 0.04	20.46 ± 0.01	20.02 ± 0.04	19.91 ± 0.04	19.86 ± 0.08	20.15 ± 0.05
LESS 9	> 26.85	...	> 28.38	> 26.81	> 26.68	> 25.79	> 24.94	...	> 23.64	24.19 ± 0.08	> 23.02	> 22.72	22.47 ± 0.04	21.85 ± 0.08	21.43 ± 0.08	21.29 ± 0.15	21.13 ± 0.08
LESS 10a	26.29 ± 0.21	> 25.40	25.74 ± 0.11	25.53 ± 0.11	25.60 ± 0.13	25.05 ± 0.16	24.61 ± 0.23	> 24.48	> 23.64	24.56 ± 0.10	> 23.02	> 22.72	23.33 ± 0.05	22.21 ± 0.10	21.78 ± 0.09	21.72 ± 0.19	21.46 ± 0.09
LESS 10b	> 26.85	> 25.40	27.45 ± 0.14	26.66 ± 0.28	25.79 ± 0.15	24.28 ± 0.08	22.63 ± 0.04	22.36 ± 0.05	21.41 ± 0.05	21.18 ± 0.02	20.81 ± 0.05	20.51 ± 0.05	20.29 ± 0.01	19.87 ± 0.03	20.14 ± 0.04	20.75 ± 0.12	21.32 ± 0.09
LESS 11	> 26.85	...	27.86 ± 0.15	> 26.81	> 26.68	> 25.79	> 24.94	> 24.48	> 23.64	25.04 ± 0.12	> 23.02	> 22.72	23.58 ± 0.06	22.16 ± 0.10	21.63 ± 0.09	21.29 ± 0.15	21.15 ± 0.08
LESS 12	> 26.85	> 25.40	> 28.38	> 26.81	> 26.68	> 25.79	> 24.94	> 24.48	> 23.64	25.71 ± 0.18	> 23.02	> 22.72	23.83 ± 0.06	22.72 ± 0.12	22.35 ± 0.12	22.17 ± 0.23	21.98 ± 0.12
LESS 14	> 26.85	> 25.40	> 28.38	> 26.81	26.71 ± 0.32	> 25.79	> 24.94	> 24.48	> 23.64	25.56 ± 0.19	...	> 22.72	23.53 ± 0.06	22.55 ± 0.11	21.87 ± 0.09	21.56 ± 0.17	21.14 ± 0.08
LESS 15	> 26.85	...	...	> 26.81	> 26.68	> 25.79	> 24.94	> 24.48	> 23.64	...	...	> 22.72	...	21.91 ± 0.09	21.30 ± 0.07	21.11 ± 0.14	21.05 ± 0.08
LESS 16	25.04 ± 0.07	24.86 ± 0.21	24.83 ± 0.10	24.49 ± 0.04	24.01 ± 0.03	23.29 ± 0.03	21.79 ± 0.02	21.57 ± 0.02	20.95 ± 0.03	20.93 ± 0.02	20.44 ± 0.05	20.16 ± 0.03	20.15 ± 0.01	19.51 ± 0.03	19.71 ± 0.04	20.03 ± 0.08	20.08 ± 0.05
LESS 17	25.15 ± 0.08	25.25 ± 0.29	24.83 ± 0.10	24.47 ± 0.04	24.26 ± 0.04	23.94 ± 0.06	23.27 ± 0.07	23.05 ± 0.09	22.05 ± 0.08	22.16 ± 0.03	21.64 ± 0.10	21.25 ± 0.09	21.07 ± 0.02	20.36 ± 0.04	20.16 ± 0.04	20.38 ± 0.10	20.76 ± 0.07
LESS 18	26.11 ± 0.18	> 25.40	25.71 ± 0.11	25.52 ± 0.11	25.34 ± 0.10	25.30 ± 0.20	24.64 ± 0.23	24.41 ± 0.27	23.21 ± 0.22	22.81 ± 0.04	22.05 ± 0.14	21.35 ± 0.10	21.45 ± 0.02	20.38 ± 0.04	20.06 ± 0.04	20.01 ± 0.08	20.67 ± 0.06
LESS 19	> 26.85	> 25.40	27.01 ± 0.12	27.04 ± 0.35	26.39 ± 0.25	26.79 ± 0.62	> 24.94	> 24.48	> 23.64	23.82 ± 0.07	...	> 22.72	24.22 ± 0.08	22.74 ± 0.12	22.23 ± 0.11	21.83 ± 0.19	21.98 ± 0.12
LESS 20	> 26.85	> 25.40	...	26.25 ± 0.20	25.66 ± 0.13	25.89 ± 0.33	> 24.94	> 24.48	> 23.64	24.56 ± 0.09	> 23.02	> 22.72	22.57 ± 0.03	21.83 ± 0.08	21.48 ± 0.08	21.16 ± 0.14	21.46 ± 0.09
LESS 22	> 26.85	...	...	> 26.81	26.20 ± 0.21	25.60 ± 0.26	> 24.94	> 24.48	...	...	...	...	...	20.47 ± 0.04	20.16 ± 0.04	20.04 ± 0.08	20.55 ± 0.06
LESS 24	> 26.85	> 25.40	...	25.53 ± 0.11	25.71 ± 0.14	25.15 ± 0.18	24.31 ± 0.18	24.71 ± 0.35	22.71 ± 0.14	...	...	21.39 ± 0.10	...	20.67 ± 0.05	20.41 ± 0.05	20.73 ± 0.12	20.97 ± 0.08
LESS 25	...	> 25.40	26.78 ± 0.13	26.02 ± 0.16	25.46 ± 0.11	25.04 ± 0.16	24.45 ± 0.20	24.25 ± 0.24	> 23.64	23.23 ± 0.05	...	21.82 ± 0.15	21.67 ± 0.02	21.03 ± 0.06	20.73 ± 0.05	20.58 ± 0.11	20.83 ± 0.07
LESS 27a	> 26.85	> 25.40	...	> 26.81	> 26.68	> 25.79	> 24.94	> 24.48	> 23.64	> 25.70	> 23.02	> 22.72	...	22.68 ± 0.12	22.30 ± 0.12	21.93 ± 0.22	22.31 ± 0.17
LESS 27b	> 26.85	> 25.40	...	26.14 ± 0.18	25.88 ± 0.16	25.35 ± 0.21	> 24.94	> 24.48	> 23.64	...	...	> 22.72	...	22.01 ± 0.09	21.68 ± 0.09	21.45 ± 0.16	21.95 ± 0.12
LESS 29	> 26.85	...	...	> 26.81	> 26.68	> 25.79	> 24.94	> 24.48	> 23.64	...	...	> 22.72	...	22.22 ± 0.10	21.70 ± 0.09	21.27 ± 0.15	21.19 ± 0.09
LESS 31	> 26.85	> 25.40	...	> 26.81	> 26.68	> 25.79	> 24.94	> 24.48	> 23.64	26.49 ± 0.26	...	> 22.72	23.46 ± 0.05	22.70 ± 0.12	22.19 ± 0.11	21.68 ± 0.18	21.65 ± 0.10
LESS 34	24.98 ± 0.07	24.69 ± 0.18	24.39 ± 0.10	24.09 ± 0.03	23.67 ± 0.02	23.06 ± 0.03	21.87 ± 0.02	21.57 ± 0.02	20.94 ± 0.03	20.78 ± 0.02	20.29 ± 0.05	20.04 ± 0.03	19.90 ± 0.01	19.51 ± 0.03	19.71 ± 0.04	20.37 ± 0.10	20.73 ± 0.06
LESS 36	> 26.85	> 25.40	...	> 26.81	...	> 25.79	> 24.94	> 24.48	> 23.64	25.70 ± 0.16	...	22.67 ± 0.30	22.76 ± 0.04	21.53 ± 0.07	21.06 ± 0.06	20.65 ± 0.11	20.98 ± 0.07
LESS 37	> 26.85	...	...	26.19 ± 0.19	25.33 ± 0.10	24.18 ± 0.08	23.45 ± 0.08	...	22.86 ± 0.16	...	22.38 ± 0.18	21.16 ± 0.08	...	20.55 ± 0.05	20.41 ± 0.05	20.82 ± 0.13	20.94 ± 0.08
LESS 39	25.44 ± 0.10	> 25.40	...	25.17 ± 0.08	24.77 ± 0.06	24.15 ± 0.07	23.91 ± 0.13	23.41 ± 0.12	23.59 ± 0.30	24.32 ± 0.10	...	22.01 ± 0.17	...	21.62 ± 0.07	21.28 ± 0.07	21.06 ± 0.14	21.07 ± 0.08
LESS 40	24.82 ± 0.06	24.71 ± 0.19	24.54 ± 0.10	24.36 ± 0.04	24.07 ± 0.03	23.81 ± 0.05	23.36 ± 0.08	23.44 ± 0.12	23.04 ± 0.19	23.05 ± 0.05	22.52 ± 0.21	22.20 ± 0.20	22.09 ± 0.03	21.45 ± 0.07	21.12 ± 0.07	21.04 ± 0.13	20.99 ± 0.07
LESS 41	...	...	...	...	...	...	...	...	...	...	...	...	...	20.50 ± 0.04	20.19 ± 0.04	19.91 ± 0.08	19.93 ± 0.05
LESS 43	> 26.85	> 25.40	28.17 ± 0.21	> 26.81	> 26.68	> 25.79	> 24.94	> 24.48	> 23.64	23.93 ± 0.07	23.11 ± 0.33	> 22.72	22.58 ± 0.03	21.46 ± 0.07	21.04 ± 0.06	21.09 ± 0.14	21.73 ± 0.11
LESS 44	25.06 ± 0.07	24.77 ± 0.20	...	24.42 ± 0.04	24.32 ± 0.04	24.34 ± 0.09	24.58 ± 0.22	24.32 ± 0.25	...	...	...	...	...	20.94 ± 0.05	20.59 ± 0.05	20.37 ± 0.10	20.82 ± 0.07
LESS 47	> 26.85	> 25.40	27.05 ± 0.13	26.31 ± 0.21	25.58 ± 0.12	25.26 ± 0.19	> 24.94	> 24.48	> 23.64	...	...	> 22.72	...	22.37 ± 0.10	22.00 ± 0.10	21.80 ± 0.19	21.83 ± 0.12
LESS 48	...	...	> 28.38	...	...	...	...	...	...	...	...	...	...	20.27 ± 0.04	20.15 ± 0.04	20.14 ± 0.09	20.80 ± 0.07
LESS 49a	26.26 ± 0.21	> 25.40	...	25.30 ± 0.09	25.22 ± 0.09	24.59 ± 0.11	24.07 ± 0.14	24.25 ± 0.24	...	23.85 ± 0.07	...	...	22.20 ± 0.03	21.26 ± 0.06	20.97 ± 0.06	21.41 ± 0.16	21.67 ± 0.11
LESS 49b	> 26.85	> 25.40	...	24.85 ± 0.06	24.56 ± 0.05	24.37 ± 0.09	24.13 ± 0.15	24.38 ± 0.26	...	23.85 ± 0.07	...	...	22.49 ± 0.03	22.16 ± 0.10	21.88 ± 0.09	21.65 ± 0.18	21.67 ± 0.11
LESS 50a	24.34 ± 0.04	24.09 ± 0.11	23.95 ± 0.10	23.70 ± 0.02	23.38 ± 0.02	22.90 ± 0.02	22.19 ± 0.03	22.04 ± 0.03	21.75 ± 0.06	21.62 ± 0.02	21.55 ± 0.09	21.32 ± 0.09	21.17 ± 0.02	21.20 ± 0.06	21.67 ± 0.09	22.17 ± 0.25	23.24 ± 0.32
LESS 50b	> 26.85	...	26.12 ± 0.12	26.17 ± 0.18	26.12 ± 0.20	25.90 ± 0.33	> 24.94	> 24.48	> 23.64	24.22 ± 0.08	> 23.02	22.63 ± 0.29	22.65 ± 0.03	21.70 ± 0.08	21.17 ± 0.07	20.76 ± 0.12	20.57 ± 0.06
LESS 54	> 26.85	...	26.97 ± 0.13	26.08 ± 0.17	26.33 ± 0.24	> 25.79	> 24.94	> 24.48	> 23.64	...	...	> 22.72	...	21.66 ± 0.08	21.26 ± 0.07	21.31 ± 0.15	21.97 ± 0.12
LESS 56	> 26.85	> 25.40	> 28.38	> 26.81	> 26.68	> 25.79	> 24.94	> 24.48	23.77 ± 0.35	24.46 ± 0.09	22.57 ± 0.22	22.15 ± 0.20	22.00 ± 0.03	21.27 ± 0.06	20.95 ± 0.06	20.81 ± 0.12	21.24 ± 0.09
LESS 57	> 26.85	> 25.40	26.57 ± 0.12	25.14 ± 0.08	25.38 ± 0.10	24.96 ± 0.15	> 24.94	> 24.48	> 23.64	24.25 ± 0.08	23.05 ± 0.32	> 22.72	22.55 ± 0.03	22.02 ± 0.09	21.63 ± 0.08	21.35 ± 0.16	20.3 ± 0.06
LESS 59	> 26.85	> 25.40	27.66 ± 0.14	26.89 ± 0.33	26.67 ± 0.31	> 25.79	24.36 ± 0.19	> 24.48	23.14 ± 0.21	23.03 ± 0.04	22.53 ± 0.21	21.62 ± 0.12	21.71 ± 0.02	20.71 ± 0.05	20.51 ± 0.05	20.83 ± 0.12	21.2 ± 0.09
LESS 60	25.50 ± 0.11	25.12 ± 0.26	24.98 ± 0.10	24.95 ± 0.06	24.59 ± 0.05	24.08 ± 0.07	23.18 ± 0.07	22.87 ± 0.07	22.54 ± 0.12	22.23 ± 0.03	22.01 ± 0.13	21.49 ± 0.11	21.31 ± 0.02	20.59 ± 0.05	20.39 ± 0.05	20.54 ± 0.11	20.6 ± 0.06
LESS 62	26.55 ± 0.26	> 25.40	26.27 ± 0.12	25.55 ± 0.11	25.09 ± 0.08	24.44 ± 0.10	23.45 ± 0.08	23.56 ± 0.13	22.17 ± 0.09	22.11 ± 0.03	21.50 ± 0.09	20.81 ± 0.06	20.85 ± 0.01	19.93 ± 0.03	19.75 ± 0.04	20.08 ± 0.09	20.2 ± 0.05
LESS 63	25.39 ± 0.10	> 25.40	...	25.05 ± 0.07	24.69 ± 0.06	24.25 ± 0.08	23.28 ± 0.07	22.92 ± 0.08	22.02 ± 0.08	21.83 ± 0.03	21.80 ± 0.11	21.21 ± 0.09	21.12 ± 0.02	20.69 ± 0.05	20.53 ± 0.05	20.76 ± 0.12	21.0 ± 0.08
LESS 64	> 26.85	...	> 28.38	26.53 ± 0.25	25.52 ± 0.12	24.29 ± 0.08	24.17 ± 0.16	24.44 ± 0.28	> 23.64	24.28 ± 0.09	...	> 22.72	23.06 ± 0.04	22.51 ± 0.11	22.41 ± 0.12	22.27 ± 0.25	21.8 ± 0.12
LESS 66	21.03 ± 0.00	20.89 ± 0.01	...	21.18 ± 0.00	21.13 ± 0.00	20.79 ± 0.00	20.64 ± 0.01	20.23 ± 0.01	21.21 ± 0.04	...	20.33 ± 0.05	20.30 ± 0.04	...	19.61 ± 0.03	19.44 ± 0.03	19.36 ± 0.06	19.3 ± 0.03
LESS 67	26.14 ± 0.19	> 25.40	25.37 ± 0.10	24.85 ± 0.06	24.52 ± 0.05	24.42 ± 0.09	23.80 ± 0.11	23.74 ± 0.16	23.07 ± 0.20	22.79 ± 0.04	22.23 ± 0.16	21.16 ± 0.08	21.40 ± 0.02	20.63 ± 0.05	20.32 ± 0.05	20.20 ± 0.09	20.7 ± 0.06
LESS 70	25.19 ± 0.08	24.72 ± 0.19	24.56 ± 0.10	23.87 ± 0.02	23.78 ± 0.02	23.69 ± 0.05	23.61 ± 0.10	23.53 ± 0.13	22.56 ± 0.13	22.56 ± 0.04	22.51 ± 0.20	21.70 ± 0.13	21.60 ± 0.02	20.96 ± 0.06	20.78 ± 0.06	20.58 ± 0.11	20.8 ± 0.07
LESS 73	> 26.85	> 25.40	> 28.38	> 26.81	> 26.68	25.82 ± 0.31	24.38 ± 0.19	> 24.48	> 23.64	24.35 ± 0.09	> 23.02	> 22.72	23.53 ± 0.07	22.92 ± 0.13	22.79 ± 0.14	22.33 ± 0.25	21.9 ± 0.12
LESS 74a	> 26.85	...	> 28.38	> 26.81	> 26.68	> 25.79	> 24.94	24.72 ± 0.35	23.23 ± 0.22	23.48 ± 0.05	23.08 ± 0.33	22.41 ± 0.24	22.08 ± 0.03	21.45 ± 0.07	21.17 ± 0.07	21.15 ± 0.14	21.8 ± 0.12
LESS 74b	> 26.85	...	27.83 ± 0.15	> 26.81	> 26.68	> 25.79	25.04 ± 0.32	> 24.48	23.36 ± 0.25	23.60 ± 0.06	> 23.02	22.08 ± 0.18	22.47 ± 0.03	21.58 ± 0.07	21.18 ± 0.07	21.04 ± 0.14	21.5 ± 0.10
LESS 75	25.14 ± 0.08	24.80 ± 0.20	...	23.86 ± 0.02	23.60 ± 0.02	23.42 ± 0.04	23.38 ± 0.08	23.50 ± 0.13	22.81 ± 0.16	22.95 ± 0.04	...	22.10 ± 0.19	22.17 ± 0.03	21.07 ± 0.06	20.43 ± 0.05	19.79 ± 0.08	19.0 ± 0.03
LESS 79	26.37 ± 0.23	> 25.40	25.56 ± 0.11	25.16 ± 0.08	24.84 ± 0.06	24.54 ± 0.10	23.61 ± 0.10	23.74 ± 0.16	22.63 ± 0.13	22.41 ± 0.03	22.09 ± 0.14	21.24 ± 0.09	21.20 ± 0.02	20.32 ± 0.04	20.16 ± 0.04	20.32 ± 0.10	20.8 ± 0.07
LESS 81	25.94 ± 0.16	> 25.40	...	24.18 ± 0.03	23.73 ± 0.02	23.39 ± 0.04	22.79 ± 0.05	...	21.38 ± 0.04	22.45 ± 0.03	21.49 ± 0.08	20.90 ± 0.07	21.70 ± 0.02	20.18 ± 0.04	19.91 ± 0.04	20.11 ± 0.09	20.6 ± 0.07
LESS 84	26.42 ± 0.24	> 25.40	25.62 ± 0.11	25.10 ± 0.07	25.03 ± 0.08	24.89 ± 0.14	24.43 ± 0.20	> 24.48	> 23.64	23.36 ± 0.05	22.81 ± 0.26	21.71 ± 0.13	22.10 ± 0.03	21.43 ± 0.07	21.08 ± 0.06	20.92 ± 0.13	21.1 ± 0.08
LESS 87	...	...	25.52 ± 0.11	...	...	...	...	...	...	...	...	...	...	21.32 ± 0.06	21.07 ± 0.06	21.03 ± 0.14	20.9 ± 0.07
LESS 88	26.78 ± 0.32	> 25.40	25.98 ± 0.11	25.42 ± 0.10	25.10 ± 0.08	24.98 ± 0.15	24.27 ± 0.17	24.43 ± 0.28	23.25 ± 0.23	23.51 ± 0.06	23.05 ± 0.32	22.00 ± 0.17	22.05 ± 0.04	21.15 ± 0.06	20.85 ± 0.06	20.73 ± 0.12	21.0 ± 0.08
LESS 96	21.92 ± 0.00	21.73 ± 0.01	21.32 ± 0.10	20.82 ± 0.00	20.62 ± 0.00	20.40 ± 0.00	19.99 ± 0.00	19.72 ± 0.00	19.74 ± 0.01	19.50 ± 0.01	19.77 ± 0.04	19.76 ± 0.02	19.59 ± 0.01	19.63 ± 0.03	19.43 ± 0.03	19.07 ± 0.05	18.5 ± 0.02
LESS 98	> 26.85	...	...	> 26.81	> 26.68	> 25.79	24.61 ± 0.23	24.64 ± 0.33	23.41 ± 0.26	22.98 ± 0.04	...	21.49 ± 0.11	21.40 ± 0.02	20.22 ± 0.04	19.84 ± 0.04	19.99 ± 0.08	20.3 ± 0.05
LESS 101	> 26.85	> 25.40	27.28 ± 0.13	26.70 ± 0.29	26.20 ± 0.21	25.58 ± 0.25	> 24.94	> 24.48	> 23.64	24.33 ± 0.10	> 23.02	> 22.72	23.16 ± 0.05	22.44 ± 0.11	21.93 ± 0.10	21.62 ± 0.18	21.5 ± 0.10
LESS 102	> 26.85	> 25.40	...	26.93 ± 0.34	26.24 ± 0.22	25.98 ± 0.35	24.97 ± 0.31	24.49 ± 0.29	22.91 ± 0.17	...	...	21.29 ± 0.09	...	20.43 ± 0.04	20.13 ± 0.04	20.17 ± 0.09	20.3 ± 0.08
LESS 103	> 26.85	...	...	> 26.81	> 26.68	> 25.79	> 24.94	> 24.48	> 23.64	...	...	22.78 ± 0.33	...	21.51 ± 0.07	21.25 ± 0.07	21.12 ± 0.14	21.7 ± 0.12
LESS 106	> 26.85	> 25.40	...	> 26.81	> 26.68	> 25.79	24.51 ± 0.21	24.38 ± 0.27	23.07 ± 0.20	22.71 ± 0.04	21.76 ± 0.11	21.33 ± 0.10	21.22 ± 0.02	20.22 ± 0.04	19.83 ± 0.04	19.91 ± 0.08	20.0 ± 0.05
LESS 108	21.25 ± 0.00	21.00 ± 0.01	20.82 ± 0.10	19.64 ± 0.00	19.11 ± 0.00	18.60 ± 0.00	18.02 ± 0.00	17.94 ± 0.00	17.41 ± 0.00	17.35 ± 0.00	17.15 ± 0.04	17.00 ± 0.00	16.99 ± 0.00	...	17.79 ± 0.01	17.84 ± 0.03	
LESS 110	...	...	...	...	...	...	...	...	...	...	...	...	...	23.13 ± 0.16	22.44 ± 0.12	21.82 ± 0.20	21.7 ± 0.12
LESS 111	25.06 ± 0.07	25.03 ± 0.25	...	23.82 ± 0.02	23.31 ± 0.02	22.79 ± 0.02	22.38 ± 0.03	22.27 ± 0.04	22.75 ± 0.15	...	...	21.57 ± 0.12	...	21.04 ± 0.06	20.98 ± 0.06	20.81 ± 0.12	20.2 ± 0.05
LESS 112	...	...	26.98 ± 0.15	...	...	...	...	...	...	...	...	...	...	20.93 ± 0.05	20.59 ± 0.05	20.43 ± 0.10	21.0 ± 0.08
LESS 114	25.31 ± 0.09	25.24 ± 0.29	24.98 ± 0.10	24.52 ± 0.04	24.21 ± 0.04	23.87 ± 0.06	23.05 ± 0.06	22.91 ± 0.07	21.63 ± 0.06	21.62 ± 0.02	20.97 ± 0.05	20.68 ± 0.05	20.67 ± 0.01	19.93 ± 0.03	19.66 ± 0.03	19.86 ± 0.08	20.1 ± 0.05
LESS 117	26.42 ± 0.24	> 25.40	...	> 26.81	> 26.68	> 25.79	24.09 ± 0.15	...	22.58 ± 0.13	...	21.60 ± 0.09	21.47 ± 0.11	...	20.56 ± 0.05	20.31 ± 0.05	20.53 ± 0.11	20.9 ± 0.08
LESS 118	...	...	...	...	...	...	...	...	...	24.30 ± 0.08	...	...	23.98 ± 0.08	23.39 ± 0.17	23.81 ± 0.25	22.77 ± 0.34	> 23.50
LESS 120	> 26.85	> 25.40	...	26.77 ± 0.30	25.99 ± 0.18	> 25.79	24.60 ± 0.23	23.79 ± 0.16	23.34 ± 0.25	23.23 ± 0.05	22.79 ± 0.26	21.77 ± 0.14	21.87 ± 0.03	20.99 ± 0.05	20.70 ± 0.05	20.74 ± 0.12	21.33 ± 0.09
LESS 122	24.83 ± 0.06	24.70 ± 0.19	24.42 ± 0.10	23.77 ± 0.02	23.44 ± 0.02	23.28 ± 0.03	22.94 ± 0.05	22.86 ± 0.07	21.96 ± 0.07	21.96 ± 0.03	21.43 ± 0.08	21.20 ± 0.09	21.00 ± 0.02	20.24 ± 0.04	19.88 ± 0.04	19.59 ± 0.07	19.6 ± 0.04
LESS 126	> 26.85	> 25.40	26.87 ± 0.12	26.32 ± 0.21	26.61 ± 0.30	25.87 ± 0.32	> 24.94	...

REFERENCES

Alexander D. M., Bauer F. E., Chapman S. C., Smail I., Blain A. W., Brandt W. N., Ivison R. J., 2005, ApJ, 632, 736

Aretxaga I., Hughes D. H., Coppin K., Mortier A. M. J., Wagg J., Dunlop J. S., Chapin E. L., Eales et al., 2007, MNRAS, 379, 1571

Austermann J. E., Dunlop J. S., Perera T. A., Scott K. S., Wilson G. W., Aretxaga I., Hughes D. H., Almaini et al., 2010, MNRAS, 401, 160

Balestra I., Mainieri V., Popesso P., Dickinson M., Nonino M., Rosati P., Teimoorinia H., Vanzella et al., 2010, A&A, 512, A12+

Barger A. J., Cowie L. L., Sanders D. B., 1999, ApJ, 518, L5

Barger A. J., Cowie L. L., Sanders D. B., Fulton E., Taniguchi Y., Sato Y., Kawara K., Okuda H., 1998, Nature, 394, 248

Baugh C. M., Lacey C. G., Frenk C. S., Granato G. L., Silva L., Bressan A., Benson A. J., Cole S., 2005, MNRAS, 356, 1191

Bell E. F., 2003, ApJ, 586, 794

Bertin E., Arnouts S., 1996, A&AS, 117, 393

Bertoldi F., Carilli C., Aravena M., Schinnerer E., Voss H., Smolcic V., Jahnke K., Scoville et al., 2007, ApJS, 172, 132

Bertoldi F., Carilli C. L., Menten K. M., Owen F., Dey A., Gueth F., Graham J. R., Kreysa et al., 2000, A&A, 360, 92

Biggs A. D., Ivison R. J., Ibar E., Wardlow J. L., Dannerbauer H., Smail I., Walter F., Weiß et al., 2010, MNRAS, submitted

Blain A. W., Longair M. S., 1993, MNRAS, 264, 509

Blain A. W., Smail I., Ivison R. J., Kneib J., 1999, MNRAS, 302, 632

Blain A. W., Smail I., Ivison R. J., Kneib J., Frayer D. T., 2002, Phys. Rep., 369, 111

Bolzonella M., Miralles J.-M., Pelló R., 2000, A&A, 363, 476

Bruzual A. G., Charlot S., 1993, ApJ, 405, 538

Bruzual G., 2007, in Astronomical Society of the Pacific Conference Series, Vol. 374, From Stars to Galaxies: Building the Pieces to Build Up the Universe, A. Vallenari, R. Tantalo, L. Portinari, & A. Moretti, ed., pp. 303–+

Bunker A. J., Stanway E. R., Ellis R. S., McMahon R. G., McCarthy P. J., 2003, MNRAS, 342, L47

Calzetti D., Armus L., Bohlin R. C., Kinney A. L., Koornneef J., Storchi-Bergmann T., 2000, ApJ, 533, 682

Carilli C. L., Yun M. S., 1999, ApJ, 513, L13

—, 2000, ApJ, 530, 618

Casali M., Pirard J., Kissler-Patig M., Moorwood A., Bedin L., Biereichel P., Delabre B., Dorn et al., 2006, in Society of Photo-Optical Instrumentation Engineers (SPIE) Conference Series, Vol. 6269, Society of Photo-Optical Instrumentation Engineers (SPIE) Conference Series

Casey C. M., Chapman S. C., Beswick R. J., Biggs A. D., Blain A. W., Hainline L. J., Ivison R. J., Muxlow et al., 2009, MNRAS, 399, 121

Chabrier G., 2003, PASP, 115, 763

Chapin E. L., Pope A., Scott D., Aretxaga I., Austermann J. E., Chary R., Coppin K., Halpern et al., 2009, MNRAS, 398, 1793

Chapman S. C., Blain A. W., Ivison R. J., Smail I. R., 2003a, Nature, 422, 695

Chapman S. C., Blain A. W., Smail I., Ivison R. J., 2005, ApJ, 622, 772

Chapman S. C., Helou G., Lewis G. F., Dale D. A., 2003b, ApJ, 588, 186

Chapman S. C., Smail I., Blain A. W., Ivison R. J., 2004a, ApJ, 614, 671

Chapman S. C., Smail I., Windhorst R., Muxlow T., Ivison R. J., 2004b, ApJ, 611, 732

Clements D. L., Vaccari M., Babbedge T., Oliver S., Rowan-Robinson M., Davoodi P., Ivison R., Farrah et al., 2008, MNRAS, 387, 247

Condon J. J., 1992, ARA&A, 30, 575

Coppin K., Chapin E. L., Mortier A. M. J., Scott S. E., Borys C., Dunlop J. S., Halpern M., Hughes et al., 2006, MNRAS, 372, 1621

Coppin K., Chapman S., Smail I., Swinbank M., Walter F., Wardlow J., Weiss A., Alexander et al., 2010a, astro-ph/1004.4001

Coppin K., Pope A., Menéndez-Delmestre K., Alexander D. M., Dunlop J. S., Egami E., Gabor J., Ibar et al., 2010b, ApJ, 713, 503

Coppin K. E. K., Smail I., Alexander D. M., Weiss A., Walter F., Swinbank A. M., Greve T. R., Kovacs et al., 2009, MNRAS, 395, 1905

Cristiani S., Appenzeller I., Arnouts S., Nonino M., Aragón-Salamanca A., Benoist C., da Costa L., Dennefeld et al., 2000, A&A, 359, 489

Croom S. M., Warren S. J., Glazebrook K., 2001, MNRAS, 328, 150

Daddi E., Cimatti A., Renzini A., Fontana A., Mignoli M., Pozzetti L., Tozzi P., Zamorani G., 2004, ApJ, 617, 746

Daddi E., Renzini A., Pirzkal N., Cimatti A., Malhotra S., Stiavelli M., Xu C., Pasquali et al., 2005, ApJ, 626, 680

Damen M., Labbé I., Franx M., van Dokkum P. G., Taylor E. N., Gawiser E. J., 2009, ApJ, 690, 937

Damen M., Labbé I., van Dokkum P. G., Franx M., Taylor E. N., Brandt W. N., Dickinson M., Gawiser et al., 2010, ApJ, submitted

Dannerbauer H., Lehnert M. D., Lutz D., Tacconi L., Bertoldi F., Carilli C., Genzel R., Menten K., 2002, ApJ, 573, 473

Dannerbauer H., Walter F., Morrison G., 2008, ApJ, 673, L127

Devlin M. J., Ade P. A. R., Aretxaga I., Bock J. J., Chapin E. L., Griffin M., Gundersen J. O., Halpern et al., 2009, Nature, 458, 737

Dickinson M., Stern D., Giavalisco M., Ferguson H. C., Tsvetanov Z., Chornock R., Cristiani S., Dawson et al., 2004, ApJ, 600, L99

Doherty M., Bunker A. J., Ellis R. S., McCarthy P. J., 2005, MNRAS, 361, 525

Downes A. J. B., Peacock J. A., Savage A., Carrie D. R., 1986, MNRAS, 218, 31

Dunlop J. S., Ade P. A. R., Bock J. J., Chapin E. L., Cirasuolo M., Coppin K. E. K., Devlin M. J., et al G., 2009, astro-ph/0910.3642

Dye S., Eales S. A., Aretxaga I., Serjeant S., Dunlop J. S., Babbedge T. S. R., Chapman S. C., et al. C., 2008, MNRAS, 386, 1107

Eales S., Lilly S., Gear W., Dunne L., Bond J. R., Hammer F., Le Fèvre O., Crampton D., 1999, ApJ, 515, 518

Elbaz D., Cesarsky C. J., 2003, Science, 300, 270

Fazio G. G., Hora J. L., Allen L. E., Ashby M. L. N., Barmby P., Deutsch L. K., Huang J., et al. K., 2004, ApJS, 154, 10

Feldmann R., Carollo C. M., Porciani C., Lilly S. J., Capak P., Taniguchi Y., Le Fèvre O., Renzini et al., 2006, MNRAS, 372, 565

Gawiser E., van Dokkum P. G., Herrera D., Maza J., Castander F. J., Infante L., Lira P., Quadri et al., 2006, ApJS, 162, 1

Giacconi R., Zirm A., Wang J., Rosati P., Nonino M., Tozzi P., Gilli R., Mainieri et al., 2002, ApJS, 139, 369

Giavalisco M., Ferguson H. C., Koekemoer A. M., Dickinson M., Alexander D. M., Bauer F. E., Bergeron J., Biagetti et al., 2004,

ApJ, 600, L93
Grazian A., Fontana A., de Santis C., Nonino M., Salimbeni S., Giallongo E., Cristiani S., Gallozzi et al., 2006, A&A, 449, 951
Greve T. R., Bertoldi F., Smail I., Neri R., Chapman S. C., Blain A. W., Ivison R. J., Genzel et al., 2005, MNRAS, 359, 1165
Güsten R., Nyman L. Å., Schilke P., Menten K., Cesarsky C., Booth R., 2006, A&A, 454, L13
Hainline L. J., Blain A. W., Smail I., Alexander D. M., Armus L., Chapman S. C., Ivison R. J., 2010, astro-ph/1006.0238
Hainline L. J., Blain A. W., Smail I., Frayer D. T., Chapman S. C., Ivison R. J., Alexander D. M., 2009, ApJ, 699, 1610
Helou G., Soifer B. T., Rowan-Robinson M., 1985, ApJ, 298, L7
Hopkins A. M., Beacom J. F., 2006, ApJ, 651, 142
Hopkins P. F., Richards G. T., Hernquist L., 2007, ApJ, 654, 731
Hughes D. H., Serjeant S., Dunlop J., Rowan-Robinson M., Blain A., Mann R. G., Ivison R., Peacock et al., 1998, Nature, 394, 241
Ivison R. J., Greve T. R., Dunlop J. S., Peacock J. A., Egami E., Smail I., Ibar E., van Kampen et al., 2007, MNRAS, 380, 199
Ivison R. J., Greve T. R., Serjeant S., Bertoldi F., Egami E., Mortier A. M. J., Alonso-Herrero A., Barmby et al., 2004, ApJS, 154, 124
Ivison R. J., Greve T. R., Smail I., Dunlop J. S., Roche N. D., Scott S. E., Page M. J., Stevens et al., 2002, MNRAS, 337, 1
Ivison R. J., Magnelli B., Ibar E., Andreani P., Elbaz D., Altieri B., Amblard A., et al. A., 2010a, astro-ph/1005.1072
Ivison R. J., Smail I., Barger A. J., Kneib J., Blain A. W., Owen F. N., Kerr T. H., Cowie L. L., 2000, MNRAS, 315, 209
Ivison R. J., Smail I., Dunlop J. S., Greve T. R., Swinbank A. M., Stevens J. A., Mortier A. M. J., Serjeant et al., 2005, MNRAS, 364, 1025
Ivison R. J., Smail I., Le Borgne J., Blain A. W., Kneib J., Bezecourt J., Kerr T. H., Davies J. K., 1998, MNRAS, 298, 583
Ivison R. J., Smail I., Papadopoulos P. P., Wold I., Richard J., Swinbank A. M., Kneib J., Owen F. N., 2010b, MNRAS, 404, 198
Ivison R. J., Swinbank A. M., Swinyard B., Smail I., Pearson C. P., Rigopoulou D., Polehampton E., et al. B., 2010c, astro-ph/1005.1071
Kennicutt Jr. R. C., 1998, ARA&A, 36, 189
Kissler-Patig M., Pirard J., Casali M., Moorwood A., Ageorges N., Alves de Oliveira C., Baksai P., Bedin et al., 2008, A&A, 491, 941
Knudsen K. K., Kneib J., Richard J., Petitpas G., Egami E., 2010, ApJ, 709, 210
Knudsen K. K., van der Werf P. P., Kneib J., 2008, MNRAS, 384, 1611
Kriek M., van Dokkum P. G., Franx M., Illingworth G. D., Marchesini D., Quadri R., Rudnick G., Taylor et al., 2008, ApJ, 677, 219
Lacey C. G., Baugh C. M., Frenk C. S., Benson A. J., Orsi A., Silva L., Granato G. L., Bressan A., 2010, MNRAS, 405, 2
Lacey C. G., Baugh C. M., Frenk C. S., Silva L., Granato G. L., Bressan A., 2008, MNRAS, 385, 1155
Landsman W. B., 1993, in Astronomical Society of the Pacific Conference Series, Vol. 52, Astronomical Data Analysis Software and Systems II, R. J. Hanisch, R. J. V. Brissenden, & J. Barnes, ed., pp. 246–+
Le Fèvre O., Vettolani G., Paltani S., Tresse L., Zamorani G., Le Brun V., Moreau C., Bottini et al., 2004, A&A, 428, 1043
Lehmer B. D., Brandt W. N., Alexander D. M., Bauer F. E., Schneider D. P., Tozzi P., Bergeron J., Garmire et al., 2005, ApJS, 161, 21
Leitherer C., Schaerer D., Goldader J. D., González Delgado R. M., Robert C., Kune D. F., de Mello D. F., Devost et al., 1999, ApJS, 123, 3
Luo B., Bauer F. E., Brandt W. N., Alexander D. M., Lehmer B. D., Schneider D. P., Brusa M., Comastri et al., 2008, ApJS, 179, 19
Luo B., Brandt W. N., Xue Y. Q., Brusa M., Alexander D. M., Bauer F. E., Comastri A., Koekemoer et al., 2010, ApJS, 187, 560
Magnelli B., Lutz D., Berta S., Altieri B., Andreani P., Aussel H., Castaneda H., Cava et al., 2010, astro-ph/1005.1154
McCarthy P. J., Le Borgne D., Crampton D., Chen H., Abraham R. G., Glazebrook K., Savaglio S., et al. C., 2004, ApJ, 614, L9
Menéndez-Delmestre K., Blain A. W., Alexander D. M., Smail I., Armus L., Chapman S. C., Frayer et al., 2007, ApJ, 655, L65
Menéndez-Delmestre K., Blain A. W., Smail I., Alexander D. M., Chapman S. C., Armus L., Frayer D., Ivison et al., 2009, ApJ, 699, 667
Mignoli M., Cimatti A., Zamorani G., Pozzetti L., Daddi E., Renzini A., Broadhurst T., Cristiani et al., 2005, A&A, 437, 883
Morrissey P., Conrow T., Barlow T. A., Small T., Seibert M., Wyder T. K., Budavári T., Arnouts et al., 2007, ApJS, 173, 682
Nonino M., Dickinson M., Rosati P., Grazian A., Reddy N., Cristiani S., Giavalisco M., Kuntschner et al., 2009, ApJS, 183, 244
Pirard J., Kissler-Patig M., Moorwood A., Biereichel P., Delabre B., Dorn R., Finger G., Gojak et al., 2004, in Society of Photo-Optical Instrumentation Engineers (SPIE) Conference Series, Vol. 5492, Society of Photo-Optical Instrumentation Engineers (SPIE) Conference Series, A. F. M. Moorwood & M. Iye, ed., pp. 1763–1772
Pope A., Borys C., Scott D., Conselice C., Dickinson M., Mobasher B., 2005, MNRAS, 358, 149
Pope A., Chary R., Alexander D. M., Armus L., Dickinson M., Elbaz D., Frayer D., Scott et al., 2008, ApJ, 675, 1171
Pope A., Scott D., Dickinson M., Chary R., Morrison G., Borys C., Sajina A., Alexander et al., 2006, MNRAS, 370, 1185
Popesso P., Dickinson M., Nonino M., Vanzella E., Daddi E., Fosbury R. A. E., Kuntschner H., Mainieri et al., 2009, A&A, 494, 443
Ravikumar C. D., Puech M., Flores H., Proust D., Hammer F., Lehnert M., Rawat A., Amram et al., 2007, A&A, 465, 1099
Rieke G. H., Young E. T., Engelbracht C. W., Kelly D. M., Low F. J., Haller E. E., Beeman J. W., et al. G., 2004, ApJS, 154, 25
Rodighiero G., Vaccari M., Franceschini A., Tresse L., Le Fevre O., Le Brun V., Mancini C., Matute et al., 2010, A&A, 515, A8+
Sanders D. B., Mirabel I. F., 1996, ARA&A, 34, 749
Silva L., Granato G. L., Bressan A., Danese L., 1998, ApJ, 509, 103
Siringo G., Kreysa E., Kovács A., Schuller F., Weiß A., Esch W., Gemünd H., Jethava et al., 2009, A&A, 497, 945
Smail I., Ivison R. J., Blain A. W., 1997, ApJ, 490, L5+
Smail I., Ivison R. J., Kneib J., Cowie L. L., Blain A. W., Barger A. J., Owen F. N., Morrison G., 1999, MNRAS, 308, 1061
Smail I., Ivison R. J., Owen F. N., Blain A. W., Kneib J.-P., 2000, ApJ, 528, 612
Stanway E. R., Bunker A. J., McMahon R. G., Ellis R. S., Treu T., McCarthy P. J., 2004, ApJ, 607, 704
Steidel C. C., Shapley A. E., Pettini M., Adelberger K. L., Erb D. K., Reddy N. A., Hunt M. P., 2004, ApJ, 604, 534
Strolger L., Riess A. G., Dahlen T., Livio M., Panagia N., Challis P., Tonry J. L., Filippenko et al., 2004, ApJ, 613, 200
Surace J. A., Shupe D. L., Fang F., Lons-

dale C. J., Gonzalez-Solares et al., 2005, http://swire.ipac.caltech.edu/swire/astronomers/publications
Swinbank A. M., Chapman S. C., Smail I., Lindner C., Borys C., Blain A. W., Ivison R. J., Lewis G. F., 2006, MNRAS, 371, 465
Swinbank A. M., Lacey C. G., Smail I., Baugh C. M., Frenk C. S., Blain A. W., Chapman S. C., Coppin et al., 2008, MNRAS, 391, 420
Szokoly G. P., Bergeron J., Hasinger G., Lehmann I., Kewley L., Mainieri V., Nonino M., Rosati et al., 2004, ApJS, 155, 271
Takata T., Sekiguchi K., Smail I., Chapman S. C., Geach J. E., Swinbank A. M., Blain A., Ivison R. J., 2006, ApJ, 651, 713
Taylor E. N., Franx M., van Dokkum P. G., Bell E. F., Brammer G. B., Rudnick G., Wuyts S., et al. G., 2009a, ApJ, 694, 1171
Taylor E. N., Franx M., van Dokkum P. G., Quadri R. F., Gawiser E., Bell E. F., Barrientos L. F., Blanc et al., 2009b, ApJS, 183, 295
Treister E., Virani S., Gawiser E., Urry C. M., Lira P., Francke H., Blanc G. A., Cardamone et al., 2009, ApJ, 693, 1713
Vaccari M., Marchetti L., Franceschini A., Altieri B., Amblard A., Arumugam V., Auld R., Aussel e. a., 2010, astro-ph/1005.2187
van der Wel A., Franx M., van Dokkum P. G., Rix H., 2004, ApJ, 601, L5
Vanzella E., Cristiani S., Dickinson M., Giavalisco M., Kuntschner H., Haase J., Nonino M., Rosati et al., 2008, A&A, 478, 83
Wang W., Cowie L. L., van Saders J., Barger A. J., Williams J. P., 2007, ApJ, 670, L89
Wardlow J. L., Smail I., Wilson G. W., Yun M. S., Coppin K. E. K., Cybulski R., Geach J. E., Ivison et al., 2010, MNRAS, 401, 2299
Weiß A., Kovács A., Coppin K., Greve T. R., Walter F., Smail I., Dunlop J. S., Knudsen et al., 2009, ApJ, 707, 1201
Younger J. D., Fazio G. G., Huang J., Yun M. S., Wilson G. W., Ashby M. L. N., Gurwell M. A., Lai et al., 2007, ApJ, 671, 1531
Younger J. D., Fazio G. G., Huang J., Yun M. S., Wilson G. W., Ashby M. L. N., Gurwell M. A., Peck et al., 2009, ApJ, 704, 803
Yun M. S., Aretxaga I., Ashby M. L. N., Austermann J., Fazio G. G., Giavalisco M., Huang J.-S., et al. H., 2008, MNRAS, 389, 333
Zheng W., Mikles V. J., Mainieri V., Hasinger G., Rosati P., Wolf C., Norman C., Szokoly et al., 2004, ApJS, 155, 73

APPENDIX A: DISCUSSION OF UNUSUAL SOURCES

Most LESS SMGs have properties similar to previous SMG populations. However, several robust counterparts have unusual properties, X-ray emission, or $8\,\mu$m excesses indicative of the presence of an AGN. We discuss these galaxies on a case-by-case basis below.

LESS 2a & 2b: LESS 2 has both a robust $24\,\mu$m (LESS 2a) and a robust radio counterpart (LESS 2b), separated by $2.7''$, with $z = 1.80^{+0.35}_{-0.14}$ and $2.27^{+0.16}_{-0.55}$ respectively. It is possible that the two counterparts are at the same redshift ($z \sim 2$), separated by ~ 20 kpc and may in the process of merging.

LESS 6: LESS 6 is $\sim 1''$ from the robust 24μm counterpart and $\sim 2.5''$ from the robust radio counterpart and has a photometric redshift of $z = 0.40^{+0.09}_{-0.03}$, therefore it is possible that the submillimetre source is a background galaxy which is being gravitationally lensed by LESS 6.

LESS 9: This SMG is X-ray luminous and has $z_{phot} = 4.63^{+0.10}_{-1.10}$ making it the highest redshift X-ray source in our sample. Our best-fitting SED shows no $8\,\mu$m excess and thus no suggestion of an AGN from the near-infrared and optical photometry.

LESS 10a: LESS 10a is one of two counterparts to LESS 10 identified from extended or blended radio emission. It has some $8\,\mu$m excess over the best-fit SED, suggesting the presence of an AGN, but no detectable X-ray emission.

LESS 11: Similarly to LESS 9 this galaxy shows no $8\,\mu$m excess but is X-ray bright.

LESS 19: Based upon the SED fitting LESS 19 has excess 5.8 and $8\,\mu$m emission. However, the source is faint and the fit has $\chi^2 = 10.0$ so it is unclear whether the apparent excess is due to errors in the fitting or the presence of an AGN.

LESS 20: This SMG is unusually radio bright with $S_{1.4\mathrm{GHz}} = 4.25$ mJy. There is no evidence of X-ray emission or an $8\,\mu$m excess, suggesting that LESS 20 is a radio-bright AGN. If this is the case then the AGN contribution to the radio flux means that T_D and L_{FIR} are likely to be significantly over-estimated. Therefore, we exclude LESS 20 from our analyses of the SFRs and luminosity function of SMGs.

LESS 40: LESS 40 has X-ray emission and an $8\,\mu$m excess and is highly likely to contain an AGN.

LESS 50b: This galaxy is X-ray luminous but does not exhibit a compelling $8\,\mu$m excess.

LESS 57: LESS 57 has a strong $8\,\mu$m excess and is X-ray bright, compelling evidence for the presence of an AGN in this SMG.

LESS 66: LESS 66 lies near the diffraction spike of a bright star, so some of the photometry may be unreliable. However, it is an optically bright point source with an $8\,\mu$m excess and X-ray emission. There are broad emission lines in the spectra suggesting that LESS 66 is a submillimetre-bright quasar.

LESS 67: This galaxy has coincident X-ray emission and may contain an AGN.

LESS 74a & b: The two counterparts to LESS 74 have $z = 1.84^{+0.32}_{-0.49}$ and $1.71^{+0.20}_{-0.17}$, are separated by $2.7''$ (~ 20 kpc), and have some faint extended emission between them in the optical images. Therefore, it is likely that LESS 74a and LESS 74b are undergoing an interaction at $z \sim 1.8$ which triggered the submillimetre emission.

LESS 75: Although LESS 75 is not X-ray detected there is strong 8 and $5.8\,\mu$m excess above the best-fit SED, indicative of a highly obscured AGN.

LESS 84: LESS 84 is X-ray detected, and has a small $8\,\mu$m excess suggesting it may contain an AGN.

LESS 96: LESS 96 is similar to LESS 66 – it is X-ray luminous and has a strong 8 μm excess above the best-fit SED, and it is an bright optical point source. We interpret this as evidence that LESS 96 is a submillimetre-bright quasar.

LESS 106: This SMG is X-ray detected but no $8\,\mu$m excess is observed.

LESS 108: LESS 108 is identified as a bright local ($z = 0.086$) late-type spiral galaxy from its strong radio and $24\,\mu$m emission. The similarity of the radio, mid- and near-infrared, and optical morphologies suggests that this is not a case of gravitational lensing.

LESS 111: LESS 111 is X-ray detected and has a $8\,\mu$m excess, indicating it may contain an AGN. It lies $\lesssim 3''$ from an extended foreground galaxy and is likely to be gravitationally lensed.

LESS 114: This SMG is coincident with an X-ray source, but shows no evidence of an $8\,\mu$m excess above the best-fit SED.

LESS 122: LESS 122 has excess flux at $8\,\mu$m compared to the best-fit SED but is not X-ray detected.

APPENDIX B: SED FITS

In Fig. B1 we show the measured photometry and best-fit SED for each SMG counterpart. The calculated photometric redshifts and errors are shown, and the probability distribution functions presented for each galaxy. Most SMGs are well-fit by out template SEDs, although nine (12%) have excess 8 μm flux above the best-fit SED.

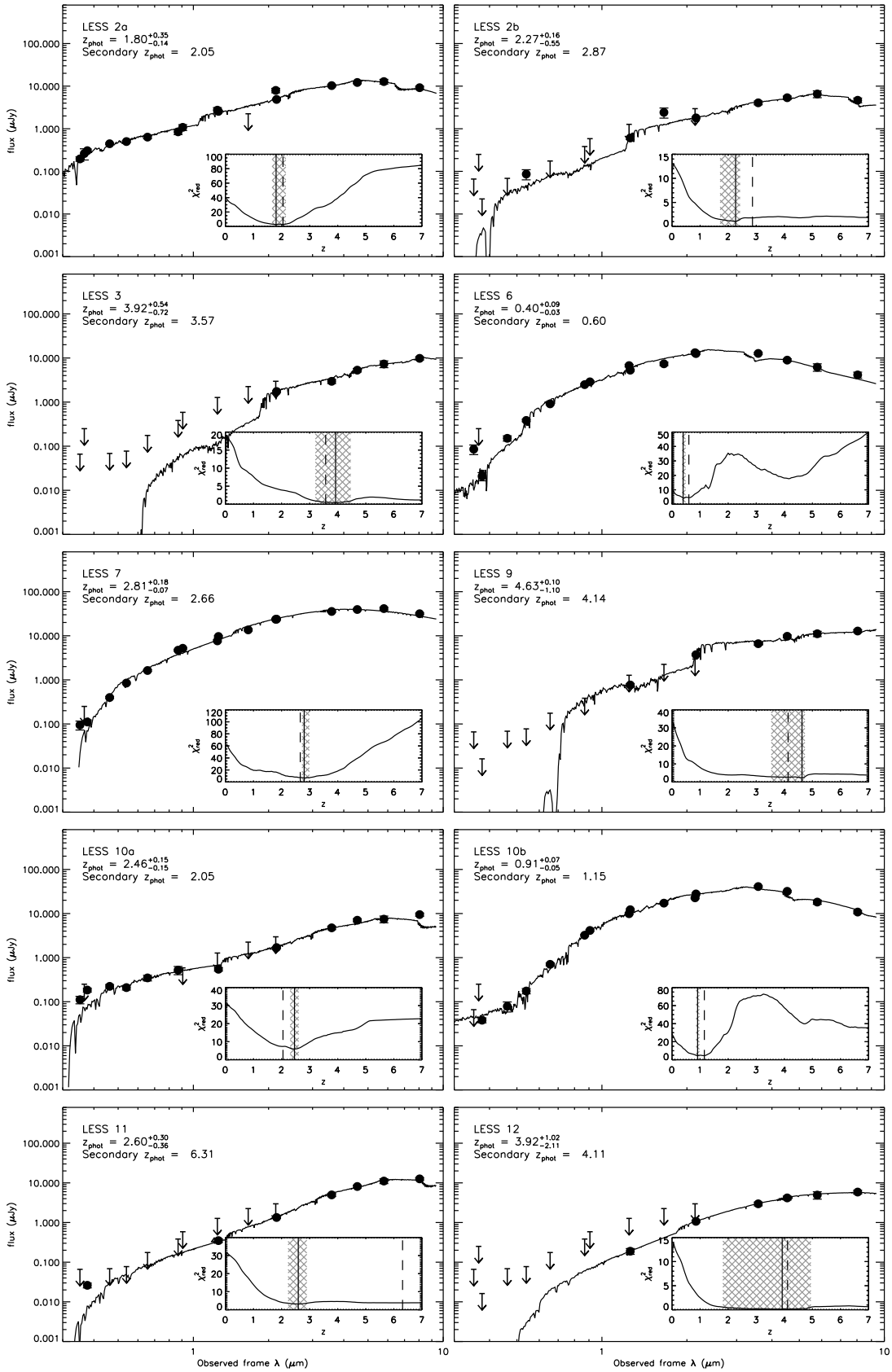

Figure B1. Photometry and best-fit SEDs for robust SMG counterparts; points and error-bars show measured photometry and arrows represent 3σ detection limits. Error bars on the primary photometric redshift are 99% confidence limits. Inset panels show the minimum reduced χ^2 at each redshift step with the photometric redshift primary and secondary solutions (where they exist) marked by solid and dashed lines respectively; the photometric redshift error is represented by the shaded region.

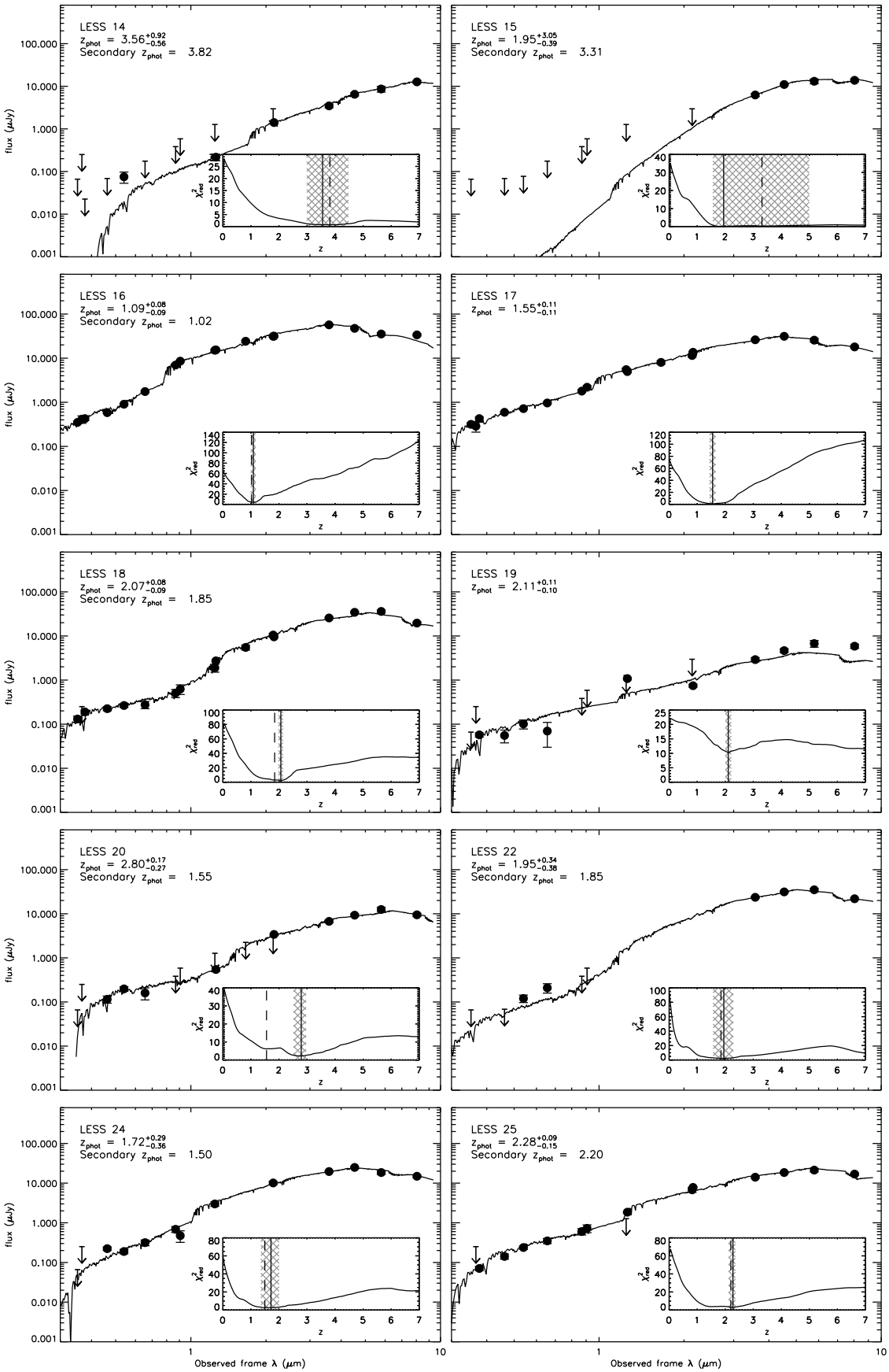

Figure B1 – *continued*

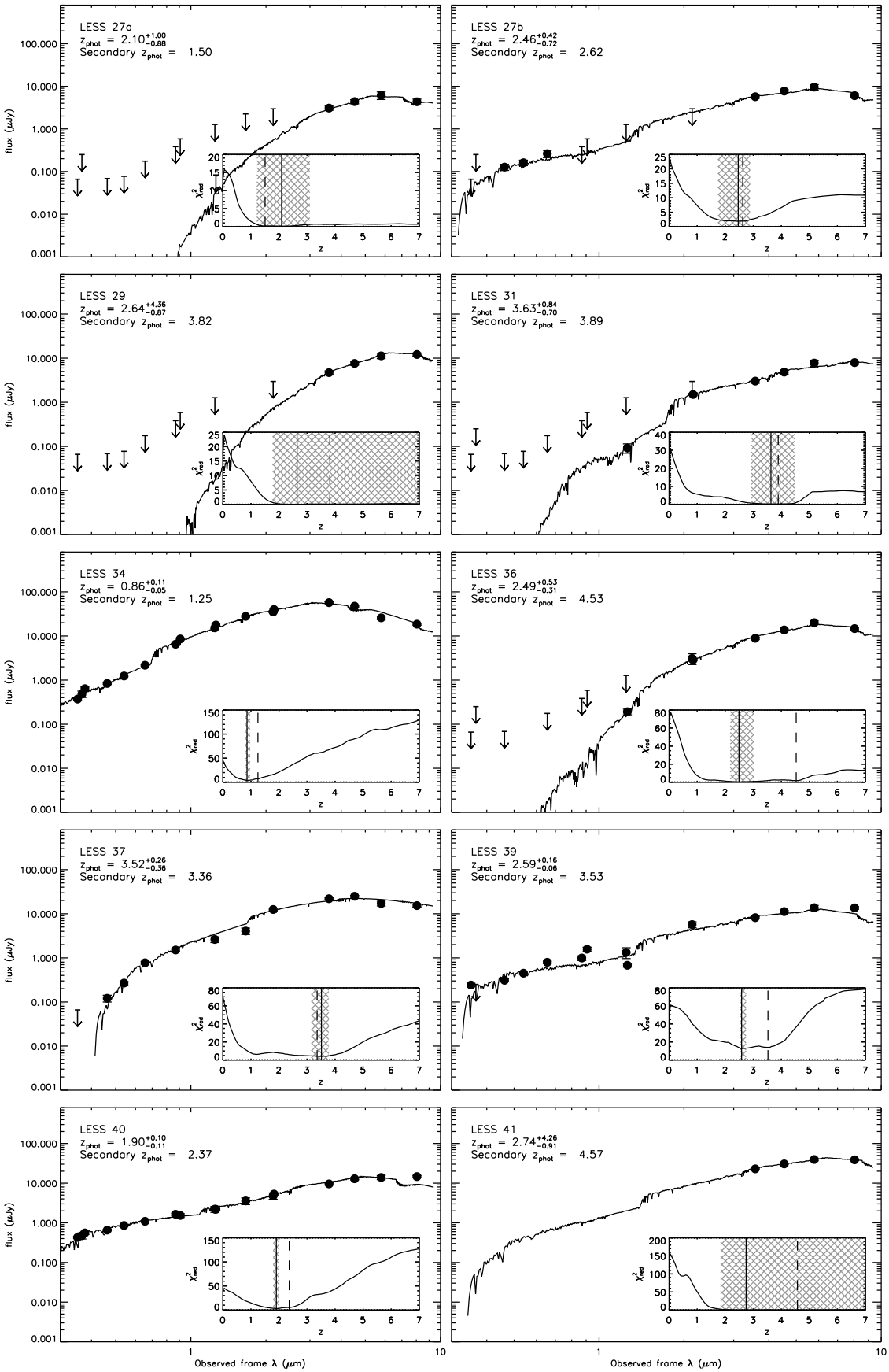

Figure B1 – *continued*

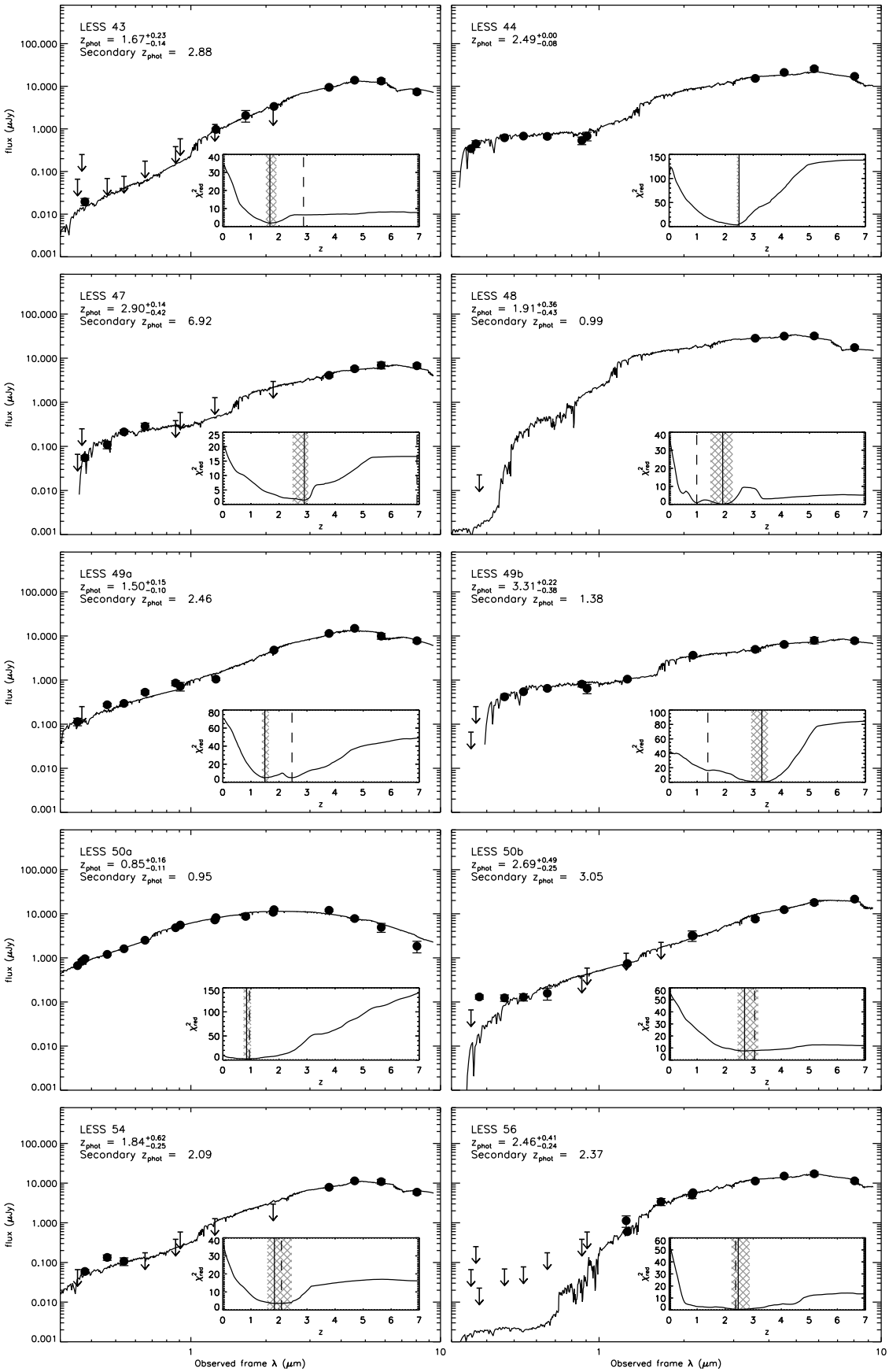

Figure B1 – *continued*

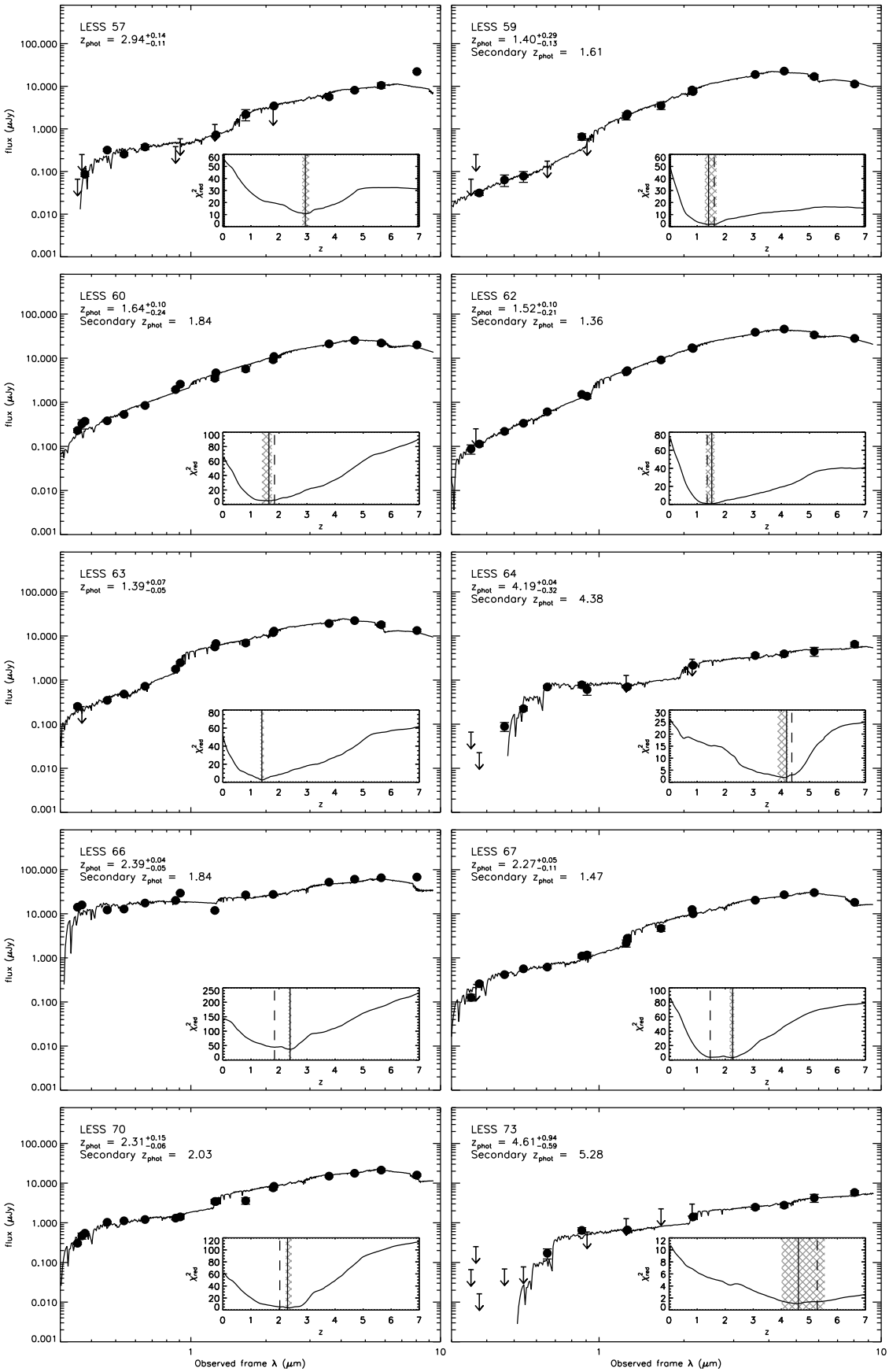

Figure B1 – *continued*

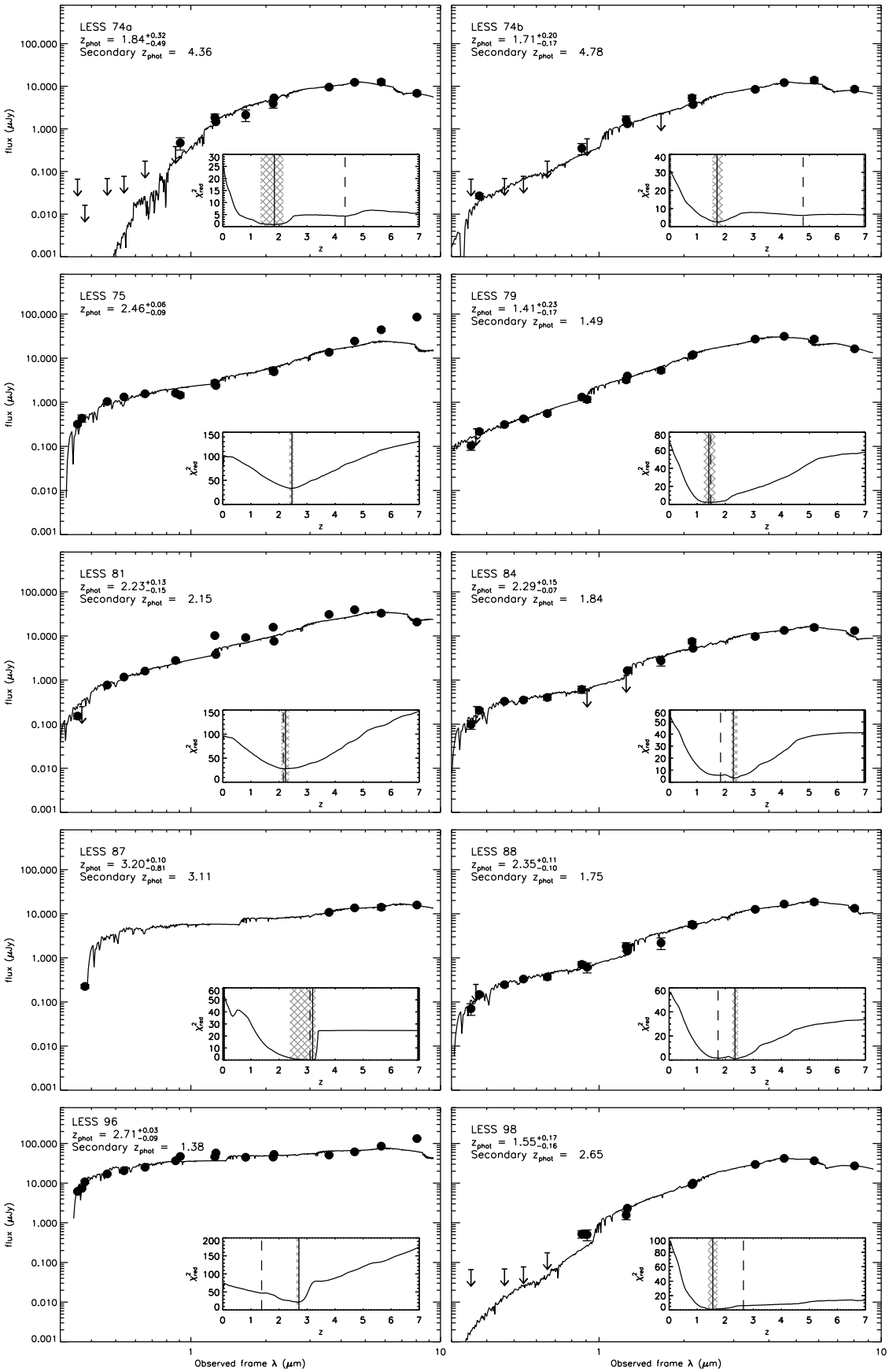

Figure B1 – *continued*

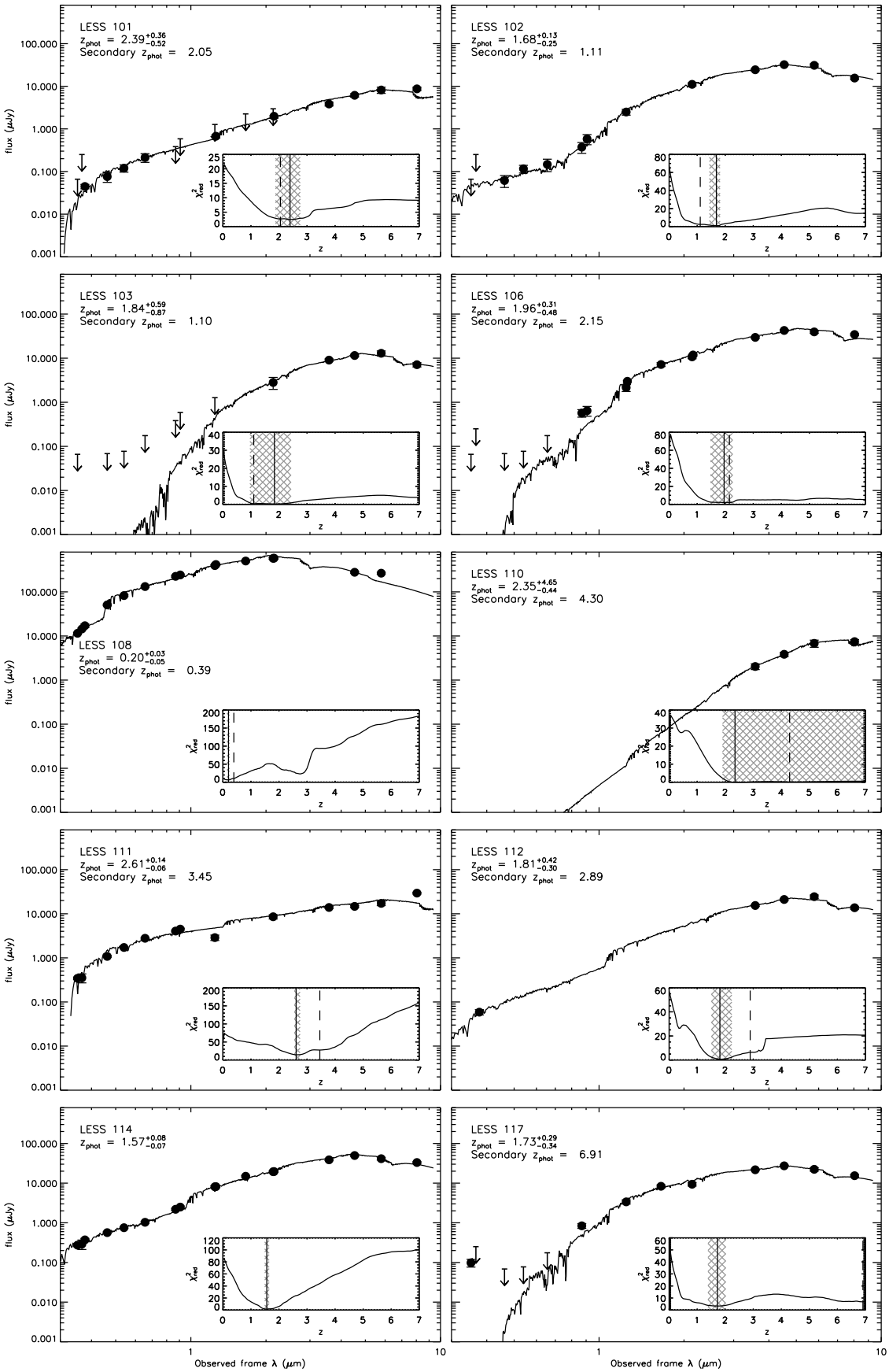

Figure B1 – *continued*

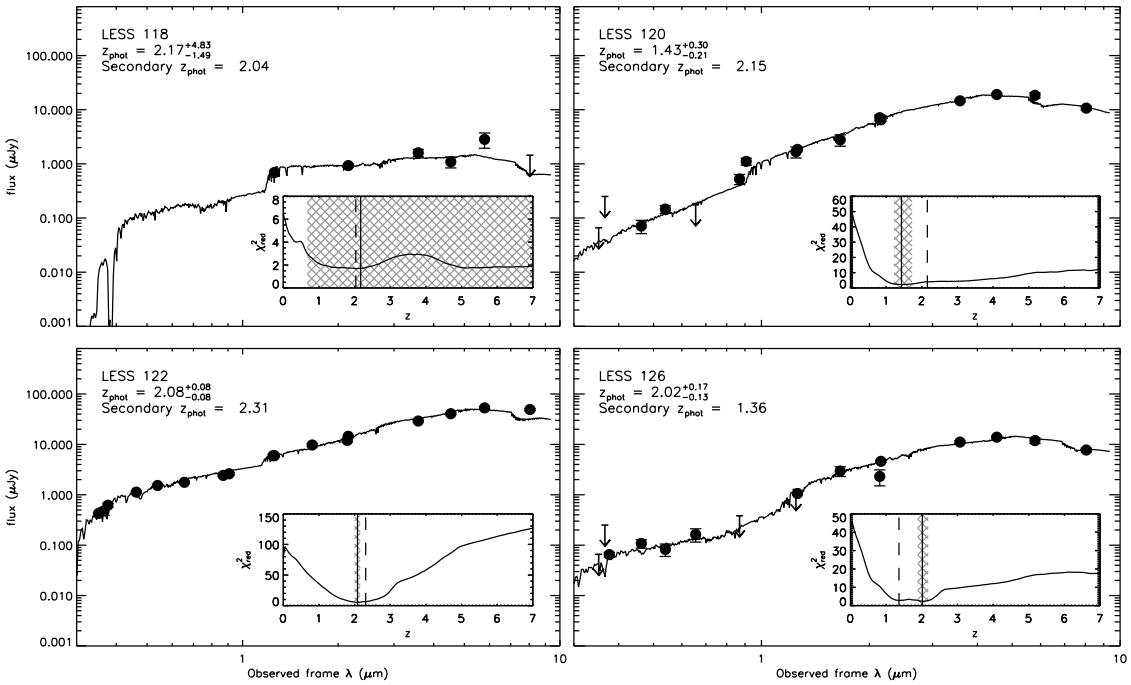

Figure B1 – *continued*